Max-Planck-Institut
für Kolloid- und Grenzflächenforschung

Universität Potsdam

Nanoparticles at Solid Interfaces

Dissertation

zur Erlangung des akademischen Grades
Doktor der Naturwissenschaften
”doctor rerum naturalium”
(Dr. rer. nat.)
in der Wissenschaftsdisziplin „Physikalische Chemie“

eingereicht an der
Mathematisch-Naturwissenschaftlichen Fakultät
der Universität Potsdam
&
Max-Planck-Institut für Kolloid- und Grenzflächenforschung
Abteilung Theorie & Bio-System

von
Guoxiang Chen

Erst Betreuer:
Prof. Dr. Gerald Brezesinski
Zweit Betreuer:
PD Dr. Hans Riegler

Potsdam, März 2018

To my parents

Abstract

Nanoparticles (NPs) are particles between 1 and 100 nanometers in size. They have attracted enormous research interests owing to their remarkable physicochemical properties and potential applications in the optics, catalysis, sensing, electronics, or optical devices. The thesis investigates systems of NPs attached to planar substrates.

In the first part of the results section of the thesis a new method is presented to immobilize NPs. In many NP applications a strong, persistent adhesion to substrates is a key requirement. Up to now this has been achieved with various methods, which are not always the optimum regarding adhesion strength or applicability. We propose a new method which uses capillarity to enhance the binding agents in the contact area between NP and substrate. The adhesion strength resulting from the new approach is investigated in detail and it is shown that the new approach is superior to older methods in several ways.

The following section presents the optical visualization of nano-sized objects through a combination of thin film surface distortion and interference enhanced optical reflection microscopy. It is a new, fast and non-destructive technique. It not only reveals the location of NPs as small as 20nm attached to planar surfaces and embedded in a molecularly thin liquid film. It also allows the measurement of the geometry of the surface distortion of the liquid film. Even for small NPs the meniscus reaches out for micrometers, which is the reason why the NPs produce such a pronounced optical footprint.

The nucleation and growth of individual bubbles is presented in chapter 5. Nucleation is a ubiquitous natural phenomenon and of great importance in numerous industrial processes. Typically it occurs on very small scales (nanometers) and it is of a random nature (thermodynamics of small systems). Up to now most experimental nucleation studies deal with a large number of individual nucleation processes to cope with its inherently statistical, spatio-temporal character. In contrast, in this thesis the individual O_2-bubble formation from single localized platinum NP active site is studied experimentally. The bubble formation is initiated by the catalytic reaction of H_2O_2 on the Pt surface. It is studied how the bubble nucleation and growth depends on the NP size, the H_2O_2 concentration and the substrate surface properties. It is observed that in some cases the bubbles move laterally over the substrate surface, driven by the O_2-production and the film ablation.

Zusammenfassung

Nanopartikel (NP) sind Partikel in der Größe zwischen 1 bis 100 nm Größe. Sie sind von enormem Interesse für die Forschung aufgrund ihrer physiko-chemischen Eigenschaften und möglicher Anwendungen in Optik, Katalyse, Sensorik oder Elektronik. In der Arbeit werden Systeme von NPs auf planaren Substraten untersucht.

Im ersten Resultate-Abschnitt der Arbeit wird eine neue Methode zur Immobilisierung von NPs vorgestellt. Für viele NP-Anwendungen ist eine starke, andauernde Haftung an die Substrate eine wesentliche Voraussetzung. Bislang wurde dies mit verschiedenen Methoden erreicht, die aber nicht immer ideal bezüglich der Adhäsion oder der Anwendbarkeit sind. Die neue Methode benutzt Kapillarität um den Adhäsionsvermittler im Kontaktbereich zwischen NP und Substrat anzureichern. Die Stärke der Adhäsion infolge der neuen Methode wird im Detail untersucht und es wird gezeigt, dass die neue Methode älteren Verfahren gegenüber in mehreren Aspekten überlegen ist.

Der folgende Abschnitt präsentiert die optische Visualisierung von nano-dimensionalen Objekten durch eine Kombination der Deformation der Oberfläche eines dünnen Films und interferenz-verstärkter optischer Reflexions-Mikroskopie. Es ist eine neue, schnelle und zerstörungsfreie Technik. Sie zeigt nicht nur die Position von NP herunter bis zu 20nm Größe auf ebenen Substrate auf, wenn sie in molekular dünnen Filmen eingebettet sind. Damit kann auch die genaue Geometrie des Meniskus der Oberflächendeformierung gemessen werden. Selbst bei kleinen NPs reicht der Meniskus Mikrometer weit. Dies ist der Grund dafür, dass die NP solch ein ausgeprägtes optische Signal produzieren.

Kapitel 5 befasst sich mit der Keimbildung und dem Wachstum von individuellen Gasblasen. Keimbildung ist ein weitverbreitetes Naturphänomen und sehr wichtig in zahlreichen industriellen Prozessen. Es findet typischerweise auf sehr kleiner Skala (Nanometer) statt und ist ein statistisches Ereignis (Thermodynamik kleiner Systeme). Bislang beschäftigen sich die meisten Keimbildungsstudien mit einer großen Zahl von individuellen Keimbildungsprozessen wegen des inhärent statistisch-raumzeitlichen Charakters. Im Kontrast dazu wird in der Arbeit die individuelle Sauerstoff-Blasen-Bildung an einer "aktiven Stelle", einem einzigen, lokalisierten Platin-NP experimentell untersucht. Die Blasenbildung resultiert aus der katalytischen Reaktion mit H_2O_2. Es wird untersucht wie die Blasenbildung von der Größe der NP, der H_2O_2-Konzentration und den Oberflächeneigenschaften des Substrates, wie beispielsweise Beschichtungen abhängt. Man beobachtet, dass sich die Blasen in manchen Fällen infolge der O_2-Produktion und der Ablösung der Beschichtung lateral bewegen.

Contents

Introduction

The study of nanoparticles (NPs) at solid interface is of great interest due to their applications in catalysis, optical devices, or sensors [1-4]. The goals of this thesis are to understand the behaviors of the NPs at a solid interface, especially the solid/liquid interface.

Chapter 1 of the thesis presents some basic concepts of interfacial thermodynamics, optical physics, and nucleation theory. Chapter 2 describes the material, sample preparations, and experimental methods.

Chapter 3 describes how to immobilize the NPs by nanoscale capillarity. The normal route for NP immobilization is realized by a cross linking agent with the sequence of functionalizing the substrate with the agent and then adsorbing the NPs [5-7]. We demonstrate a new strategy to realize the rapid and large-area fabrication of a stable attachment of metal NPs on a silicon substrate via simply changing the adding sequence of the coupling agent (APTES). Unlike in the traditional approach where the coupling agent is introduced in the beginning, our approach introduces a new sequence to attach the between NP and substrate by capillary condensation. We use ultrasonication to check the mechanical stability of immobilized NPs. AFM is applied to precisely check the NP coverage before and after such tests at the same region. We prove that this new proposal has more mechanical stability than the conventional approach. In addition, it is demonstrated that with this approach even weakly interacting monomers such as fullerenes (C_{60}) or polymers can be used to immobilize NPs on planar surfaces.

Chapter 4 presents a method to visualize the location of individual nano-sized objects (e.g., NPs) immersed in thin films by conventional optical reflection microscopy. Although the immersed objects are much smaller than the optical resolution limit, their position can be visualized optically through their distortion of the film/air interface. We use silica coated wafers to image the NPs through the optical interference-enhanced reflection microscopy technique [8-9]. The reflectivity contrast can be greatly enhanced by this auxiliary layer intercalated between the nano-sized objects and the reflecting substrate.

In Chapter 5, a single Pt NP immobilized on a silicon wafer surface acts as localized active nucleation site. Pt NPs catalyze the decomposition of hydrogen peroxide (H_2O_2) and induce the formation of oxygen[10]. Here we localize the Pt NP with optical microscopy and AFM. Then real-time measurements of individual bubble formation are possible.

Chapter 6 investigates the behavior of bubbles moving at silica surfaces coated with a nanometer thick hydrophobic polymer layer. Bubble formation is started from Pt NP active sites by decomposition of H_2O_2. After the bubble production is big enough, it will break the thin polymer film and then move sideways. We try different kinds of polymers and show that it works with hydrophobic polymers such as polystyrene (PS) and polyvinyl chloride (PVC). For poly (methyl methacrylate) (PMMA), the bubbles just grow but do not move.

1. Scientific background

1.1 Interfacial thermodynamics

1.1.1 Surface tension

The interface is the boundary between two spatial regions occupied by two immiscible phases. The interface between a condensed phase (liquid or solid) and air is named as surface. The interface or surface region has a finite thickness (e.g. 1-2 nm for water) where the composition and energy varies continuously from one phase to the other [11-12].

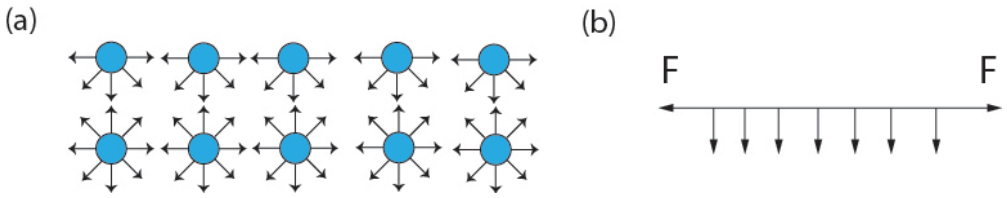

Figure 1.1: The schematic of the force analysis for the molecules in the bulk and at the interface. (a) the molecules in the bulk have neighbor molecules in all directions by other molecules for which they have an equal attraction; the molecules at the interface have neighbor molecules only by sides and downward molecules for which they have an unequal attraction. (b) the surface tension forces acting on molecules at the interface.

As shown in Figure 1.1, the molecules in the bulk liquid attract each other by different directions. However, the molecules at the interface are partially surrounded by the neighbor molecules [11]. Unlike the molecules in the bulk, surface molecules experience attraction mainly from either sides and downward, as shown in Figure 1.1(b). As a result, the energy of molecules at surfaces is higher than that in the bulk. Due to this difference, energy would be required to bring the molecules from the bulk to the interface to create a new interfacial region. This work required to form such a unit interface area is named as the interfacial tension, γ [12].

From fundamental thermodynamic relations, we get that a microscopic change in internal energy (U) can be expressed in terms of corresponding microscopic changes in entropy and volume for a closed system in thermal equilibrium [13]:

$$dU = TdS - pdV \tag{1.1}$$

Here, T is absolute temperature, S is entropy, p is pressure, and V is volume.

It is not considering the interface, only the bulk system. Actually even it is the pure liquid coexisting with its vapor; it must have an interfacial area (A). If considering the system with interface, it must pay surface work (γdA) on the system. The fundamental relation is expressed in terms of internal energy as:

$$dU = TdS - pdV + \gamma dA \tag{1.2}$$

in terms of enthalpy (*H*) as:

$$dH = TdS + Vdp + \gamma dA \tag{1.3}$$

in terms of Helmholtz free energy (*F*) as:

$$dF = -SdT - pdV + \gamma dA \tag{1.4}$$

in terms of Gibbs free energy (*G*) as:

$$dG = -SdT + Vdp + \gamma dA \tag{1.5}$$

According to the above relations, the interfacial tension γ follows

$$\gamma = (\frac{\partial U}{\partial A})_{S,V,n} = (\frac{\partial H}{\partial A})_{S,p,n} = (\frac{\partial F}{\partial A})_{T,V,n} = (\frac{\partial G}{\partial A})_{T,p,n} \tag{1.6}$$

1.1.2 Young-Laplace equation

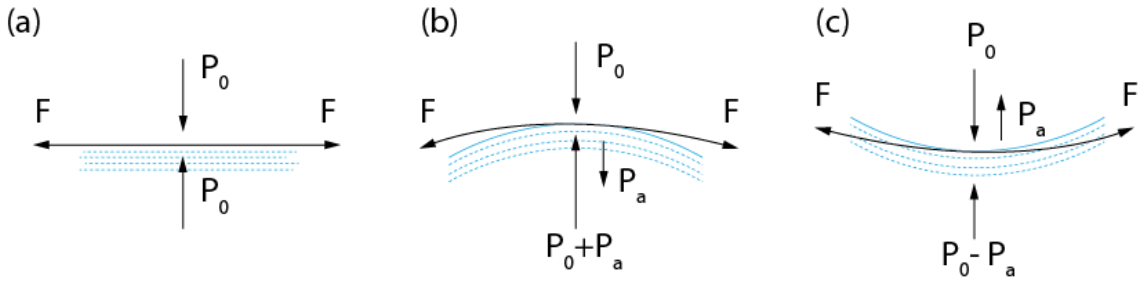

Figure 1.2: Schematic of an additional pressure on a curved surface.

If a liquid surface is curved in equilibrium, there will be a pressure difference across it, which results from the surface tension [11]. As shown in Figure 1.2 (a), if the liquid surface is planar, when we focus on a small patch of the surface, the force resulting from surface tension is balanced with neighbor molecules. The pressure difference between inside and outside is zero. If the surface is curved, the force is not planar and its direction is like in

Figure 1.2 (b) or (c). In equilibrium, the resultant force will point to inside or outside of the liquid. Therefore, comparing with planar liquid surface, the curved surface has an additional pressure (p_a), which is the result of mechanical equilibrium under the effect of interfacial tension.

The Young-Laplace equation relates such additional pressure between two static fluid phases, and the curvature of the surface [11].

$$\Delta p = p_a = \gamma \left(\frac{1}{R_1} + \frac{1}{R_2}\right) \tag{1.7}$$

where R_1 and R_2 are the two principal radii of curvature, Δp is called Laplace pressure. When the shape of the interface is a sphere, the two principle radii of curvature equal the radius of the sphere (R), then the Laplace pressure is changing to

$$\Delta p = \frac{2\gamma}{R} \tag{1.8}$$

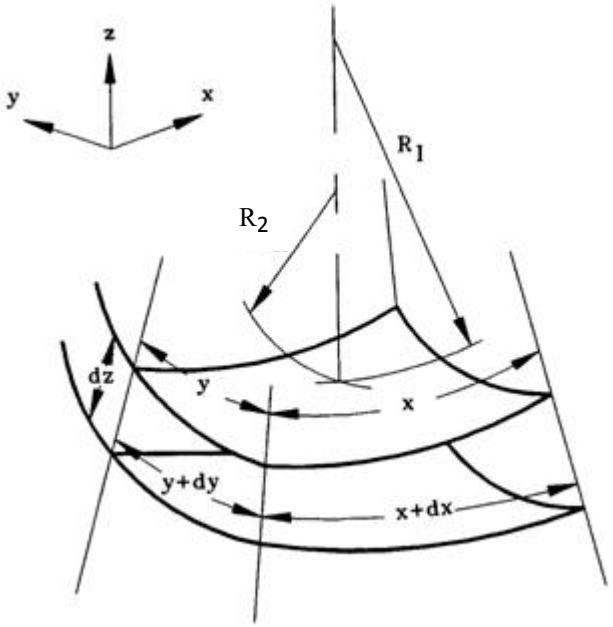

Figure 1.3: Diagram used for deriving the Young-Laplace equation.

To derive the equation of Young-Laplace we need to look at a small patch on the interface with area $\delta A\ (xy)$. Here we make a small displacement of the interface as shown in Figure

1.3, denoted as *dz*, it will induce a small change of the area of the interface patch $d\delta A$, and change of the volume of the small body $dV = \delta A dz$. The volume work done to form this additional amount of surface by the environment equals the change of the internal energy.

$$\Delta p \delta A dz = \gamma d\delta A \tag{1.9}$$

and,

$$\delta A dz = xydz \tag{1.10}$$

$$d\delta A = xdy + ydx \tag{1.11}$$

From a comparison of similar triangles, it follows that

$$\frac{dx}{x} = \frac{dz}{R_1} \tag{1.12}$$

$$\frac{dy}{y} = \frac{dz}{R_2} \tag{1.13}$$

Substitution of Equ. (1.12, 13) back to Equ. (1.9) will give the Young-Laplace equation.

$$\Delta p = \gamma \left(\frac{1}{R_1} + \frac{1}{R_2}\right) \tag{1.14}$$

For a bubble in a liquid, the pressure difference Δp is $2\gamma/R$, where γ is the liquid surface tension and R is the radius of the bubble.

1.1.3 Kelvin equation

Furthermore, the liquid vapor pressure will also change, if its surface is curved, when compared with the planar surface. The reason for such a vapor pressure difference is the Laplace pressure as described above. Because of the raised Laplace pressure on the curved liquid surface the molecules inside the liquid evaporate more easily than for a planar surface. The Kelvin equation is used to describe this difference of vapor pressure for a curved liquid surface [11]:

$$RTln\frac{p_0^K}{p_0} = \gamma V_m \left(\frac{1}{R_1} + \frac{1}{R_2}\right) \tag{1.15}$$

where p_0^K is the vapor pressure of the curved surface, p_0 is that of the planar surface and V_m is the molar volume of the liquid. Here the index "0" indicates that everything is only valid

in thermodynamic equilibrium. For a bubble (the radius is R) in the liquid, the Kelvin equation can be written as:

$$RTln\frac{p_0^K}{p_0} = \frac{2\gamma V_m}{R} \tag{1.16}$$

1.1.4 Capillary condensation

From the Kelvin equation we can get the expression of capillary condensation. It predicts that vapor will condense in channels of sufficiently small dimensions even when the pressures is below the saturation vapor pressure (p_0) for the liquid in contact with a planar surface.

Here we chose the model of a spherical particle on a planar surface to illustrate capillary condensation as shown in Figure 1.4 [14]. The annular gap between the particle and the planar surface can act as a pore space filled with condensed liquid from the vapor phase. Such a condensation will continue until the meniscus radius of the liquid reaches the value given by the Kelvin equation [11]. It can be written as following,

$$RTln\frac{p_0^K}{p_0} = -\frac{2\gamma V_m}{r_C} \tag{1.17}$$

The vapor pressure of the liquid inside the pore decreases to p_0^K, with $r_C$being the capillary radius where the meniscus is in equilibrium.

Capillary force, also named meniscus force, is a consequence of the capillary condensation of the liquid condensed into the small porous space surrounding the direct contact area. It has many examples, such as two particles adsorbing together by liquid condensing into the gap of the contact area, particles-solid planar surfaces, and planar-planar surfaces.

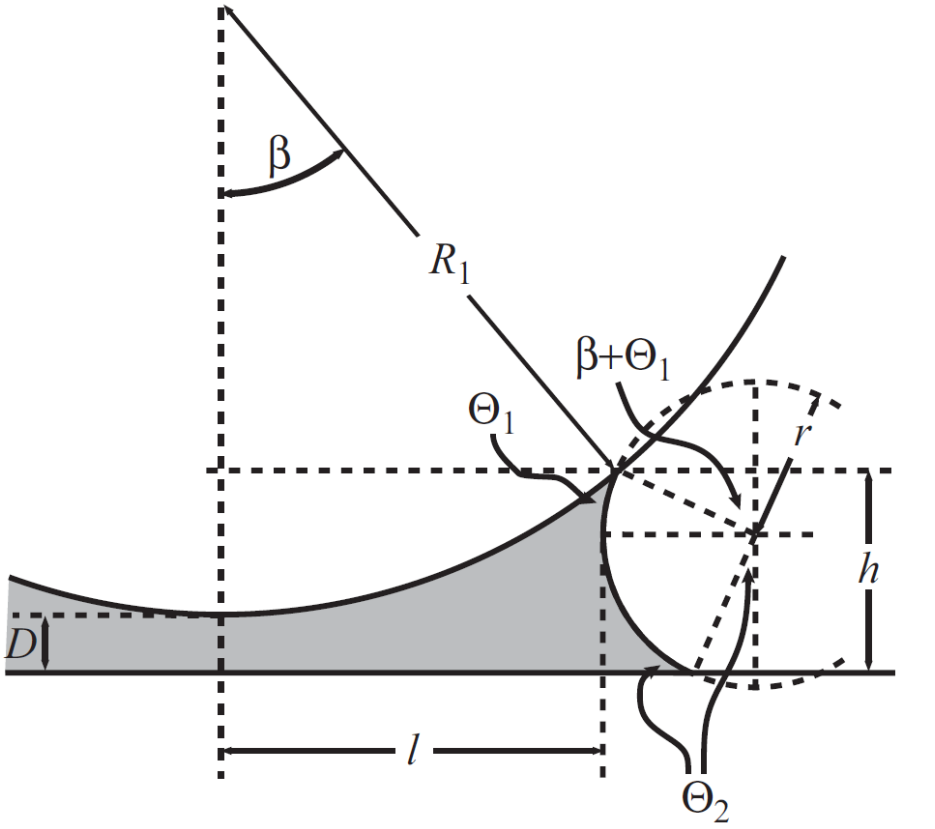

Figure 1.4: Schematic of a spherical particle with radius R_1 on a planar surface which has a distance D. The height of the liquid meniscus is h. The angle β describes the position of the three-phase contact line on the particle surface [14].

Figure 1.4 shows the capillary force in the case of a spherical particle on a planar surface. The curvature of the meniscus liquid is expressed by two radii: the azimuthal radius l and the meridional radius r, perpendicular to each other. So the total radius of curvature of the meniscus liquid surface is $1/l - 1/r$. The pressure is $\Delta p = \gamma\,(1/l - 1/r)$. Since l is bigger than r, the curvature is negative, that means the pressure in the liquid is lower than that of the vapor phase outside. It acts upon the cross sectional area which results in an attractive force of F. So the total capillary force can be written as [14],

$$F = 2\pi l\gamma - \pi l^2 \Delta p \tag{1.18}$$

Here, $2\pi l\gamma$ is the force resulting from the surface tension of the liquid and $-\pi l^2 \Delta p$ is induced by the Laplace pressure. Since capillary forces are always attractive, it is convenient to apply a positive sign to attraction.

In this thesis, we will focus on the capillary condensation effect on particle immobilization on planar substrates.

1.2 Theory of diffusion

Diffusion is the net movement of particles (molecules or atoms) from a region of higher concentration to a region of lower concentration due to the difference of the chemical potential. The gradient is the change of the value of a quantity in the form of concentration, pressure, or temperature as a function of another variable, usually distance. In this thesis, we focus on oxygen molecule formation and diffusion from a single Pt-NP active site by the decomposition of H_2O_2.

1.2.1 Fick´s first law

The rate of matter motion is defined by its diffusion flux, J ($m^{-2}s^{-1}$), which is given by the amount of matter passing through a unit area during a unit time interval. If the matter is diffusing, it means a matter flux of a number of molecules per square meter per second goes from a location of high concentration to a location of low concentration. The diffusive flux of matter is described by Fick´s first law of diffusion [15]:

$$J_{(matter)} = -D\ dN/dz \tag{1.17}$$

where D is the diffusion coefficient or diffusivity of a substance with units of area per unit time (m^2s^{-1}), N is the number density of matter with the units of number per unit volume (m^{-3}), z is the position with unit m.

For a system on the condition of constant temperature and pressure, the maximum non-expansion work that can be done per mole when a substance moves from a location with the chemical potential μ to another location with the chemical potential $\mu + d\mu$ is $dW = d\mu$ [15]. Due to the chemical potential depending on its position x, it can be written as,

$$dW = d\mu = \left(\frac{\partial \mu}{\partial z}\right)_{p,T} dz \tag{1.20}$$

In another way, work also can be expressed by the opposing force (F),

$$dW = -Fdz \tag{1.21}$$

By comparing these two expressions, we write this thermodynamic force as

$$F = -(\frac{\partial \mu}{\partial z})_{p,T} \tag{1.18}$$

For a solution with the activity of the solute *a*, the chemical potential can be expressed

$$\mu = \mu^0 + RT \ln a \tag{1.23}$$

If the solution is not uniform the activity depends on the position and we can write

$$F = -RT(\frac{\partial \ln a}{\partial z})_{p,T} \tag{1.19}$$

If the solution is ideal, *a* may be replaced by the molar concentration *c*, and then

$$F = -\frac{RT}{c}(\frac{\partial c}{\partial z})_{p,T} \tag{1.25}$$

Supposing that the flux of diffusing particles is the motion due to a thermodynamic force resulting from a concentration gradient, the particles will obtain a steady motion speed on the condition that the thermodynamic force is equaled with the viscous drag. So this kind of particles motion speed is proportional to the thermodynamic force. In addition, due to the further proportional relationships of the particle flux J to the particles drift speed and the thermodynamic force to the concentration gradient, it can gain that $J \sim dc/dz$, which is the form of Fick´s first law of diffusion when both sides of Equ. 1.19 are devided by Avogadro´s constant [15].

1.2.2 Diffusion equation

Here is the discussion of time-dependent diffusion processes, where the spreading is inhomogeneous with time. The process is described by the diffusion equation, namely, Fick´s second law of diffusion. By using this equation one can predict how diffusion induces the concentration to change with time. From Fick´s first law and mass conservation, we will obtain this diffusion equation [15]:

$$\frac{\partial c}{\partial t} = D\,\frac{\partial^2 c}{\partial x^2} \tag{1.26}$$

For the solvent (all particles n_0) initially (t=0) concentrated on the surface of area A (location x=0) (this is a 1-D case), the solution of the above diffusion equation can be obtained as:

$$c(x,t) = \frac{n_0}{A(\pi Dt)^{1/2}} e^{-x^2/4Dt} \tag{1.27}$$

1.2.3 Diffusion probabilities

From the solution of the diffusion equation, one can get the net average distance for the particle diffusion in a given time [15]. Deriving from the Equ. 1.27 (1-D diffusion), the net distance travelled on average in the time t for the particles with diffusion constant D can be expressed as,

$$\langle x \rangle = 2(\frac{Dt}{\pi})^{1/2} \tag{1.28}$$

The root mean square distance travelled is [15, 118],

$$\langle x \rangle^{1/2} = (2Dt)^{1/2} \tag{1.20}$$

1.3 Physical optics

In general, classical optics has two categories: geometrical optics and physical optics. In geometrical optics, the light is like a ray, which goes straight. In physical optics, light is like a wave, which is a series of propagating electric and magnetic field oscillations. This model owns the characters such as interference, diffraction and polarization [16-17].

1.3.1 Interference

Interference is the process in which two waves with the same or nearly same frequency superpose to form a resultant wave whose amplitudes are bigger, smaller or the same when compared to the original waves. When two individual waves with similar frequency are traveling and then meeting each other, the superposed wave is the sum of the interfering wave's amplitudes. If the resultant wave has greater amplitude than the individual waves, this is constructive interference. If the resultant wave has a smaller amplitude than the individual waves, it is called destructive interference.

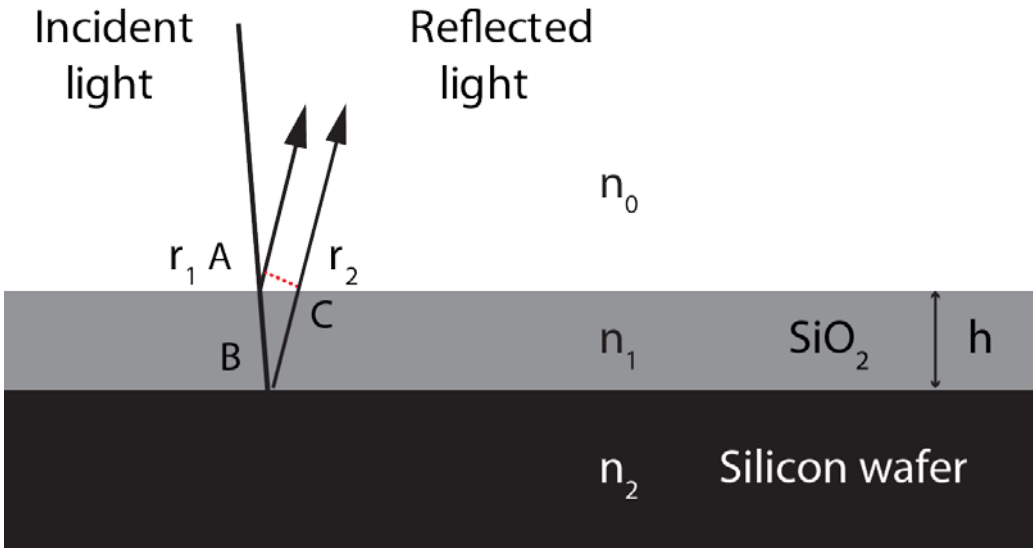

Figure 1.5 Schematic of the two beam interference from the upper and lower boundaries of a thin film (silica film coated on a silicon wafer).

One example is thin film interference in the case of a silica film coated on a silicon wafer, as shown in Figure 1.5. The incident light strikes the surface of a silica film of index n_1 from the medium of index n_0 (generally for air n_0=1) and two light reflecting interferences are created. The incident light at A splits into two parts: refracted and reflected beam. At B of the film/substrate interface, the refracted beam reflects and then divides again into two parts at C. The optical path difference is Δ (AB +BC). When the light incident is nearly perpendicular to the surface, the optical path difference Δ is approximately equal to twice the film thickness 2h, namely,

$$\Delta = 2n_2h \tag{1.30}$$

So constructive interference is on the condition of $2n_2h = i\lambda_0$; destructive interference is on the condition of $2n_2h + \frac{\lambda_0}{2} = (i + {}^1/_2)\lambda_0$, where i is integer [16].

1.3.2 Diffraction

Diffraction is the bending of waves as they pass through an aperture or around an obstacle. It occurs when the wavelength of the incident wave is close to the size of the obstacle or aperture. An example is single-slit diffraction as shown in Figure 1.6. It presents the resultant pattern for light that passes a single slit. The intensity at the center of the pattern is a maximum and the equally spaced regions beside the center become more and more weak. For the slit with width d, the optical path difference is $d/2 \sin \theta$ between the light from top

and the distance *d/2* below. If the value is half a wavelength λ, one can obtain the first order minima of diffraction. If the $d \sin\theta = i\,\lambda$ *(i>1, i* is integer*)*, higher order minima will be seen on the screen [17].

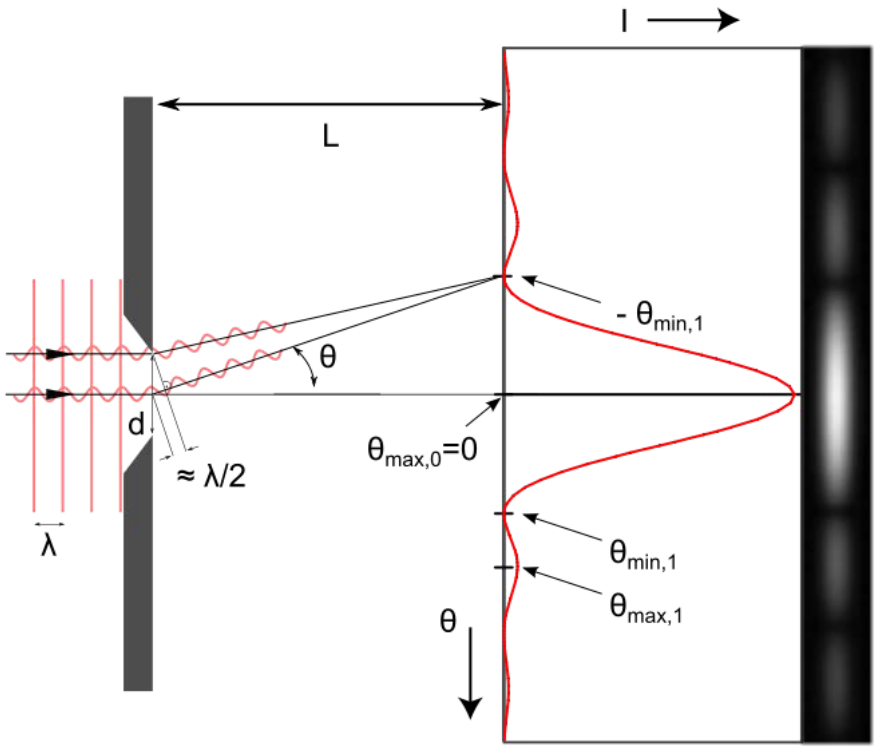

Figure 1.6 Schematic of the diffraction pattern from a slit from an incident planar wave.

The ability of an imaging system to resolve details of sub-wavelength structures is limited by Abbe diffraction limit [17]. When light incident passes through on a circular lens, diffraction occurs. The light is not focused to a point but forms an Airy disk having a bright region in the center in the focal plane. The radius (*d*) to the first minimum of Airy disk is given by

$$d = 1.22\lambda N \tag{1.31}$$

where λ is the wavelength of the light and N is the f-number (focal length f divided by aperture diameter D) of the imaging optics. In object space, the corresponding angular resolution is [17]:

$$\sin\theta = 1.22\frac{\lambda}{D} \tag{1.32}$$

In imaging of two point sources, each will produce an Airy pattern. As the two points move closer together, the Airy patterns will start to overlap, and finally they will merge to form a single pattern, at which case the two point sources cannot be resolved in the image [17]. The Rayleigh criterion specifies that two point sources can be considered to be resolvable if the separation of the lens, and the smaller the wavelength, the finer the resolution of an imaging system.

1.4 Theory of nucleation

Nucleation is the beginning of a first-order phase transition by which a metastable phase transforms into a more stable one [18-21]. This phase transition is initiated by a random fluctuation that overcomes the energy barrier which is required to form the nuclei of the new phase. Once the nuclei of the new phase forms, further growth is energetically favorable. In general, nucleation can be of two types: homogeneous or heterogeneous (induced by "foreign" surfaces). Classical nucleation theory, which is original from the work of Volmer and Weber, Farkas, Becker and Döring[17-22], is a widely used approximate theory for estimating such processes.

1.4.1 Homogeneous nucleation

Homogeneous nucleation occurs when clusters of the new phase (β) are only in contact with the old phase (α). For an ideal spherical cluster of radius *r*, the total free energy ΔG_T is balanced by two competitive factors, the volume free energy ΔG_V and the interfacial energy ΔG_I due to the formation of the new surface, as shown in Figure 1.7:

$$\Delta G_T = \Delta G_I + \Delta G_V = 4\pi r^2 \cdot \gamma + \frac{4}{3}\pi r^3 \cdot \Delta g_v \tag{1.33}$$

where *r* is the nuclei radius, γ is the interfacial energy (per unit square) and $\Delta g_v = \frac{\mu_\beta - \mu_\alpha}{V_M}$ is the volume free energy (per unit volume), μ_α and $\mu_ß$ are the potentials of old phase and new phase.

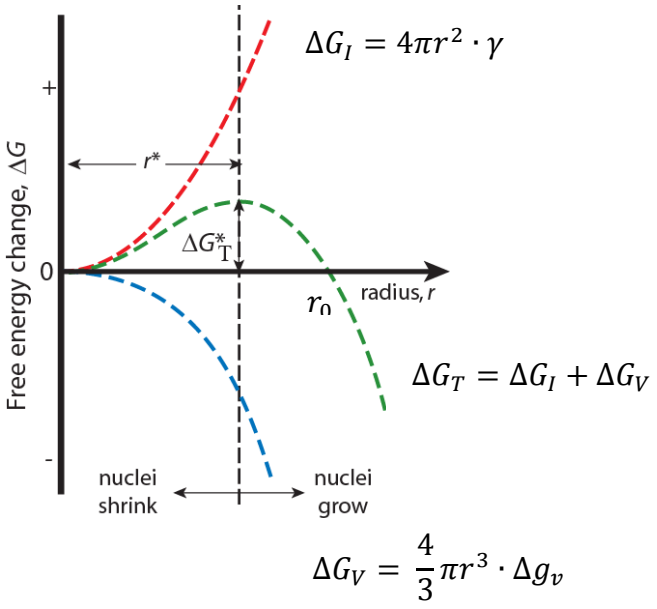

Figure 1.7 The dependence of the cluster free energy, ΔG, on the cluster radius, r.

Initially free molecules or atoms form clusters (nucleus). As the clusters grow, ΔG_T increases mainly dominated by the rapid increase in surface energy, implying that the particle growth is not thermodynamically favorable. Thus most of the clusters dissolved back to the old phase. Once some of the clusters reach the size of a critical r^* and pass the barrier of free energy, further growth of these clusters will lead to a decrease in free energy, a tendency favorable for the continuous growth, even though ΔG_T in this regime before reaching the size of r_0 is still > 0. After passing r_0, ΔG_T will become negative and the growth of clusters will be highly favored and eventually lead to the formation of a bulk-phase.

The maximum value of ΔG_T corresponds to the critical nucleus, r^*. For a spherical cluster it is obtained as following:

$$\frac{d\Delta G_T}{dr}\Big| r^* = 8\pi r \cdot \gamma + 4\pi r^2 \cdot \Delta g_v = 0 \tag{1.34}$$

Thus:

$$r^* = \frac{-2\gamma}{\Delta g_v} \tag{1.35}$$

From Equ. 1.34 and 1.35 we get:

$$\Delta G_T^* = \frac{16\pi\gamma^3}{3(\Delta g_v)^2} = \frac{4\pi\gamma {r^*}^3}{3} \tag{1.36}$$

Here ΔG_T^* is the nucleation barrier for new phase formation. Beyond r^*, ΔG_T^* decreases with increasing *r*, and at r_0,

$$\Delta G(r_0) = 4\pi {r_0}^2 \cdot \gamma + \frac{4}{3}\pi {r_0}^3 \cdot \Delta g_v \tag{1.37}$$

Then we have,

$$r_0 = \frac{-3\gamma}{\Delta g_v} \tag{1.38}$$

When a cluster´s size grows to r_0, the nucleation barrier is zero. The nucleation continues as the ΔG_T will become < 0 (thermodynamically favorable) after passing r_0.

1.4.2 Heterogeneous nucleation

Heterogeneous nucleation occurs much more often than homogeneous nucleation. The reason is that there are always impurities like microscopic particles or phase boundaries in the old phase which are active as nucleation sites, thus diminishing the free energy barrier and facilitating nucleation. At such preferential sites, the effective surface energy is lower, thus diminishing the free energy barrier and facilitating nucleation.

The free energy change of the nucleation process depends on the scenario. Assuming that the nucleus is a truncated spherical with radius *r*, the total free energy change is:

$$\Delta G_T = \Delta G_I + \Delta G_V = \left[\gamma_{\alpha\beta} A_{\alpha\beta} + \left(\gamma_{\beta\delta} - \gamma_{\alpha\delta}\right) A_{\beta\delta}\right] + V_\beta \Delta g_V \tag{1.39}$$

where α, β, δ are the surface tension of old phase, new phase, and new phase-substrate boundary, respectively.

From the Young equation, we have

$$\left(\gamma_{\beta\delta} - \gamma_{\alpha\delta}\right) = -\gamma_{\alpha\beta}\cos\theta \tag{1.40}$$

where θ is the contact angle of the new phase on the surface.

From the results of geometrical computation, we then have

$$\Delta G_T = \left[4\pi r^2 \cdot \gamma_{\alpha\beta} + \frac{4}{3}\pi r^3 \cdot \Delta g_v\right] \cdot \left[\frac{2 - 3\cos\theta + \cos^3\theta}{4}\right] \tag{1.41}$$

namely

$$\Delta G_{T_{heter}} = \Delta G_{T_{heter}} f(\theta) \tag{1.42}$$

with

$$f(\theta) = \frac{2 - 3\cos\theta + \cos^3\theta}{4} \tag{1.43}$$

Here we can see that the height of the nucleation barrier is a function of the contact angle. When θ is π, it is the same as with homogeneous nucleation. Otherwise, the critical Gibbs free energy change for heterogeneous nucleation is always smaller than for homogeneous nucleation.

1.4.3 Nucleation of a bubble in a liquid

Bubble nucleation can be described by classical nucleation theory [23-29]. One common example is bubble nucleation in liquid at the boiling point [23-24].

1.4.3.1 Homogeneous nucleation of bubble

To create a bubble with the volume of V in a liquid means the creation of a new interface with the successive transfer of molecules from the liquid into the bubble. Firstly we study the minimum work, W, required to create a bubble which contains n gas molecules inside. The maximum work available from the vaporization of n gas molecules is by a reversible path at the vapor pressure, P_V, of the liquid under am ambient pressure, P_L, at which n molecules of gas having the volume, $V_G^{'}$. W_1 is [23]:

$$W_1 = (P_V - P_L)V_G^{'} \tag{1.44}$$

when the bubble is not in chemical equilibrium with the liquid, then at equilibrium its volume, V_G, different from $V_G^{'}$. If the volume is changed from $V_G^{'}$ to V_G while keeping the number of molecules inside same, then the work done on the environment is W_2 given by [23]:

$$W_2 = \int_{V_G'}^{V_G} (P - P_L)\, dV_G = P_G V_G - P_G V_G' - P_L\left(V_G - V_G'\right) - \int_{P_V}^{P_G} V\, dP \qquad (1.45)$$

and $\int_{P_V}^{P_G} V\, dP$ can be expressed as $n(\mu_L - \mu_G)$, where P_G is the pressure inside the bubble, μ_L and μ_G are the potentials of liquid phase and gas phase.

Thus, the minimum work, *W*, required to create a bubble with the surface of $A(n)$ is the work to create the interface, being expressed in terms of less the maximum work done by the expanding gas [23]:

$$W = \gamma A(n) - W_1 - W_2 = \gamma A(n) - (P_G - P_L)V_G + n(\mu_G - \mu_L) \qquad (1.46)$$

If the rate of growth or collapse of a bubble is governed only by the rates of vaporization or condensation, the bubble will be in mechanical equilibrium satisfying as following,

$$P_G = P_L + \frac{2\gamma}{r} \qquad (1.47)$$

where *r* is the radius of the bubble.

1.4.3.2 Heterogeneous nucleation of bubble

Under many situations in which bubbles form, they are nucleated heterogeneously at the "foreign" interface. The conditions of such heterogeneous nucleation depend on the structures of the surface and liquid interfacial tensions. For example, nucleation happened at plane rigid surfaces. The minimum work to create the lens-shaped vapor embryo at a planar rigid surface is [24]:

$$W = \gamma_{LG} A_{LG} + (\gamma_{SG} - \gamma_{SL}) A_{SG} - (P_G - P_L)V_G + n(\mu_G - \mu_L) \qquad (1.48)$$

where *L, G, S* indicate for liquid, gas, and surface, respectively,

$$V_G = \frac{4}{3}\pi r^3 \cdot \left[\frac{2 - 3\cos\theta + \cos^3\theta}{4}\right] = \frac{4}{3}\pi r^3 \cdot f(\theta) \qquad (1.49)$$

where θ is the contact angle of the bubble on the surface.

$$A_{SG} = \pi r^3 \cdot [1 - \cos^2\theta] \qquad (1.50)$$

$$A_{LG} = 2\pi r^2 \cdot [1 + \cos\theta] \tag{1.51}$$

The equations which express the force balance at the edges of the bubble are:

$$\cos\theta = \frac{\gamma_{SG} - \gamma_{SL}}{\gamma} \tag{1.52}$$

2. Experimental Details

2.1 Materials, synthesis, and preparation details

2.1.1 Chemicals and materials

Hexachloroplatinic acid hydrate ($H_2PtCl_6 \cdot 6H_2O$, ⩾ 99.9%), L-ascorbic acid ($C_6H_8O_6$, 99%), trisodium citrate dihydrate ($C_6H_5Na_3O_6, \cdot 2H_2O$ ⩾ 99%), sodium borohydride ($NaBH_4$, ⩾ 96%), sodium citrate, citric acid, sodium borohydride and 3-(aminopropyl) triethoxysilane (APTES) were purchased from Sigma-Aldrich. Fullerene (C_{60}, ⩾ 99.9%) was purchased from Alfa Aesar. Poly (methyl methacrylate) (PMMA, average Mw ~45,000) and polystyrene (PS average Mw ~45,000) were purchased from Polymer Source Inc. The chemicals were used without further purification. Deionized (DI) water (18.2 MΩ) obtained from a SG-ultra pure water system was used in all experiments.

Silicon wafer with artificially grown oxide layers of ~ 50nm, 100 nm, 300 nm and without oxide layer were purchased from Silchem (Freiberg, Germany).

2.1.2 Silicon substrate cleaning

Prior to sample silanization, pieces of silicon wafers (1.5 cm × 1.5 cm) were cleaned by using a ultrasonication bath (100 W, 80 Hz, Elmasonic P 60H) applying the following sequence: 10 min in DI water, 10 min in ethanol, 10 min in acetone, 10 min in ethanol, and 10 min in DI water. These substrates were then immersed for 25 min in a freshly prepared piranha solution (H_2O_2 (35%) / H_2O (65%) and 96% H_2SO_4, 1:3 ratio). The substrates were then thoroughly washed in DI water for 10 min and were stored in DI water before use (storage time at most two days).

2.1.3 Synthesis of Pt NPs and Au NPs

(A) Synthesis of Pt NPs (~23 nm)

A platinum suspension was prepared in aqueous solution following a seed-mediated growth procedure according to Bigall et al [103]. At the beginning, Pt NP seeds of about 4.5 nm in diameter were prepared. 7 mL of 4 mM chloroplatinic acid solution was added to 97 mL boiling DI water in a 100 mL round-bottom flask. After 1 minute, 2.2 mL of an aqueous solution containing 1% (w/w) sodium citrate and 0.05% (w/w) citric acid was added, followed half a minute later by a quick injection of 1.1 mL of a freshly prepared 0.08% w/w

sodium borohydride solution (also containing 1% sodium citrate and 0.05% citric acid). After 10 minutes, the sol solution was cooled down to room temperature. The Pt-NP seeds obtained in this way were used as seeds for preparing the larger Pt-NPs (diameter about 23 nm) used in this paper. To this end 1 mL of the Pt-NP seed solution was added to 29 mL of DI water at room temperature. Then 90 μL of a 0.2 M chloroplatinic acid solution and 0.5 mL of a 1.25% L-ascorbic acid solution containing also 1% sodium citrate were added step by step. The mixture was slowly heated to the boiling point (~10 ºC/min) and left to react for 45 minutes with stirring. Then it was cooled to room temperature. The reaction product was collected by centrifugation, washed three times with DI water and stored.

(B) Synthesis of big Pt NPs (~50 nm / 70 nm / 100 nm)

The Pt-NPs (~23 nm) obtained in the above way were used as seeds for preparing the larger Pt-NPs (diameter about 50 nm). To this end 4 mL of the Pt-NP seed (~23 nm) solution was added to 26 mL of DI water at room temperature. Then 90 μL of a 0.2 M chloroplatinic acid solution and 0.5 mL of a 1.25% L-ascorbic acid solution containing also 1% sodium citrate were added step by step. The mixture was slowly heated to the boiling point (~10 °C/min) and left to react for 45 minutes with stirring. Then it was cooled to room temperature. The reaction product was collected by centrifugation, washed three times with DI water and stored. The diameter of the above particles is about 50 nm. The same procedure using 1 and 0.25 mL of 23 nm seed solution in 29 mL of water resulted in particles of 70 and 100 nm diameter, respectively.

(C) Synthesis of big Pt NPs (~140 nm / 200 nm)

0.5 mL of the Pt-NPs (~50 nm) solution was added to 29 mL of DI water at room temperature. The other procedures are same. The diameter of the particles is about 140 nm. The same procedure using 0.5 mL of the Pt-NPs (140 nm) in 29 mL of water resulted in particle of 200 nm.

(D) Synthesis of Au NPs

Gold colloids were prepared according to Frens [104]. 30 mL of an aqueous solution of 0.5 mM $HAuCl_4$ solution was given into a 100 mL Erlenmeyer flask on a stirring hot plate and brought to a rolling boil. To the rapidly-stirred boiling solution, quickly 3 mL of a 0.25% aqueous solution of sodium citrate dehydrates were added. As a result gold colloids form as the citrate reduces the gold ions. The total reaction time is about 10 minutes. The dispersion

was cooled to room temperature. The Au-NPs were collected by centrifugation and washed three times with DI water and then stored.

2.1.4 Immobilization of NPs on silicon substrates through APTES

(A) Conventional route

Surface amino-silanization of the oxidized silicon wafer surface was done by chemical vapor deposition (CVD) with APTES. The silanization process was performed in a standard desiccator (volume about 1 L). Before evacuation of the desiccator, the freshly cleaned silicon wafers were placed with the polished side up on a petri dish inside the desiccator near the perimeter. Then a small beaker with 20 μL of APTES was placed inside the desiccator at its center. Then the desiccator was closed, the pump was started and running continuously for 2 hours, keeping the residual pressure inside the desiccator at about 20 mbar. Then the substrates were taken out of the desiccator, rinsed for 10 min in anhydrous ethanol (to get rid of any APTES in excess of a monolayer). Then the samples were annealed for about one hour at 100 ºC in normal atmosphere.

Deposition of the NPs onto the amino-silanized silicon wafer substrates was achieved by immersing the substrates into the colloidal suspension of Pt NPs for 3 hours. After that the silicon wafer substrates were rinsed with DI water three times to wash off loosely attached Pt NPs.

(B) New route

Pt NPs were deposited onto silicon substrates by spin casting with the aqueous NPs solution. It should be noted that the deposition of the NPs onto the hydrophilic silicon substrate surface could also have been done by immersion of the substrates (dip coating), as in the case of the conventional approach. However, spin coating is a much better defined deposition process and allows a better control of the NP coverage. Therefore it was preferred to immersion/dip coating. Regarding the NP deposition, spin casting and dip casting essentially provide identical processes i.e., the drying of a thin film containing NPs. Because it is better controllable, we would have preferred to use always spin casting. But with the conventional approach spin casting could not be applied, because with hydrophobic, amino-silanized surfaces the hydrophilic aqueous liquid drops deposited onto the rotating sample simply roll off.

The surface amino-silanization of the substrates pre-coated with the NPs was identical to procedure 1.) described in the conventional route above.

2.1.5 Immobilization of NPs on silicon substrates through fullerene (C_{60}) or polymers

Firstly, Pt NPs were deposited onto silicon substrates by spin casting with the aqueous NPs solution. Then we spin casting with either 5×10^{-5} M C_{60} in toluene at rotating speed 1000 rpm, 4×10^{-4} w/w PMMA or 4×10^{-4} PS in toluene at rotating speed 3000 rpm to the silicon substrate which were pre-coated with the NPs.

2.1.6 Ultrasonic test

The adhesion of NPs immobilized on the substrates was tested by immersing the NP coated silicon substrates (kept in place by a holder) in a 100 ml beaker filled with DI water. The beaker was placed in an Elmasonic P 60H cleaner (100 W) partially filled with water.

2.1.7 Characterization of NPs coated substrates

A JEM2100 transmission electron microscopy (TEM) was used to image the morphology and size of Pt and Au-NPs. Samples for TEM were prepared by placing a drop of NP solution on a carbon coated copper grid. The NP size distribution was measured with Image J software through determining the diameter of at least 100 randomly selected particles for each sample. Scanning electron microscopy (SEM) images of the colloidal Pt and Au NPs were used for the determination of the NP coverages on planar substrates prepared by spin casting. For each sample, the coverage of at least five different regions was measured and the average coverage and the standard distribution were determined. A JPK Nanowizard 4 atomic force microscopy (AFM) was used to measure the same substrate surface regions before and after the ultrasonication treatment (the test for the NP adhesion respectively NP immobilization).

2.2 Experiment techniques

2.2.1 Atomic force microscopy

Atomic force microscopy (AFM) or scanning force microscopy (SFM) is a very high resolution type of scanning probe microscopy (SPM), with demonstrated resolution on the order of fractions of a nanometer [63]. As depicted in Figure 2.1, a typical AFM system consists of a cantilever probe with a sharp tip mounted to a piezoelectric (PZT) actuator and

a position sensitive photo detector for receiving a laser beam reflected off the end-point of the beam to provide cantilever deflection feedback [115]. The principle of AFM operation is that the interactions like van der Waals, capillary, steric, electrostatic or electromagnetic between tip and surface can be detected by the form of the deflection of the cantilever when the tip scans the sample surface. As the tip scans the surface of the sample, moving up and down with the contour of the surface, the laser beam reflected by the cantilever is detected by a properly positioned, four sector photodiodes. Feedback from the photodiode difference signal gives the tip the precise position by maintaining either a constant force or constant height above the sample. In most of the cases, piezoelectric tube actuators perform the scanning by moving the sample or the probe over the sample. In the constant force mode, the PZT transducer monitors real time height deviation. In the constant height mode, the deflection force on the sample is recorded.

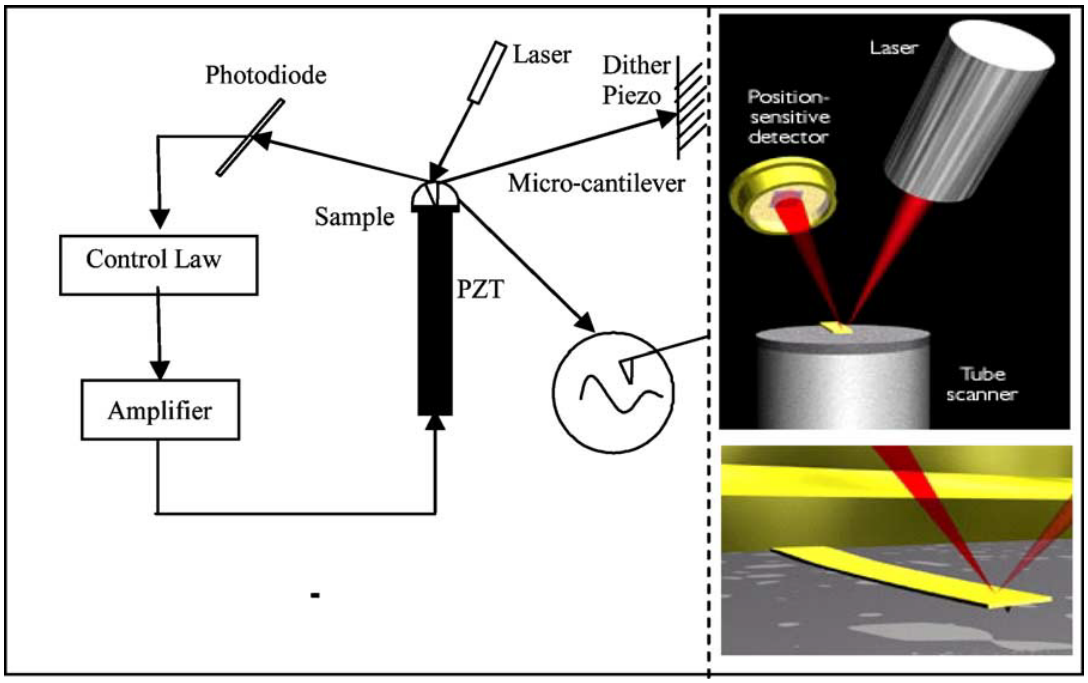

Figure 2.1: Schematic of basic AFM operation [115].

2.2.2 Optical interference-enhanced reflection microscopy

By using a planar, suitably oxide layered surface the reflected intensity contrast can be increased significantly between bare surface areas and regions covered by thin objects [74, 78]. To have the best contrast for small changes of the thin transparent objects, we use an

artificially grown oxide (silica) layer of 50 nm (responding to the laser wavelength: 450 nm) on silicon wafers.

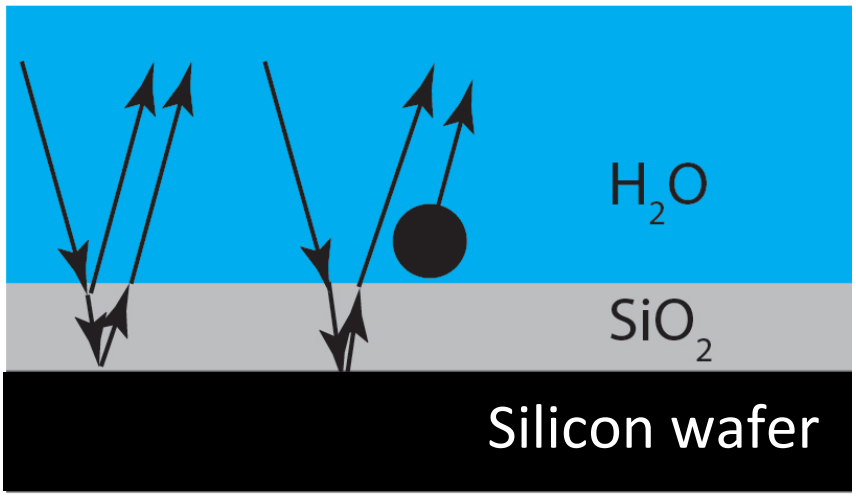

Figure 2.2: Schematic diagram of the optical interference-enhanced reflection microscopy.

As shown in Figure 2.2, when the light passes through the liquid, it will reflect at the interfaces of liquid-silica and silica-silicon. The reflected intensity from the interference of the beams can be enhanced by the silica coated layer [74]. The reflectivity contrast between the regions with and without particles can be distinguished. Using imaging techniques, such as background subtraction, oversampling, and other, the contrast can be amplified.

3. Immobilization of Metal Nanoparticles on a Planar Substrate with High Mechanical Stability

3.1 Introduction

The assembly of metallic or semiconductor NP coatings on different solid substrates to impart desired novel chemical or physical properties is an important technique in the development of new composite and functional materials. Among these fields, metal nanoparticles (NPs) films with controlled nanostructure and composition are intensely investigated due to their potential to novel applications in catalysis, chemical sensing, electrochemistry, or devices [1-4, 31-36]. One of the requirements in many of the aforementioned applications is to make NPs attached to a tangible substrate. However, a key aspect of such system is their adverse mechanically stability. As we known, NPs will eventually detach because of the weak adhesive interaction between them and the substrate. This will lead to unstable-coatings that will lose functionality during repeated uses or induce the environmental problems. In recent years, there has been rapidly increasing attention into improving the mechanical stability of NPs coatings such as thermal embedding, calcination, atomic layer deposition, and covalent chemical bonding [5-7, 37-41]. However, most of these methods have the drawbacks that they destroy the structure of nanomaterials and influence their application. Among these methodologies, the most-reported efforts are the approaches of covalent or electrostatic interaction between particles and a substrate modified through one kind of coupling agent for example APTES, because it is facile and doesn´t destroy the NPs´ intrinsic property. However, the development of efficient methods for the highly mechanical stability of NPs films on the substrate still remains of great interest.

In this chapter, we demonstrate a new strategy to realize the rapid and large-area fabrication of stable coating of metal NPs on silicon substrate with high stability via changing the adding sequence of coupling agent (APTES). Unlike in the traditional approach where the coupling agent is introduced in the beginning, our approach introduces a new sequence to render APTES selectively attach and couple in the interface between NP and substrate to improve the interfacial bonding. In addition, we try to spin cast the polymer and fullerene solution to immobilize NPs due to the similar reason of capillary condensation. We use ultrasonic test to check the mechanical stability of immobilized NPs [36]. AFM was applied to precisely check the NPs´ coverage before and after such test at the same site. We prove that this new proposal has more mechanical stability than conventional approach.

3.2 Pt NPs immobilization

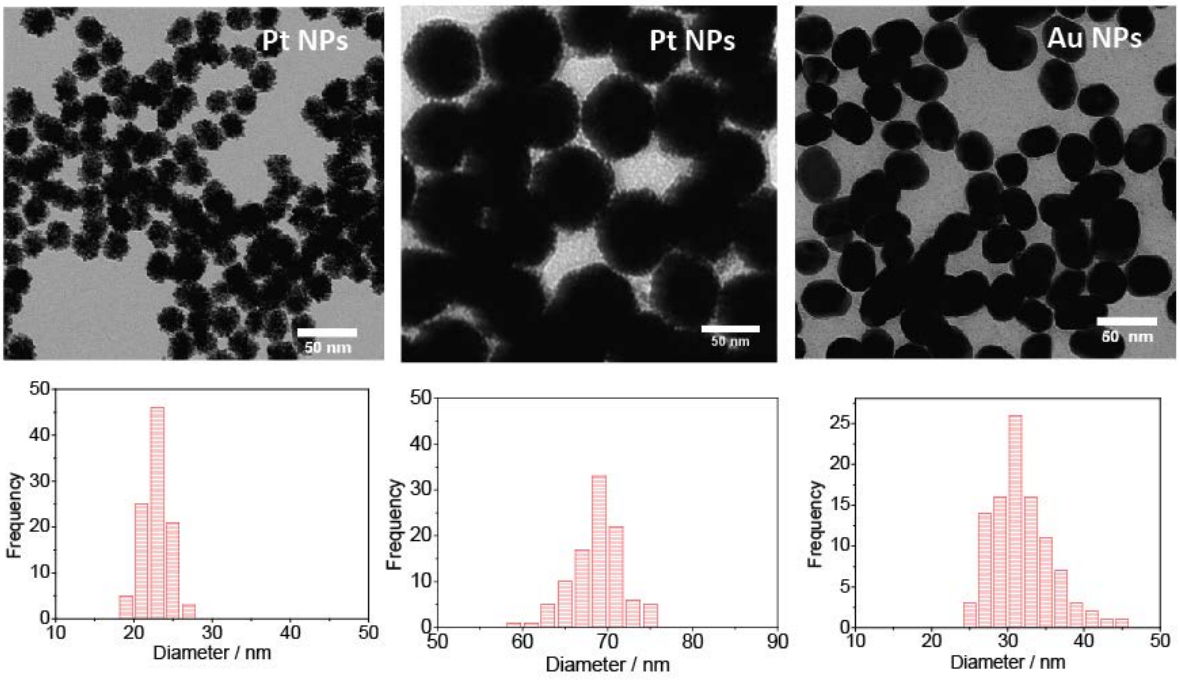

Figure 3.1: Transmission electron microscopy (TEM) images (the upper row) of Pt and Au NPs and their size distributions (the down row).

The details of the NPs synthesis were described in Chapter 2. The size and morphology of the different platinum (Pt) and gold (Au) NPs used in this chapter were determined by TEM mearsurement as shown in Figure 3.1. The size distribution of the NPs was analyzed from the TEM images. To this end, 100 NPs were counted for each case. As shown in Figure 3.1, the size distribution of particles with 23±1.1 nm, 70±3.9, 30±3.1 nm for the small, big Pt NPs and Au NPs.

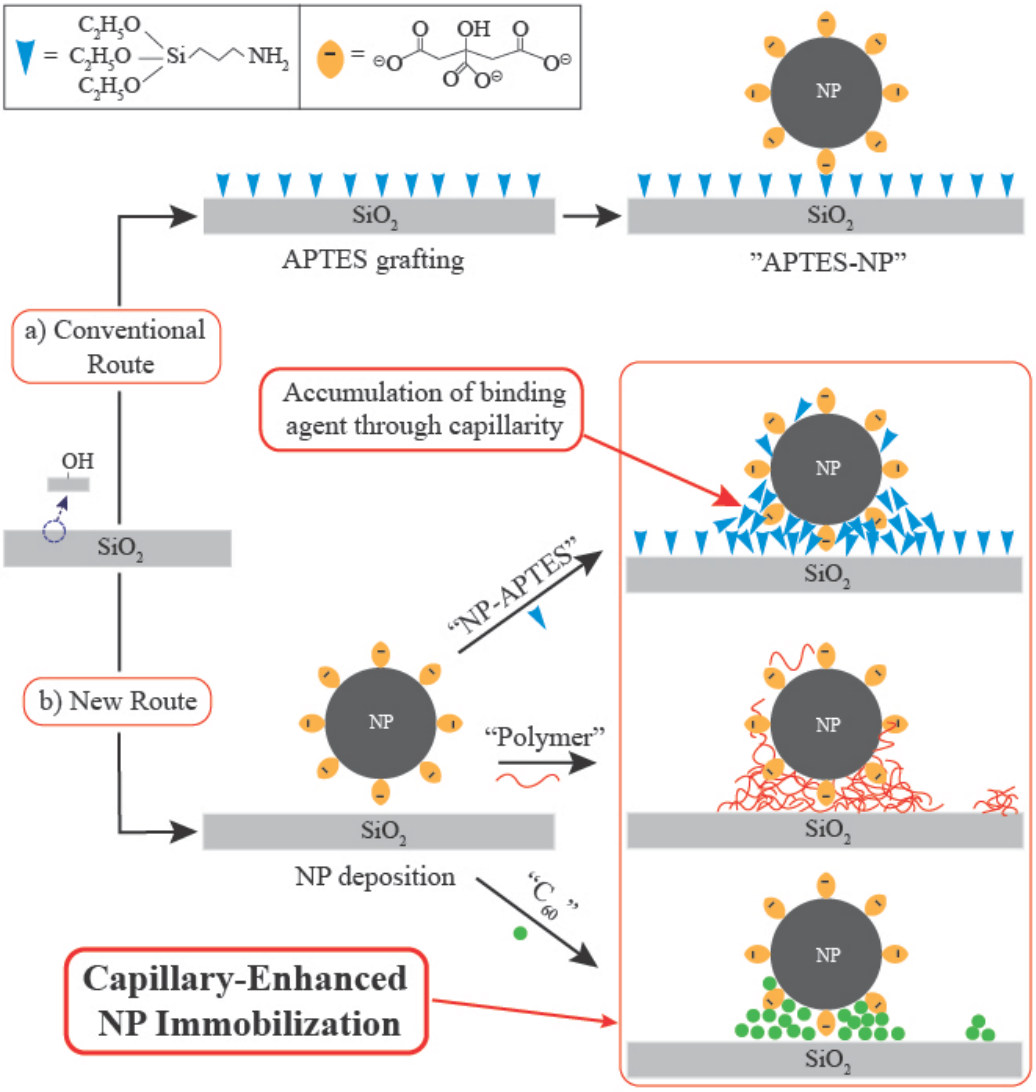

Figure 3.2: Sketch of the fabrication process for nanoparticles immobilized on the silicon substrate with conventional way (upper) or our new proposal (down).

3.2.1 Conventional way

In the conventional route the hydroxylated silica surface was first coated with a thin (molecular) layer of APTES. For a smooth surface coating this was preferentially done by chemical vapour deposition (CVD) [42-43]. The amino-silanized silicon wafers were immersed into the colloidal suspension of Pt NPs for the purpose of getting the NPs coated on the substrate [44-45]. Then, these silicon wafers were rinsed with DI water for three times to remove the Pt NPs excess. As depicted in Figure 3.2 the immobilization of the NP on the substrate is dominated by the cross-link between the amine of the APTES and the citrate attached to the NP. Because APTES as well as citrate supposedly form a thin

(monomolecular) film, links between substrate and NP are limited to the rather small area of direct contact between the planar substrate and the spherical NP.

3.2.2 New proposal

In the new approach, the sequence of preparation steps is changed. The NPs are deposited on the silica substrates before the surface is exposed to the coupling agent. They are deposited from an aqueous solution by evaporative spin casting, which allows a precise control of the NP coverage [46-47]. The NPs adhere (weakly) to the bare silica surface because of VdW interactions. The coupling agents are deposited on the substrate after the deposition of the NPs on the substrate. Three types of coupling agents were applied: 1.) a widely used cross-linking monomer (APTES), 2.) polymers, such as polystyrene (PS) or polymethylmethacrylate (PMMA), and 3.) a monomer (C_{60} fullerenes). APTES was applied by CVD from the gas phase, as in case of the conventional approach. The polymers as well as the C_{60} monomer were deposited by evaporative spin casting from solution with a volatile hydrophobic solvent (typically toluene). The spin cast conditions were adjusted to obtain only a very low overall surface (submonolayer) coverage of the polymers respectively C_{60} monomers.

3.3 Adhesion stability

To test the adhesion of NPs immobilized on substrate, the NPs coated silicon substrate was immersed in a 100 ml beaker that was filled with DI water with a holder inside. The beaker was put in an Elmasonic P 60H cleaner for specified periods of time. And then we use AFM and SEM to measure the NP coverage change between before and after ultrasonication.

3.3.1 AFM in-site image

Firstly, we estimate the incubation time influence on the APTES interfacial bonding between NPs and substrate during APTES gas-phase deposition in the vacuum vessel. The adhesion strength of the Pt NP coatings on the silicon substrate was investigated by a simple but effective ultrasonic test. The NP coated substrates were first immersed into a beaker that was filled with DI water. The beaker was put in the ultrasonic cleaner for a certain time during the test. Atomic force microscopy (AFM) was applied to check the density change of NP before and after such ultrasonic test. Here, we compared the very same place before and after ultrasonication using the AFM measurement with a home-made positioning stage. First, we measured a certain region with AFM. Then the sample was taken out to ultrasonic test.

Then the sample was brought to the AFM after ultrasonic test and measured that region again using the positioning stage. The results were shown in Figure 3.3. For 5 minutes of APTES CVD, there were certain parts of whole NPs remaining on the silicon substrate. However, just enduring 10 minutes of APTES CVD, most all of the NPs in our scanned region still remained at the same place after the above same test. To further prove this result, longer incubation time experiments were done by the same way. It is worth noting that the same results were shown from 15 to 30 minutes of APTES CVD. It indicated that such NPs immobilized system owes high mechanically stable just on the condition of such short 10 minutes of APTES CVD.

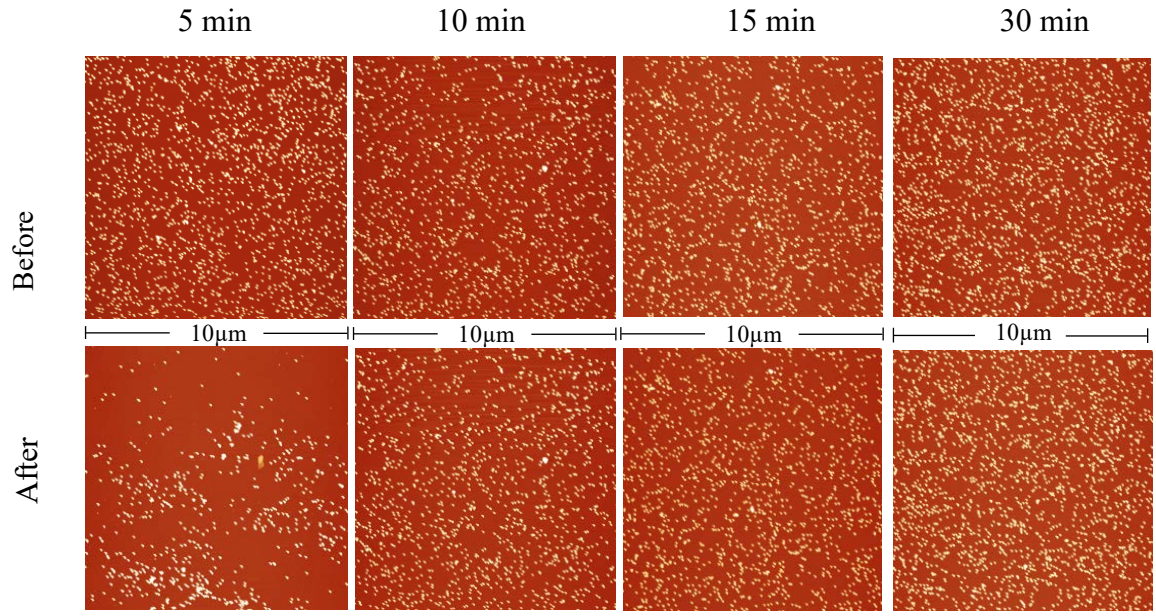

Figure 3.3: AFM images of the Pt NPs immobilized on silicon substrate with different APTES CVD time: from 5 min to 30 minutes before and after 30 minutes of ultrasonication. The scanned regions are 10 μm×10 μm.

We compared the conventional method for NP immobilization with our new proposal. As shown in Figure 3.4., most parts of NPs were washed away after ultrasonic test to the conventional strategy. For the case without posting cross linking agents, there were nearly most all of NPs washed away from the silicon substrate after the ultrasonic test. However, for only 10 minutes of APTES CVD, nearly all of the Pt NPs were still at the same sites after ultrasonic test.

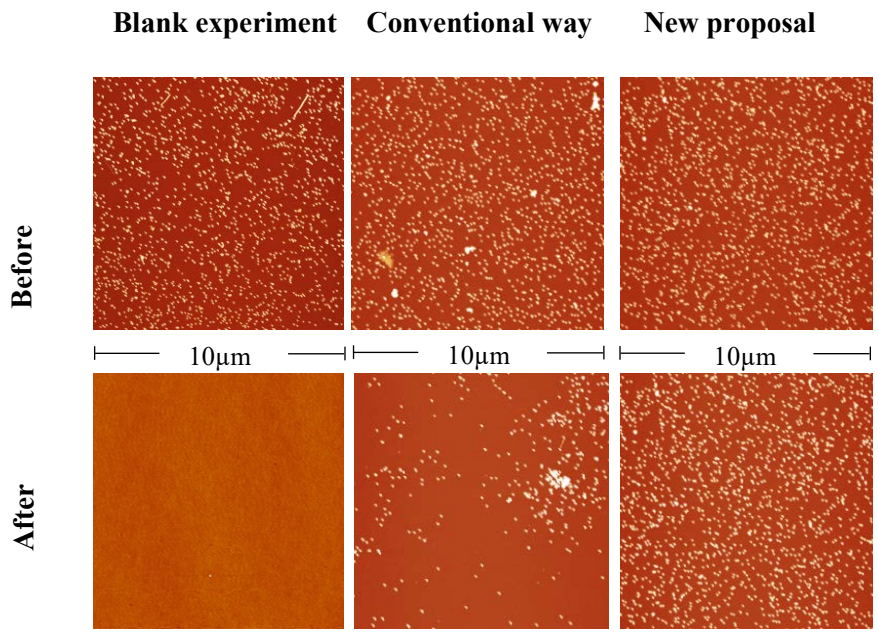

Figure 3.4: AFM (in site) images of the Pt NPs in blank test, the conventional approach and new proposal presented in this chapter (from left to right) before and after 30 minutes at 100 W, 37 Hz ultrasonic test (from up do down). The area for AFM images are 10 µm × 10 µm.

3.3.2 SEM images

In order to double check more thoroughly, we used SEM measurements to get the NPs´ coverage change of the different immobilization strategies. It also showed the similar result that is in accordance with AFM images. As shown in Figure 3.5, we can see that even if the incubation time for APTES CVD is only 10 minutes, the NPs still had very good resistance to the washing by ultrasonic cavitation. From 10 to 30 minutes APTES CVD, the densities of NPs were nearly the same between before and after 30 minutes ultrasonication. However, for the usual method where the NPs got immobilized on the substrate by immersing the APTES modified silicon substrate into the Pt NPs solution for 6 hours, most of NPs were removed by ultrasonication.

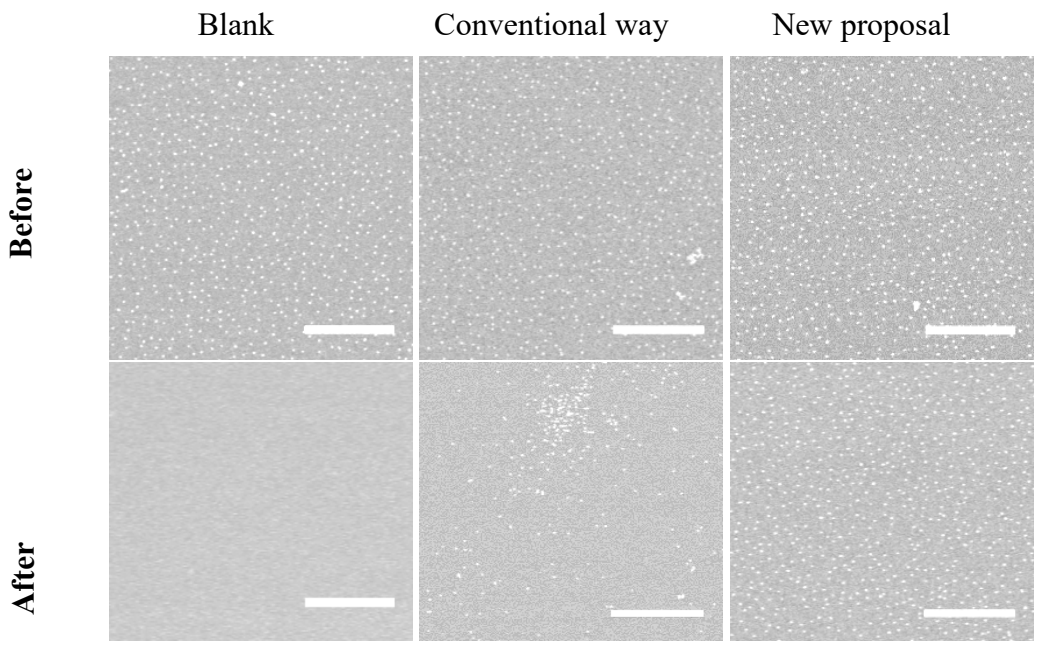

Figure 3.5: SEM images of the Pt NPs in blank test, the conventional approach and new proposal presented in this paper (from left to right) before and after 30 minutes ultrasonic test. The scale bar is 1 µm.

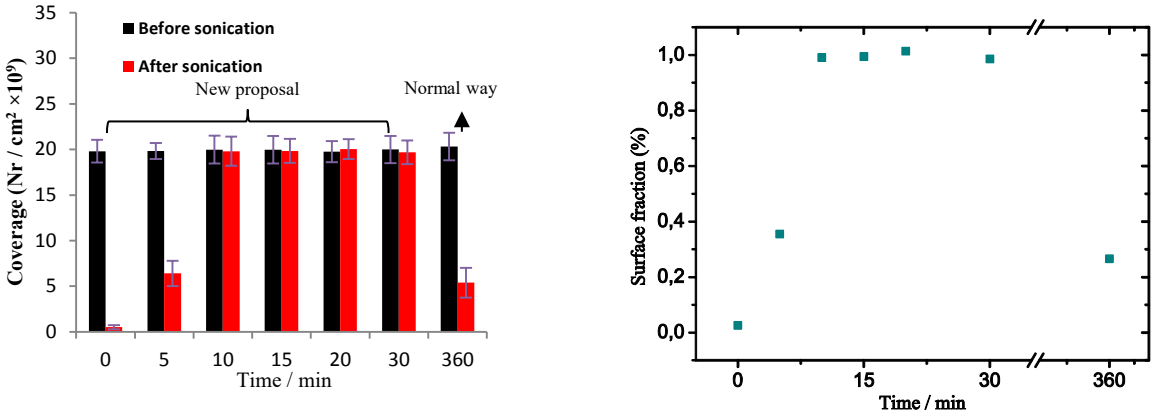

Figure 3.6: The densities of Pt NPs before and after an ultrasonic test time of 30 minutes for the new proposal (From 0 to 30 minutes of APTES CVD) and conventional way (360 minutes are the immersing time for surface amino-functionized-substrate in Pt NPs solution).

The percentages of NPs number retained after the ultrasonic test are presented in Figure 3.6. It shows that 98.9 % to 100 % of the NPs were retained when the APTES CVD time was higher than 10 minutes. However, the sample of NPs immobilized on silicon substrate by the conventional strategy was only 26.5 %. For the blank experiment (without any cross-linking

agent), nearly most of NPs were washed away after the ultrasonic test. It proves that the new strategy for immobilization of NPs has much higher stability than the traditional approach.

3.3 Polymer and fullerene (C_{60}) cases

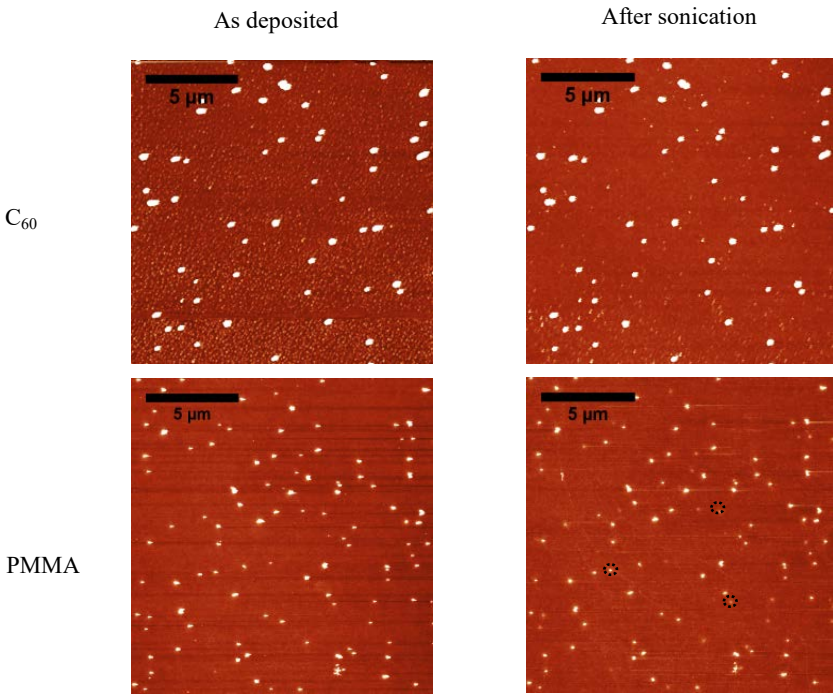

Figure 3.7: Comparison of the Pt-NP adhesion strength between samples with NP deposition with spin casting of fullerene (C_{60}) and PMMA.

Figure 3.7 presents the adhesion strength for the cases of fullerene (C_{60}) and PMMA. The left column shows the surfaces covered by NPs after spin casting of C_{60} and PMMA solution. The right column depicts the NPs coverage after 30 minutes of ultrasonication. The areas depicted before and after the ultrasonication are identical. The NPs are fixed very well, which proves that in this new approach even weakly interacting monomers such as fullerenes (C_{60}) can be used to immobilize NPs on planar surfaces.

3.4 Footprint after moving the NPs

The relocation of NPs and the exposed footprint area indicate the reason of the enhanced NP adhesion in case of the new NP-APTES immobilization sequence.

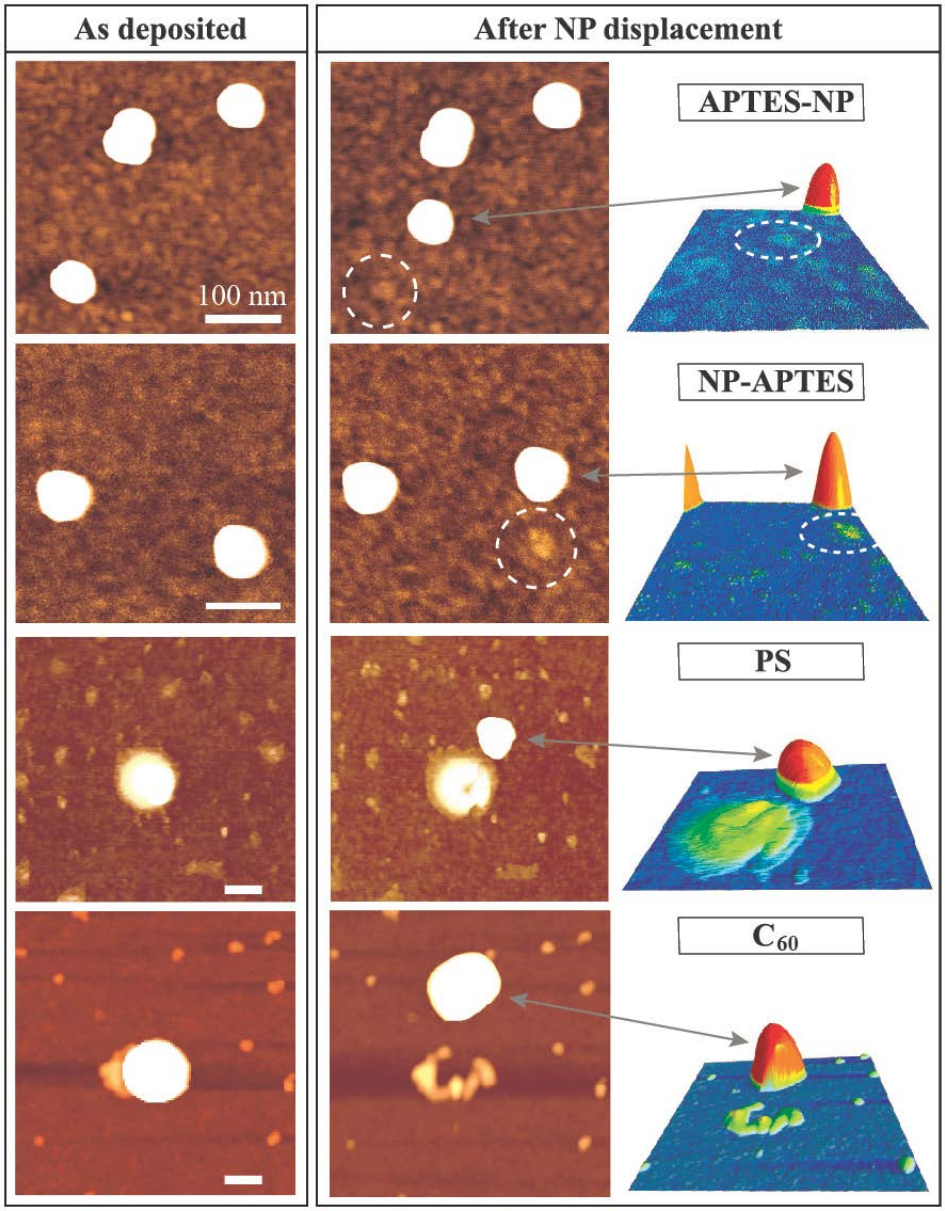

Figure 3.8: AFM images of the footprint areas after moving individual NPs away from their original position. Left row: AFM image prior to particle movement. Middle row: AFM images of the same area after lateral movement of the NP. Right row: AFM 3D images of the area in the vicinity of the NP (after it is moved). In the case with the conventional approach ("APTES-NP") the footprint area is barely different from the surrounding substrate surface. In the case of the new approach the footprint areas are different from the surrounding substrate surface. For NP-APTES the surface below the NP is about 0.3 - 0.4 nm higher than the surrounding substrate surface. The NP sizes were ~25 nm ("APTES-NP" and "NP-APTES") and ~70 nm ("PS" and "C_{60}").

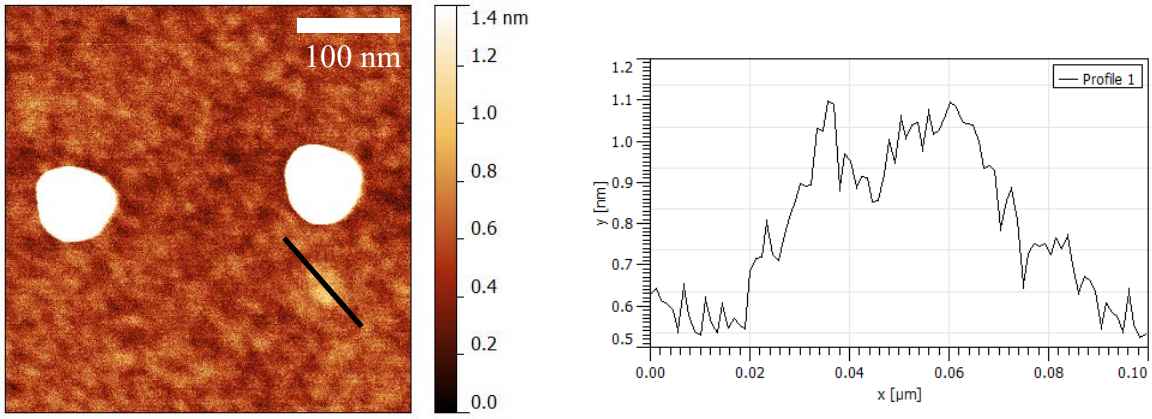

Figure 3.9.: AFM image of the APTES footprint area after moving a Pt NP away from its original point and the corresponding cross section.

Figure 3.8 shows the results of experiments with individual NPs that were moved sideways (with the AFM tip) to reveal the original contact area (footprint) between the NPs and the substrate surface. The location of the NPs prior to their lateral displacement has been determined by triangulation based on the locations of other NPs in their vicinity. One can see that in the case with the NP grafted in the conventional way ("APTES-NP") the footprint area of the NP is barely different from the surrounding surface (as in the case of NPs attached to the bare silica surfaces). In the case of the new method ("NP-APTES") the footprint area can be identified as a spot, which is different from the surrounding surface. The area is about 0.3-0.4 nm higher, as shown in Figure 3.9. In the cases of PS and C_{60} as binding agent the footprint area reveals substantial elevations i.e., some extra deposit. The topologies are similar to rings opened by the lateral movement of the NP. It appears as if the extra deposit was located in the annular gap around the contact area between the NPs and the substrate. The AFM data also show that the surface areas of the samples without attached NPs, which were prepared with the APTES by the conventional as well as by the new method are relatively featureless with a roughness of a few Å. This indicates a (monomolecular) APTES coating without bulk aggregates of APTES. With PS occasional patches/domains about 10Å thick are observed. The shape and amount of these individual PS domains are typical for a submonolayer coverage of PS on silica as is expected from the applied spin cast conditions. It is remarkable that these domains are much thinner than the deposits found in the footprint area. For C_{60} individual C_{60} aggregates (spherical caps) are observed, which are distributed randomly over the substrate surface. This is in agreement with investigations on C_{60} deposited on silica. In comparison to the case with PS the C_{60}

accumulated in the annular gap around the contact between NP and substrate appears more like a chain of spherical caps than a continuous broken ring [119].

The experimental data with the PS and the C_{60} demonstrate that the enhanced NPs immobilization is not caused by larger, polymeric-like structures formed by the binding agents, which create a layer on top of the NPs and the substrate surface, holding the NPs in place. It appears very unlikely that PS forms a large closed network at the low PS coverage applied. For C_{60} under the applied conditions a network-like structure holding the NPs in place is even more unlikely.

3.5 Au NPs immobilization

Furthermore, we applied this new strategy to other NPs system, for example Au NPs. Au NPs were also synthesized using the citrate as capping agent. The average diameter is around 30 nm, according to the TEM image (Figure 3.2 c). From the contrast AFM images (Figure 3.10), the numbers of NPs of the fixed scanning region were nearly the same when compared before and after ultrasonic test. The NPs were still there without any movement. So, we may anticipate that this methodology could be applied to other metallic or semiconducting NPs.

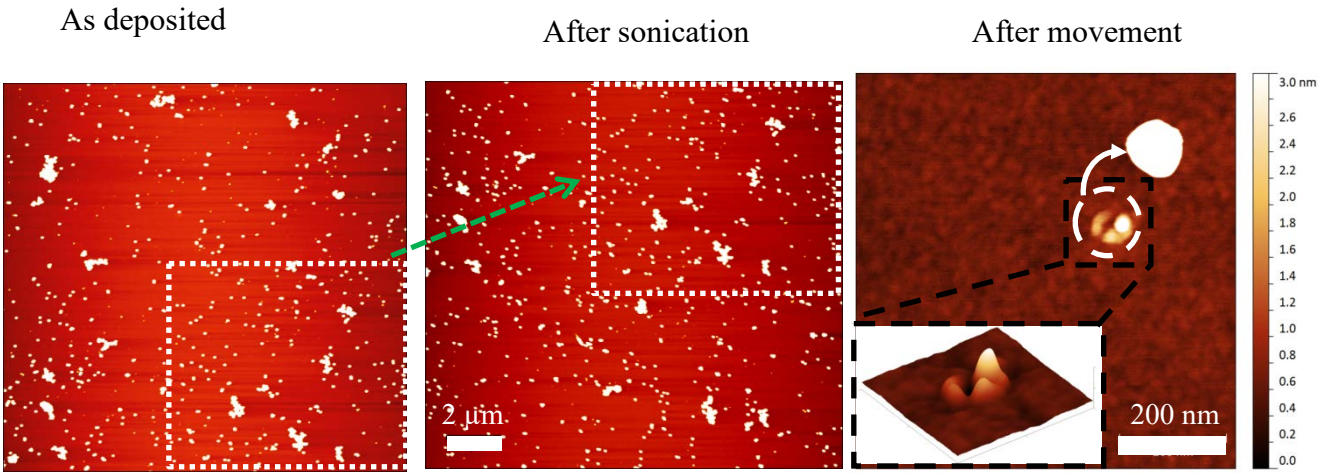

Figure 3.10: Comparison of silica surfaces coated with Au NPs following the new preparation route before (left), after (middle) 30 minutes of ultrasonication and the footprint area after moving individual NP (right). The white boxes mark the same substrate surface area.

3.6 Mechanisms of enhanced immobilization

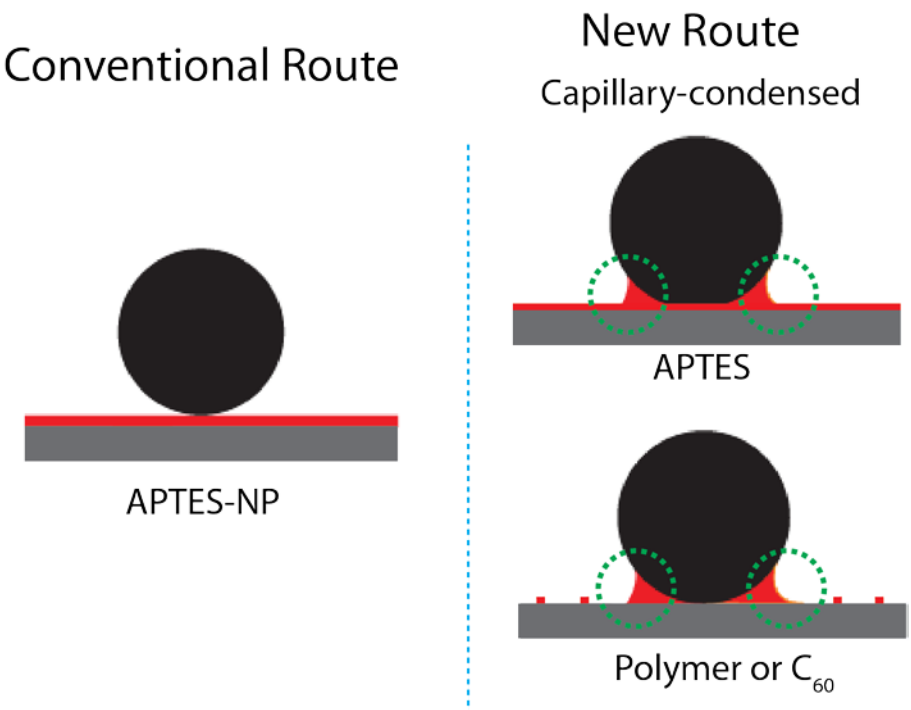

Figure 3.11: Schematic of the NP-substrate contact section in case of the conventional preparation route (left) and in case of the new approach. The AFM images of Figure 3.9 indicate an enrichment of APTES in the footprint section. It is suggested that this caused from a capillary condensation effect.

Figure 3.11 proposes the reason for the increased adhesion based on the new preparation procedure and the additional amount of (presumably) APTES in the range of the NP-substrate contact region. We suppose that the extra amount of APTES originates from capillary condensation [48-53]. The NPs deposited on the substrate are surrounded by an annular gap surrounding the direct NP-substrate contact zone. During the exposure of such a configuration with APTES vapor in the APTES-CVD process, APTES coats the silica surface with a monolayer and in addition enriches in the annular gap through capillary effects.

AFM data proved that with the new preparation protocol the binding agent is accumulated in the annular gap surrounding the contact between the spherical NPs and the planar substrate surface. With the conventional sequence of preparation steps an accumulation of binding agent is not observed. We believe that this accumulation leads to the enhanced

immobilization of the NPs, because it increases the number of links between substrate, binding agent, and NP. In other words, the contact area between NP and substrate is increased. We propose that the accumulation of the binding agent is caused by capillarity. The annular gap surrounding the small contact area between the spherical NP and the planar substrate acts like a narrow pore, where the binding agent gets enriched due to capillary-enhanced adsorption (kind of a "capillary condensation"). It is shown that this "capillary-enhanced grafting" works for different methods of applying the binding agent, such as deposition from the vapor phase and deposition from solution. It works with different types of binding agents, such as those with specific tailor-made cross-linking properties (APTES). But it also works with polymers without specific binding properties (PMMA, PS). It even works with monomers with rather poor binding properties (C_{60}). It is also demonstrated that the new route works for NPs of different sizes and NPs made from other material than platinum (e.g., gold). The new preparation protocol is quite universal. It also works for different shapes of NPs and substrates as long as the attachment of the NP to the substrate surface creates some pore-like structure, which then leads to a capillary-enhanced local accumulation of the binding agent.

3.7 Conclusions

In sum we propose a new and rather generally applicable approach to immobilize NPs attached to substrate surfaces. Instead of applying the conventional scenario of pre-coating (pre-functionalizing) the surface of the substrate and/or of the NPs before contacting the NPs and the surface, we propose that it is more favorable to bring the NPs and the substrate first in contact and then to apply the functionalization respectively binding agent. Thus the narrow annular gap near the NP substrate contact section can induce through capillary (condensation) effects a substantial enrichment of the functionalization agent (which serves as a "glue") in this gap. The extra amount of agent respectively the larger contact area between NP, agent and substrate surface will significantly increase the adhesion interaction between NP and substrate surface.

We support this proposed scenario by showing a much increased NP-substrate adhesion in the case of our new (and at first sight seemingly counterintuitive) preparation sequence of applying the functionalization step (the "glue") ***after*** the NP deposition. In agreement with this scenario we further show that with our new preparation approach the contact area between NPs and substrate indeed contains some extra material (supposedly APTES), which is not there in the cases of the conventional preparation procedure. Last not least we show that this approach also works for Au-NPs and may therefore be applied to fix all types of NPs to surfaces.

4. Enhanced Optical Visualization of Nano-Sized Objects through Thin Film Surface Distortion and Interference Enhanced Optical Imaging

4.1 Introduction

There is an enormous research interest in using nanoparticles because of their remarkable physicochemical properties and potential applications [54-58]. One of the requirements in many of the aforementioned applications is to identify and localize such nanoparticles. So far, there are several approaches used for nanoparticles imagens. Electron microscopy, such as scanning electron microscopy (SEM) and transmission electron microscopy (TEM), can identify the nanoparticles. However, the sample will be destroyed because of high energy electron beam and low vacuum [59-62]. Scanning probe microscopy methods, such as atomic force microscopy (AFM), can also identify and image the nanoparticles, but they are time consuming and scan area is restricted [63-64]. Scanning electrochemical microscopy also can be used to measure the local nanoparticles electrochemical behavior which is limited to liquid/solid, liquid/gas or liquid/liquid interfaces [65-70]. Surface plasmon resonance microscopy is another technique which is not precise to size and shape of the nanomaterials [71-73].

Optical methods, on the other hand, offer the potential for rapid, nondestructive characterization of large areas [74-78]. Over the past two decades, great developments in optical microscopy, especially for super-resolved fluorescence microscopy, have made this technology resolve objects with nanometer precision [78-82]. Recently our group used interference-enhanced optical microscopy to see nanobubbles [8]. Optical interference-enhanced reflection microscopy uses a planar, suitably layered surface to increase the reflected intensity contrast between bare surface areas and regions covered by thin transparent objects [9, 83-87].

In this chapter, we present a new approach to visualize by conventional optical reflection microscopy the location of individual nano-sized objects (e.g., NPs) immersed in thin films. Although the immersed objects are much smaller than the optical resolution limit, their position can be visualized optically through their distortion of the film/air interface. Furthermore, we used silica coated wafers to enhance the contrast between the NPs and substrate. Due to the optical reflected interference, the contrasts for the NPs are enhanced so that they can be localized even without film distortion.

4.2 NPs visualization during thinning of planar liquid films

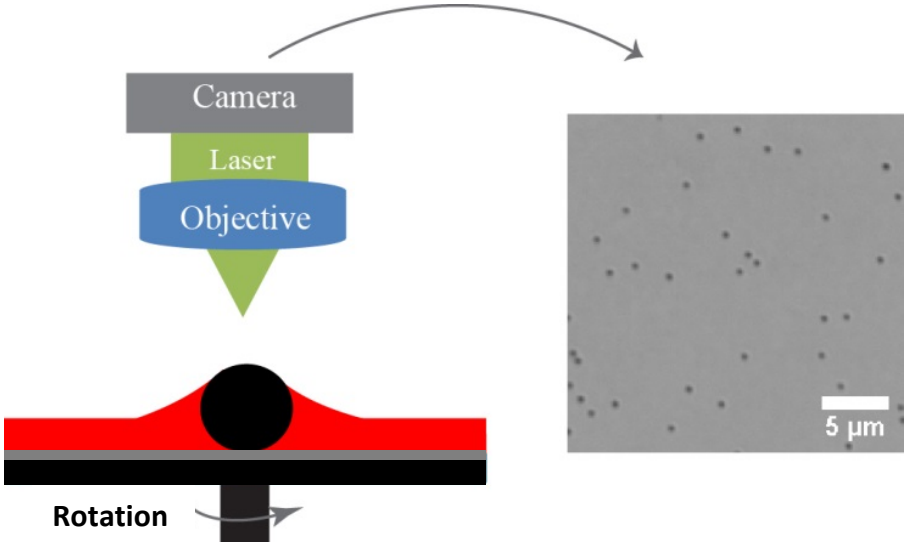

Figure 4.1: Reflection optical interference microscopy imaging coupled with a high speed camera (left) and an optical microscopy image of 50 nm Pt NPs during spin casting process (right).

Figure 4.1 shows the experimental setup to optically determine the location of a nano-sized object and to investigate the interaction between the object and the adjacent film. The sample is imaged from the top in reflection mode with a time resolution of milliseconds. The film/substrate interface is imaged on the camera sensor. A film is formed on top of a planar silicon substrate by spin casting, a well specified method to form thin planar films [8]. Due to the interference of the reflections from the interfaces the camera records a laterally uniform intensity. From this intensity the thickness of the planar liquid film can be calculated (see Figure. 4.2 B). With the interference enhancement by an artificial silica layer on top of the silicon wafer the film thickness can be determined with nm resolution [9].

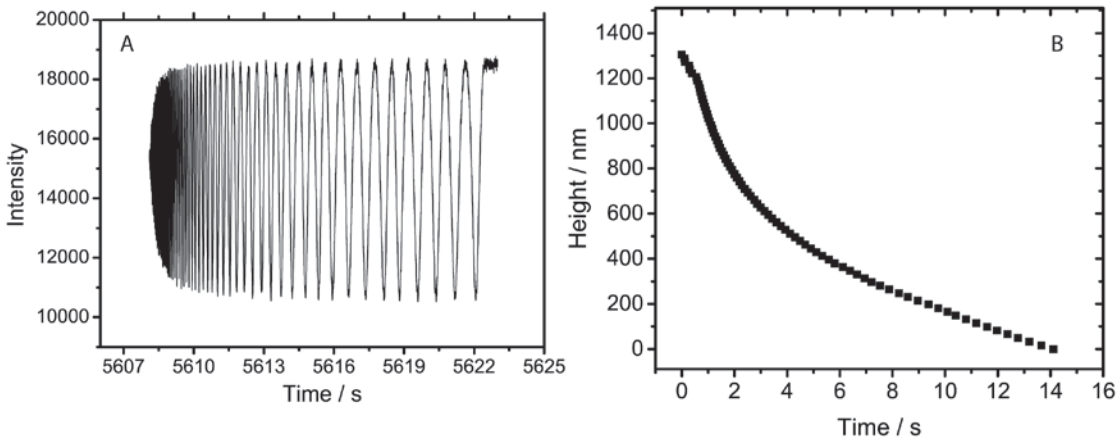

Figure 4.2: (A) Liquid film time-resolved optical intensity and (B) thinning during spin casting of 50 nm Pt NPs solution.

As liquid was deposited on a spinning, planar, wettable substrate, it forms a thinning film through the process of hydrodynamic-evaporative thinning [87-90]. Here we analyze the vertical structural conformation during spin casting of a 50 nm Pt NPs solution. Optical interference enhanced reflection microscopy uses a planar, suitably layered surface to increase the reflected intensity contract between bare surface areas and regions covered by thin transparent objects. The substrate used here is an artificially grown silica layer of 50 nm thickness on silicon wafers, which is the optimal thickness for the laser light with the wavelength of 450 nm, which we used for the optical interference enhanced reflection microscopy. In the following cases of polymer film or melting alkane, the silica layer is not necessary. We use a high speed camera to record this spin casting process. Figure 4.2(A) shows the optical intensity change as the liquid is deposited on the spinning silica coated silicon wafer (2 cm×2cm). Due to the reflected intensity related to the film thickness, we are able to follow the thickness of thinning film. As shown in Figure 4.2(B), the height is gradually decreasing and finally zero after liquid film drying.

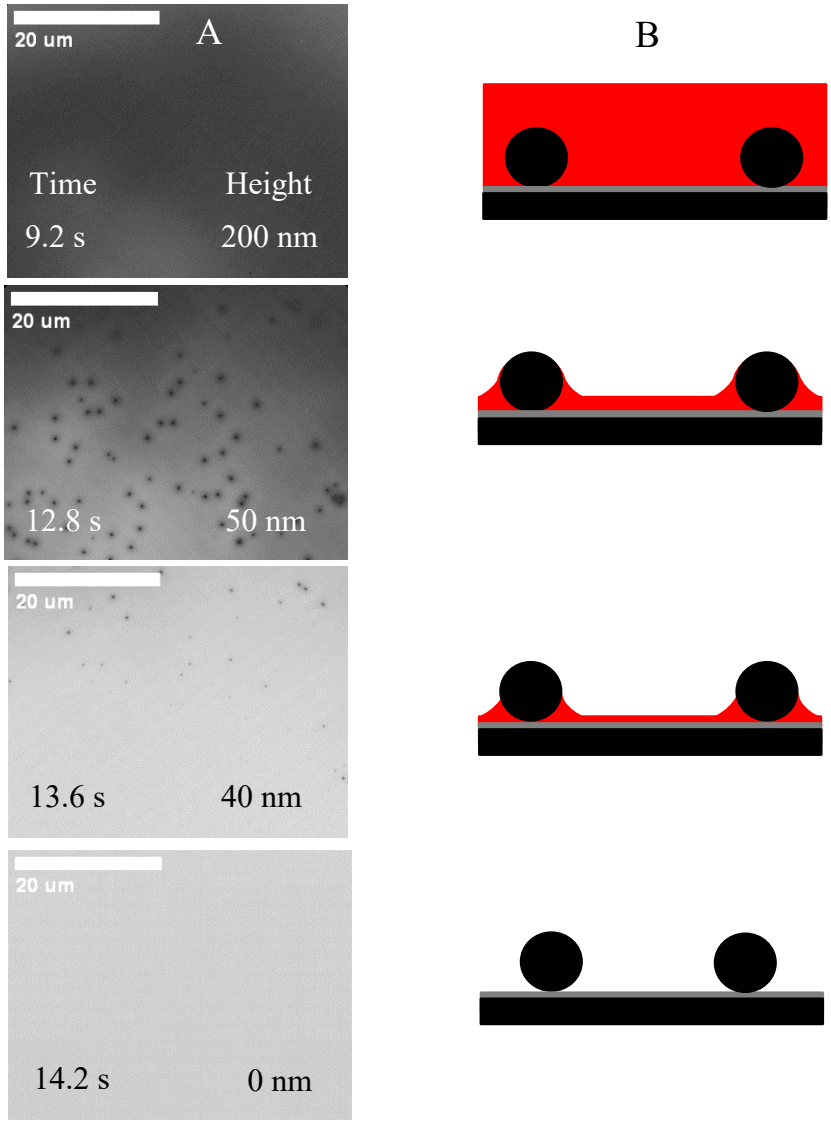

Figure 4.3: Visualization of the 50 nm NPs during the thinning of liquid film on a planar substrate (silicon wafer). A) The sequence of images taken during the evaporative thinning of a water film, which contained Pt NPs with diameters of about 50 nm. B) The cartoons schematically depict the distortion of the liquid/air interface due to capillary interaction, which greatly enhances the "optical footprint" of the NPs and is responsible for the increased visibility of the NP location.

Figure 4.3 presents the visualization and schematic of the NP location during the thinning of thin film on a planar silica surface. The NPs are not visible if the film is thicker than the diameter of the NPs. As soon as the film thickness becomes slightly smaller than the NP diameter, the location of the NPs becomes visible. The visibility contrast again fades away as soon as the film becomes very thin. With a completely dry sample the NPs are virtually not visible. As an example, the visibility/contrast behavior is shown by a sequence of images as shown in Figure 4.3(A), which has been taken during the film thinning of an aqueous

solution of NPs of 50 nm diameter deposited on a rotating substrate during this spin casting process. This process is imaged by reflection optical microscopy from the top with a time resolution of about 1 ms (Figure 4.2). In the range when the film thickness is slightly less than the diameter of the NPs (t=12.8 s, h=40 nm) dark spots appear in the images. These can be attributed to the location of the NPs. The average number of spots per area and their lateral distribution pattern agrees with AFM and SEM measurements of the dry substrate. With the dry samples the location of the NPs again becomes invisible. The cartoons schematically depict the evolution of a liquid film with an immersed spherical NP on the planar substrate during the evaporative film thinning. For films thicker than the diameter of the NP the surface of the liquid film is planar. The optical footprint of the NP is weak. As soon as the film thickness is smaller than the NP diameter, a liquid meniscus i.e., a film surface distortion appears around the NP. This distortion, which involves a much larger area than the cross-section of the NPs, is the reason for the increased visibility of the NP location. When the liquid has evaporated completely this enhanced optical footprint is gone and the location of the NP becomes invisible as in the case of the thick film.

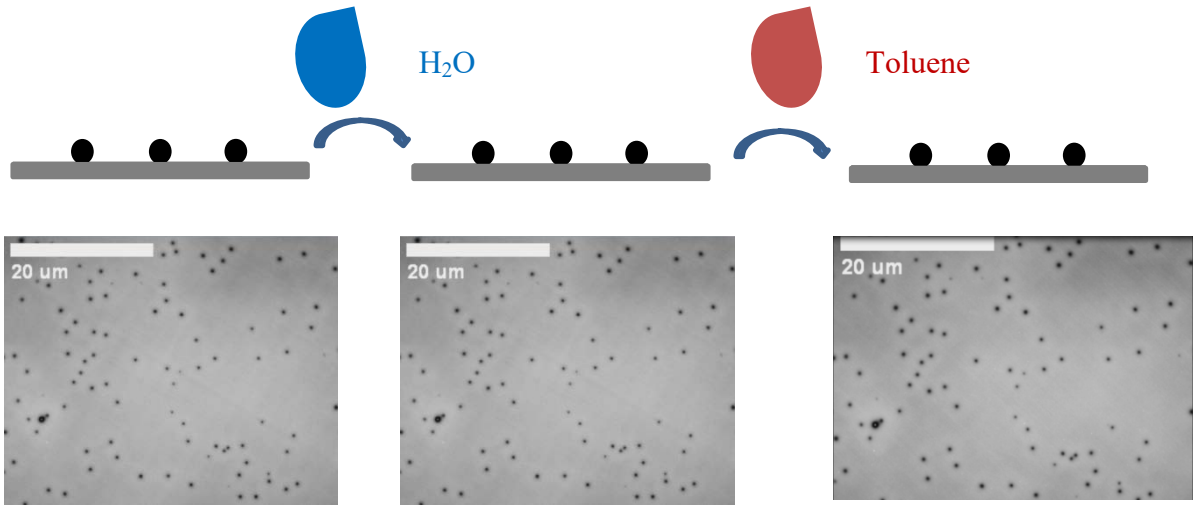

Figure 4.4: Optical microscopy images during repeatedly spin casting of H_2O and toluene onto 50 nm Pt NPs pre-coated substrate.

In addition, we spin cast H_2O and toluene onto the NPs coated substrate. As shown in Figure 4.4, nearly all of them stay at their original location after consecutive spin casting of these two solvents. The stability of NPs coated on the substrate gives us the possibility to spin cast polymer solutions onto such surfaces.

4.3 NPs visualization through embedded in thin solid polymer films

4.3.1 Poly (methyl methacrylate) (PMMA)

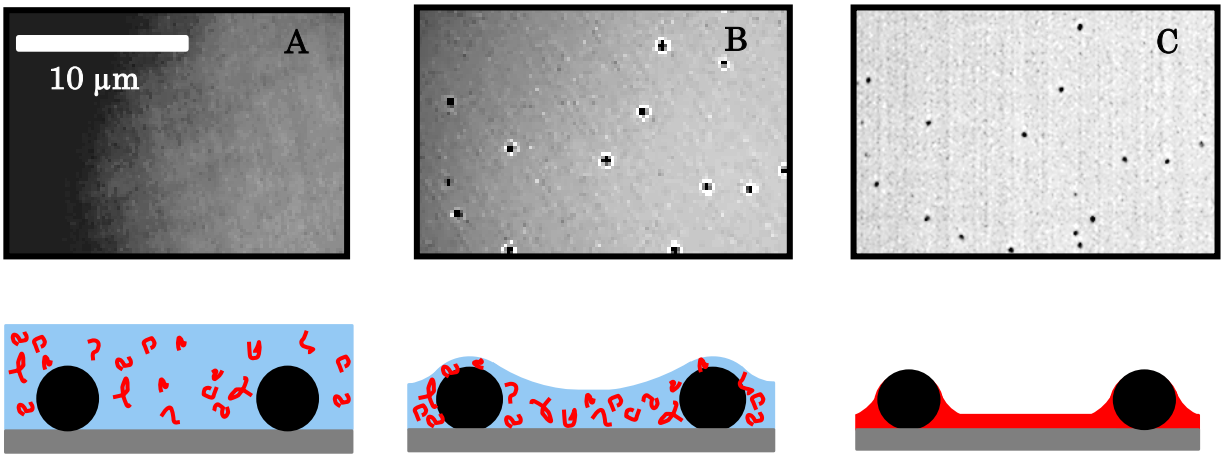

Figure 4.5: Optical microscopy images during spin casting of 5×10^{-3} w/w PMMA in toluene solution onto 140 nm Pt NPs pre-coated substrate.

We present another approach to visualize by conventional optical reflection microscopy the location of individual nano-size objects (e.g., NPs) immersed in thin polymer films. Although the immersed objects are much smaller than the optical resolution limit, their position can be visualized optically through their distortion of the film/air interface with the help of thin polymer film. Imaging is possible when the film thickness is in the range of the size of the objects (see Figure 4.5).

For this method, we prepare the films by consecutive spin casting of Pt NPs from aqueous solution followed by spin casting of PMMA/toluene solution. Real time optical imaging reveals the position of the nanoparticles, their interactions (e.g., lateral movement), the film surface morphology, and the lateral thickness variation of the film. As shown in Figure 4.5 A, the NPs cannot be visualized when the film thickness is higher than the NP diameter. As the thickness of film reaches to the NPs diameter, we can localize the NPs (Figure 4.5 B). After spin casting of a PMMA film, the distortion around the NP is frozen by the solid film, which makes it possible to visualize the NPs all the time (Figure 4.5 C).

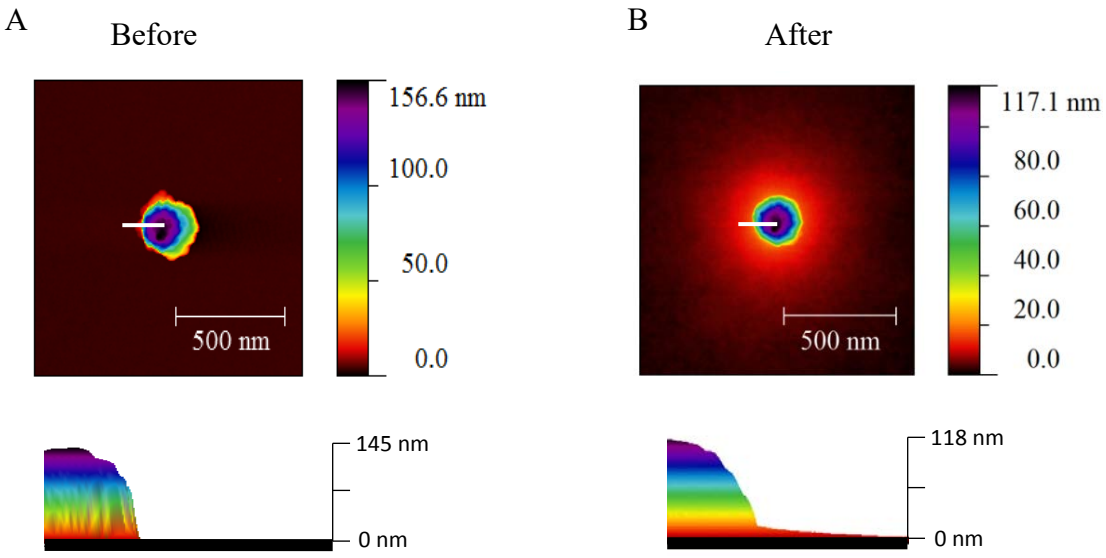

Figure 4.6: The upper row: AFM images before and after spin casting of 5×10^{-3} w/w PMMA solution onto 140 nm NPs pre-coated substrate; the down row: the 3D images of the corresponding AFM images.

The optical imaging of deposited structures is complemented by AFM as shown in Figure 4.6. The height of NPs is around 140 nm initially. After spin casting of PMMA solution on to the NPs pre-coated substrate, there is the distortion around NPs as shown in 3 D images. By spin casting of the PMMA solution, we are able to freeze such a distortion structure around the NPs, which helps to localize the NPs.

4.3.2 Polystyrene (PS)

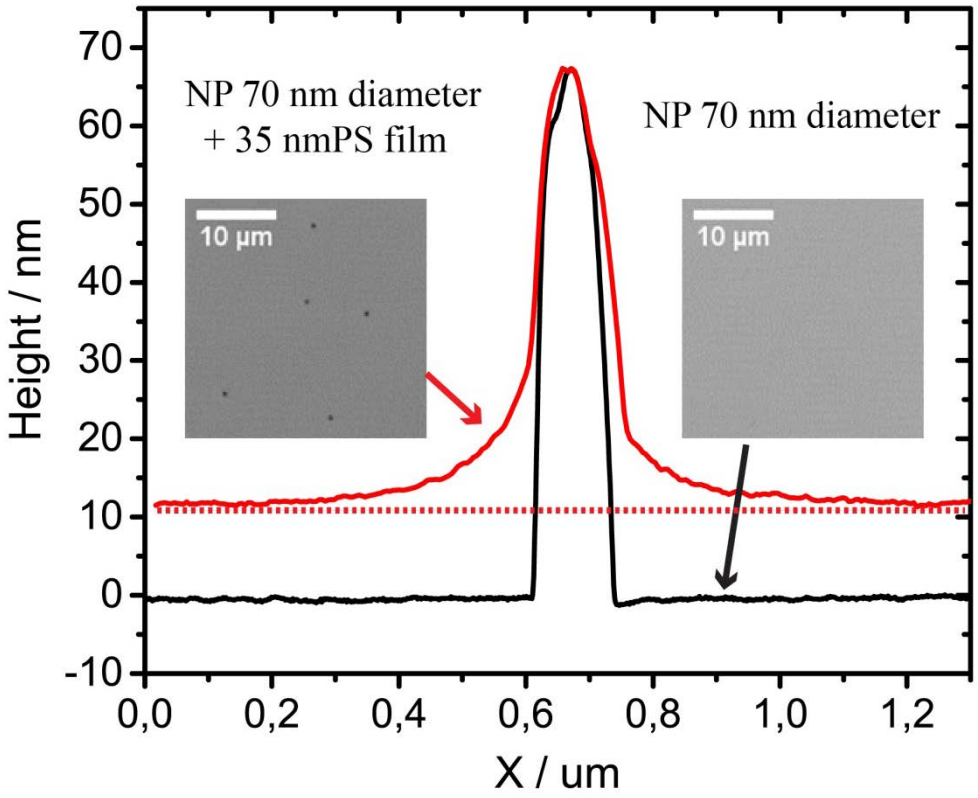

Figure 4.7: Distortion formation after spin casting of PS solution onto 70 nm Pt NPs pre-coated substrate.

Figure 4.7 shows optical imaging of NPs with diameters of about 70 nm deposited on a planar silica surface with or without an additional polystyrene film. The height profiles measurement and the optical image on the left show the case with the NPs deposited on a bare silica surface followed by the deposition of PS-film. The height profiles across the center of the NP (height vs lateral distance) are derived from the AFM data.

In the optical image on the left the locations of the NPs are clearly visible. The cross section image with the NP embedded in the PS-film shows that PS surface forms a circular meniscus adjacent to the NP. This becomes quite obvious from the height profile (red line): The NP with a diameter of about 70 nm “sticks out” of the solid PS-film by about 55 nm. The NP distorts the PS-film. It creates a meniscus with the PS film thickness that reaches laterally several hundred of nanometers away from the NP. Without the PS-film the NPs are not visible in the optical image. This method is universal and work with different kinds of polymers.

4.3.3 Different sizes of NPs

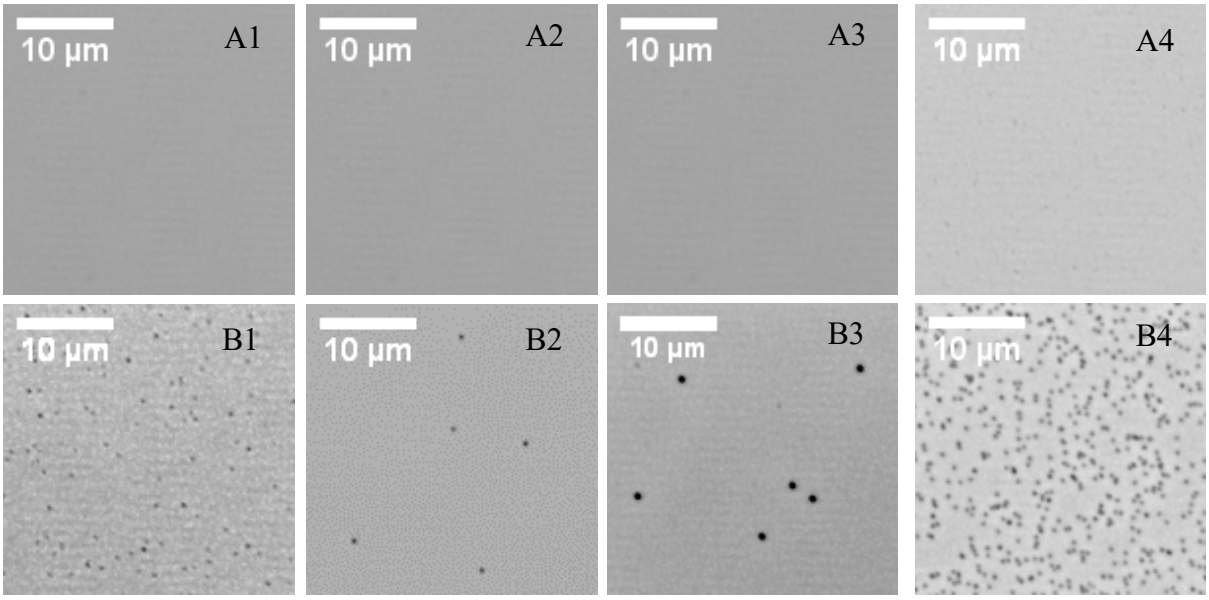

Figure 4.8: Optical microscopy images of before (A1-4) and after (B1-4) spin casting of PMMA solution (film thickness: 10 nm) onto different diameters and kinds of NPs coated substrates (100× objective Pt NPs A1: 25, A2: 70, A3: 100 nm; A4: SiO_2 NPs 50 nm).

Additionally we spin cast the same concentration of PMMA solution to different size and different kinds of NPs pre-coated substrates. Figure 4.8 shows optical images of NPs with different diameters in range from 25 nm to 100 nm deposited on a planar silica surface with or without an additional PMMA film. On the upper row the locations of the NPs are not visible. Because the NP embedded in the PMMA film forms a circular meniscus, the NPs are clearly visible under the optical microscopy lower row. We can also see differences between different sizes of the NPs. We also tried another kind of nanoparticle e.g. SiO_2 with 50 nm in diameter. It results in similar image differences between before and after embedding in 10 nm thin polymer film.

4.3.4 Different thicknesses of polymer dependence on NPs visualization

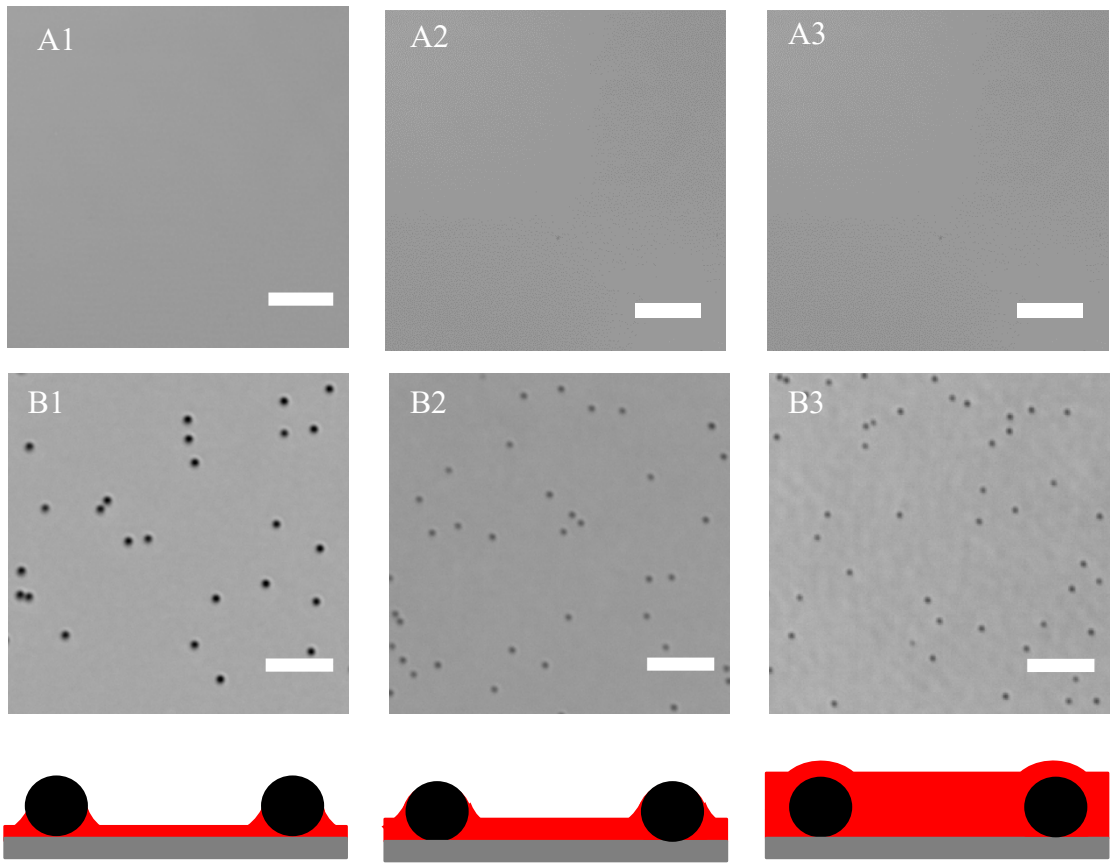

Figure 4.9: Optical images of before (A1-A3) and after (B1-B3) coated with different thickness of PMMA film (B1: 10 nm; B2: 35 nm; B3: 80 nm) onto 70 nm Pt NPs pre-coated substrate. Scale bar: 5 µm.

Furthermore, we tried to compare different thicknesses of PMMA film on the 70 nm Pt NPs pre-coated substrate. Figure 4.9 shows optical microscopy images of 70 nm Pt NPs before and after embedding in different heights of PMMA thin films with 10 nm, 35 nm, and 80 nm. The height profiles across the center of the NP (height vs lateral distance) are measured by AFM, as shown in the following Figure 4.10. The 70 nm Pt NPs without polymer film are not visible. However, they can be seen after they are coated with different thicknesses of PMMA thin films. The sample with the thickness of 10 nm had the best contrast when compared with the thinner and thicker ones. To understand this, we moved to the following AFM data.

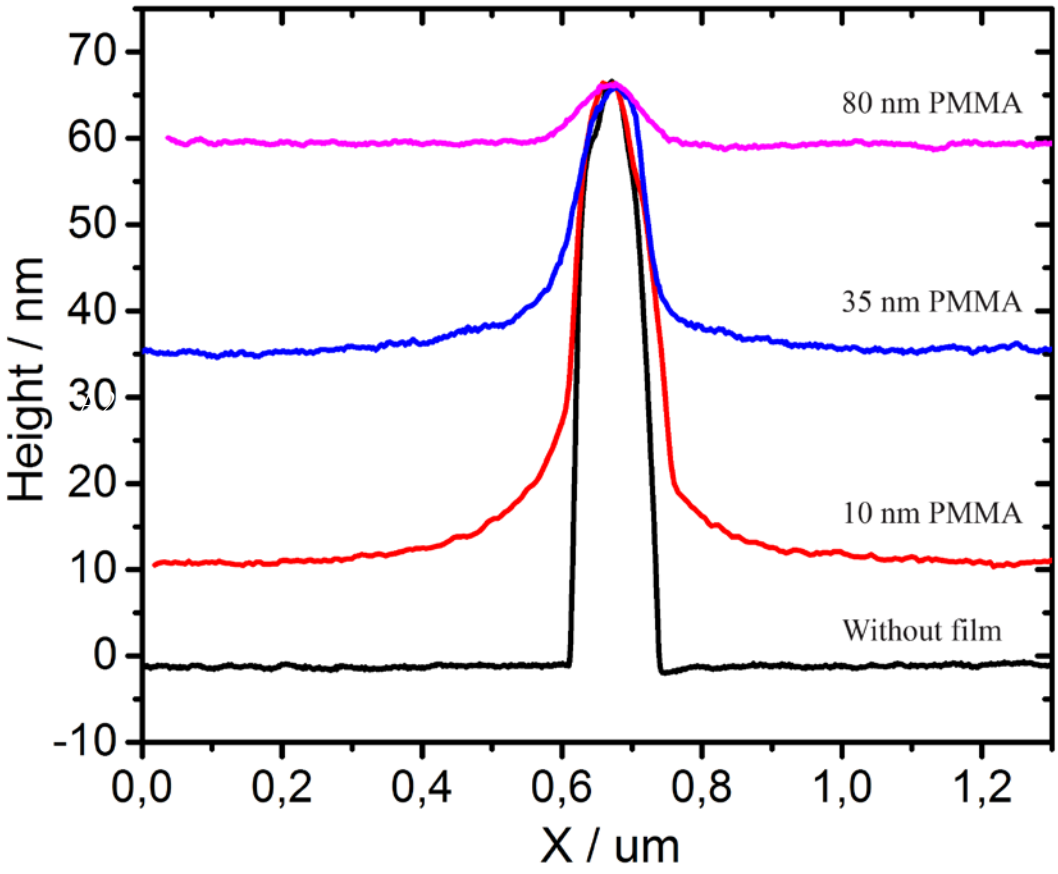

Figure 4.10: The height profiles from AFM measurements before and after coated with different thicknesses of PMMA film onto 70 nm Pt NPs coated substrate.

Figure 4.10 presents the height profiles AFM images of 70 nm Pt NPs embedded in different height of PMMA thin film in range from 10 nm, 35 nm, and 80 nm. The height profiles were across the center of the NPs. For 10 nm PMMA, its distortion was the largest among these three thicknesses film. A larger lateral distortion causes the larger enhance imaging.

4.4 Switching on and off NPs visualization through melting alkanes

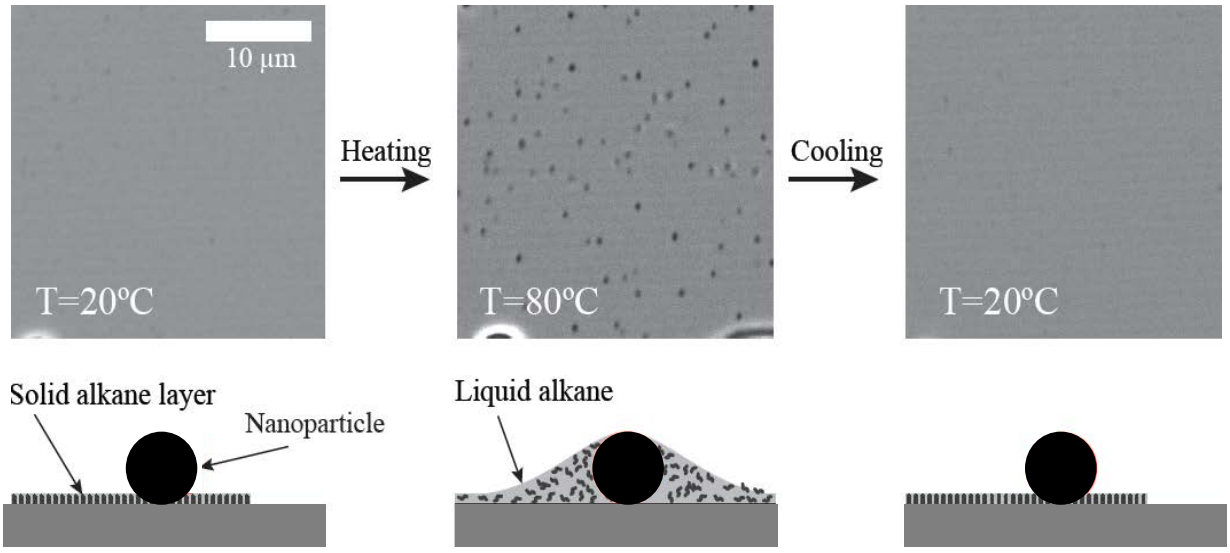

Figure 4.11: Optical microscopy images (top row), schematics (down row) of ~25 nm Pt NPs deposited on a planar silica surface together with a thin layer of long chain n-alkane ($C_{30}H_{62}$). At the temperatures below its melting point (*Tm* = 67 ºC) the alkane forms areas with planar films consisting of mono-and/or multilayers with layers of uniform thickness (= the length of the alkane molecules). The NPs do not deform these solid alkane films. At temperatures above its melting point, the molten alkane forms a liquid film. This film completely wets the substrate surface and forms a liquid meniscus around the NPs. This can be inferred from the strongly enhanced optical visibility of the location of the NPs in this case.

Figure 4.11 demonstrates how the imaging contrast can be switched on and off by changing the distortion of the surface adjacent to the NP. In Figure 4.11 this has been achieved by switching between the solid and the liquid state of a thin film of a long chain n-alkane ($C_{30}H_{62}$) that is deposited on the substrate surface in addition to the NPs. Below their melting temperature (T_m = 67 °C) the alkanes form areas with solid planar mono- and multilayers of uniform thickness (each layer is as thick as the length of one molecule) [91]. In the solid state the planar alkane film morphology is not affected by the NPs. This is verified by the AFM imaging and corresponding height profile. Above their melting point the alkanes form a closed liquid film on the substrate. The NPs are embedded in this film and they distort the film surface in their vicinity just as in the case of the thinning liquid film (Figure 4.3) or in the case of the solid PS-film (Figure 4.8). This meniscus formation in the case of the co-deposited alkane film can be inferred from the strongly enhanced optical visualization of the NP locations.

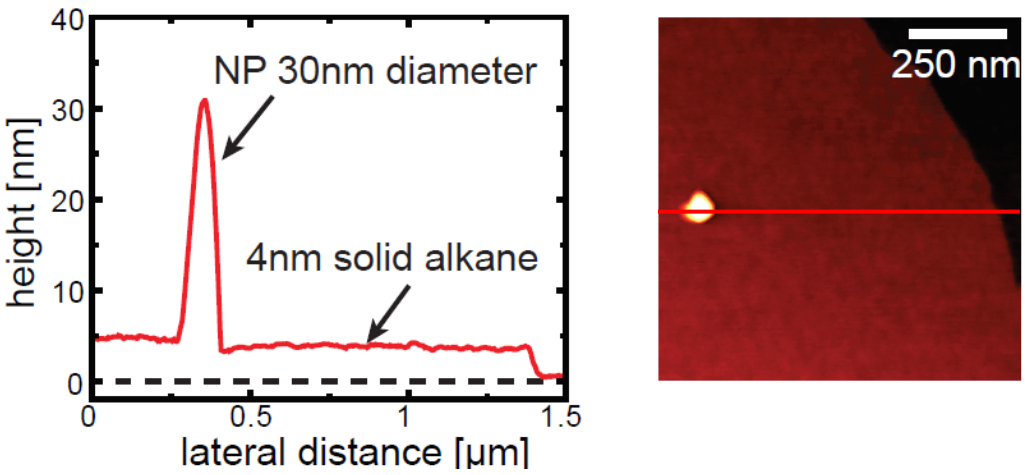

Figure 4.12: AFM image and cross section after cooling of alkane ($C_{30}H_{62}$).

Figure 4.12 presents AFM imaging of NPs deposited on a planar silica surface together with a after cooling the alkane ($C_{30}H_{62}$) melting liquid. Due to temperatures below its melting point the alkane forms areas with planar films consisting of mono- and/or multilayers with layers of uniform thickness (= the length of the alkane molecules). As shown in Figure 4.12(A) the NPs just embedded in the solid alkane films and do not distort it any more. The thickness of the film is about 4 nm which is the monolayer of alkane ($C_{30}H_{62}$) from Figure 4.12(B).

4.5 NPs visualization through optical interference-enhanced imaging method

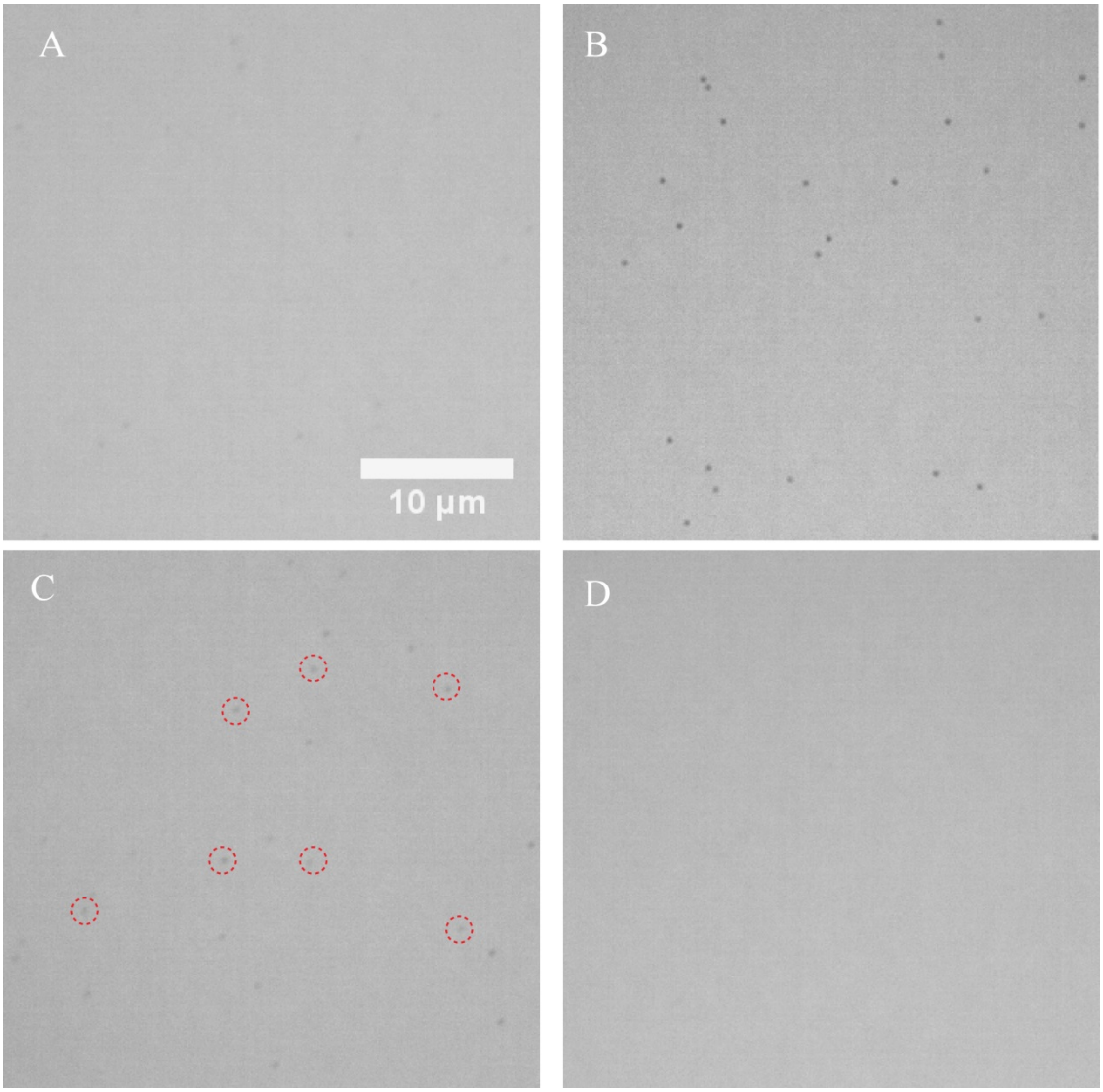

Figure 4.13: Optical images of 70 nm Pt NPs deposited on different thicknesses SiO_2 layers coated silicon substrate. A: without SiO_2 layer; B: 50 nm SiO_2 layer; C: 100 nm SiO_2 layer; D: 300 nm SiO_2 layer. The laser wavelength is 450 nm.

Figure 4.13 shows the optical microscopy images of 70 nm Pt NPs on different SiO_2 layers coated silicon substrate. The wavelength of laser used here is 450 nm. We can see that for 50 nm layer of SiO_2 the imaging had the best contrast. For 100 nm layer of SiO_2, we also can localize the NPs as shown in Figure 4.13 C (the red dashed circles), but with a reduced contrast. We can not see them with 300 nm SiO_2 layer coated substrates or without layers. It proves that we can directly localize the NPs by using the different thickness SiO_2 layer coated substrate. In this case of NPs imaging, we do not need the extra film distortion

formed around the NPs. It is sufficient to use SiO_2 coated silicon wafers to enhance the contrast to image the localization of nano-sized objects.

4.6 Interferences at SiO_2/Si interfaces

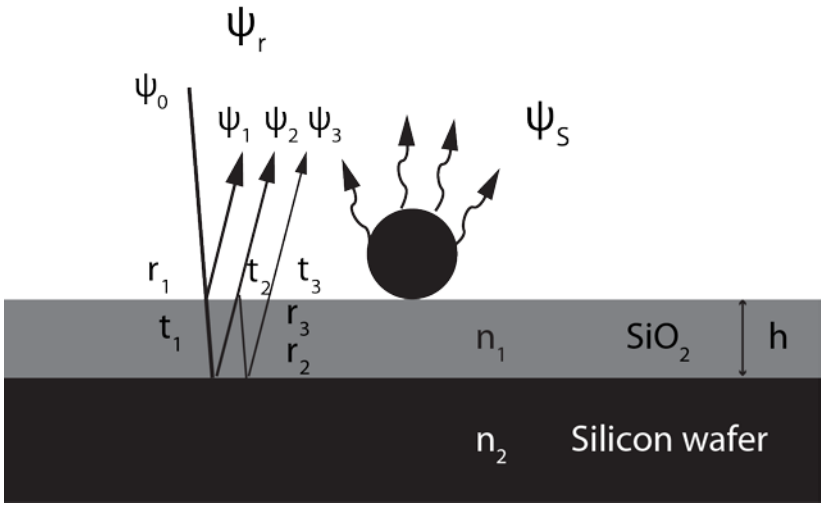

Figure 4.14: Schematic of the reflection from the film deposited on substrate.

In classical theory, the interaction of a particle with light can be understood via induced dipoles on a non-absorbing particle [76]. The strength of the induced dipole is proportional to polarizability of the small particle

$$\alpha = 4\pi\varepsilon_0 r^3 \frac{\varepsilon_p - \varepsilon_m}{\varepsilon_p + 2\varepsilon_m} \tag{4.1}$$

where r is the particle radius, $\varepsilon_p$and ε_m are the particle and surrounding medium permittivity, respectively [116]. Detection techniques which depend on the scattering intensity do not work when the particles are small (eg. nanoscale) due to the detector signal given as $I \propto |\psi_s|^2 \sim |\alpha|^2 \propto r^6$.

In our system, we used interference-enhanced optical reflection microscopy to detect the NPs through silica coated wafers to enhance the contrast. Figure 4.14 shows a schematic of the reflections from the silica film coated wafer. Due to the different refractive indices of silica (n_1 = 1.4598) and silicon (n_2 = 3.88), light reflecting interfaces will be created. The reflections from the various interfaces are,

$$\psi_1 = r_1 \psi_0 e^{i\pi} \tag{4.2}$$

$$\psi_2 = t_1 r_2 t_3 \psi_0 e^{i\varphi} \tag{4.3}$$

$$\psi_3 = t_1 r_2 r_3 r_2 t_3 \psi_0 e^{2i\varphi} \tag{4.4}$$

…

where ψ_i is the complex amplitude, r_i and t_i are reflectance and transmittance, which are given by the Fresnel relations [9, 117].

For a film with thickness h and refractive index n, illuminated by monochromatic light of wavelength λ, the phase shift φ for normal incidence is

$$\varphi = \frac{4\pi \cdot 2nh}{\lambda} + \pi \tag{4.5}$$

Assuming coherence, the overall reflected wave resulting from all reflections is

$$\psi_r = \sum \psi_i = r_1 \psi_0 e^{i\pi} + t_1 r_2 t_3 \psi_0 e^{2i\varphi} \frac{1}{1 - r_2 r_3 e^{i\varphi}} \tag{4.6}$$

Therefore the reflected intensity I_r is

$$I_r = {\psi_r}^2 = \left| \frac{t_1 r_2 t_3}{e^{-i\varphi} - r_2 r_3} - r_1 \right|^2 |\psi_0|^2 \tag{4.6}$$

For the laser wavelength 450 nm, the relative intensity $I_r/|\psi_0|^2$ as function of film thickness h is shown in Figure 4.15 A. Furthermore, if we want to get the best contrast for small changes of objects, it´s noted that we should maximize dI_r/dh. As a result, Figure 4.15 presents such contrast of the reflected intensity as a function of the wavelength for an oxide layer of 50 nm. We can see that it has the best contrast for the light at 450 nm wavelength. For our system, the 70 nm Pt NPs is detected clearly for an oxide layer of 50 nm, which can be explained by this curve. However, the NPs cannot be imaged for the oxide layer of 300 nm or without oxide layer, because the contrast is not big enough for NP imaging.

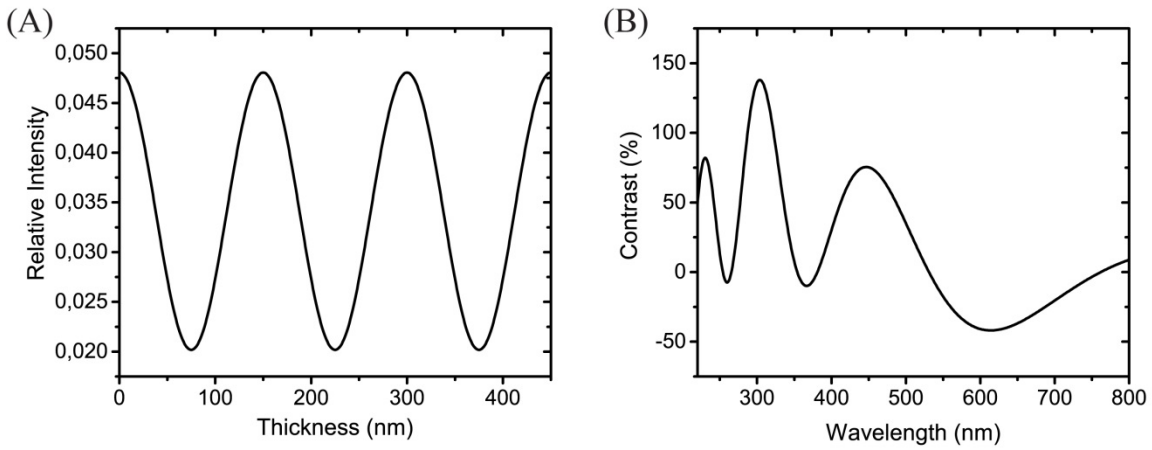

Figure 4.15: (A) Relative reflected intensity $I_r/|\psi_0|^2$ as function of silica film thickness h. (B) Contrast dI_r/dh as function of incidence wavelength for a 50 nm silica coated silicon wafer.

4.7 Conclusion

We present a method to track the location of NPs within the film and study their interactions with the film based on conventional optical microscopy imaging. It is a rather simple, fast, non-destructive technique. We show that the imaging contrast can be enhanced vastly through the distortion of the surface of a film on the substrate deposited together with the NPs. We present and analyze three prototypical cases including a transient, a permanent, and a reversible visibility enhancement. Aside from the benefit of a much improved imaging of the location of the NPs the approach also reveals valuable information on the interaction between the NPs and the co-deposited thin film (e.g., its height evolution in the vicinity of the NPs). In another case, we used silica coated wafers to enhance the contrast between the NPs and substrate. Due to the optical reflected interference, the contrast for the NPs is greatly enhanced which allows this localization even without distortion/meniscus of a liquid or solid film.

5. Individual Bubble Formation from Single Localized Platinum Nanoparticle Active Sites

5.1 Introduction

Nucleation behaviors have always been of great research interest, because it is ubiquitous in nature and of great importance in numerous industrial processes [92-102]. The formation of an individual pre-critical nucleus and its growth into a stable aggregate is fast and elusive. Typically it occurs on very small scales (nanometers) and is of random nature (thermodynamics of small systems). Experimental data on individual, controlled nucleation processes are virtually nonexistent. In particular new experimental approaches are necessary to gain new insights into the process. Active sites provide a unique opportunity to locally and reproducibly investigate the relation between the physic-chemical properties of the active site and the nucleation behavior. To this end active sites have to be identified (localized), their nucleation relevant properties have to be known (modified), and the site-specific nucleation behavior has to be quantified.

In this chapter, single Pt NP immobilized on silicon wafer surfaces shall act as localized active nucleation site. Pt NPs are known for their ability to catalyze the decomposition of hydrogen peroxide (H_2O_2), to induce the formation of oxygen molecules. Here we localize the Pt NP under optical microscopy and confirm it by AFM measurement. Real-time measurement and characterization of individual O_2 bubble formation were investigated.

5.2 Experimental set-up

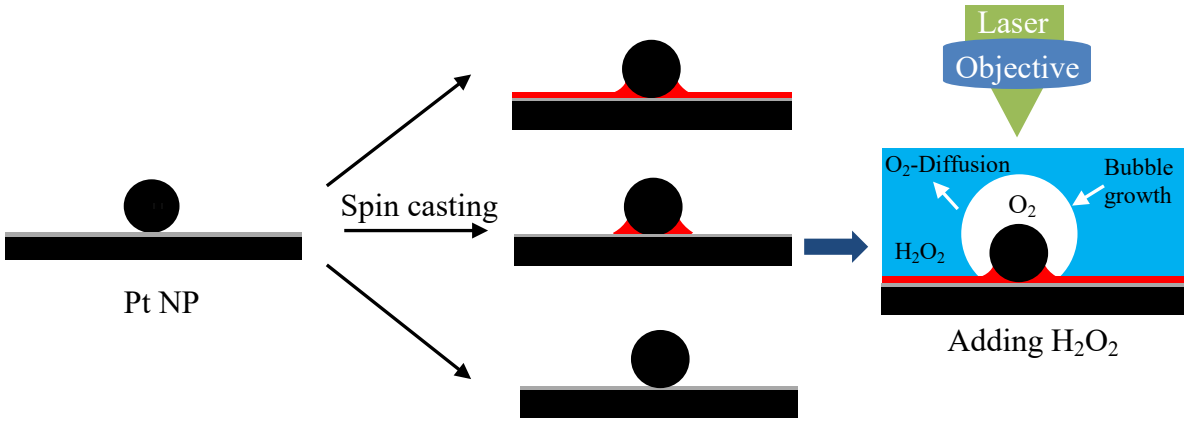

Figure 5.1: Schematic illustration of preparation of different kinds of single Pt NP active site with different interfacial properties and observation of individual bubble formation with optical microscopy.

The Pt NPs with defined diameters, and with the catalytic ability for the decomposition of H_2O_2, were deposited on a planar silicon substrate. To observe a single bubble formation on an individual nano-active site, we used high resolution interference-enhanced optical microscopy to localize the nanoparticle (silicon wafer with 50 nm silica layer) under the laser with the wavelength of 450 nm. In a typical experiment, the NPs were deposited on the silicon substrate. H_2O_2 solution was dropped onto the samples to create a liquid film above the substrate. We observe at the center of the sample where the liquid-air and the solid-liquid interfaces were nearly parallel. The process of bubble formation was recorded on-line under optical microscopy integrated with a high speed camera. We can change the concentration of H_2O_2, the size of Pt NPs, the substrate properties and the thickness of polymer films.

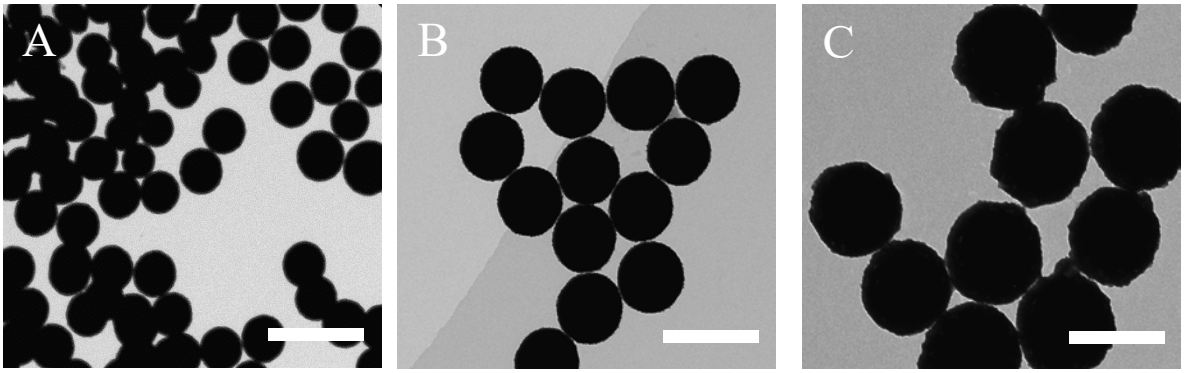

Figure 5.2: TEM images of different diameters of Pt NPs used in this chapter: A) 95 nm; B) 140 nm, C) 200 nm. Scale bar: 200 nm.

The Pt NPs were prepared according to a multistep seed-mediated growth method developed by Nadja C. Bigall et al [103]. Details are shown in THE appendix. We form a successive generation of spherical particles with different sizes by adjusting both the seed particle concentration and the amount of Pt precursor into the solution. Figure 5.2 shows TEM images of differently sized Pt NPs with spherical geometry and low polydispersity.

5.3 Individual bubble formation from single Pt nano-active site

First we spin cast the 200 nm Pt NPs solution and then the PMMA solution (resulting film thickness: 50 nm). Then the substrate was covered with 35 % H_2O_2 to produce the O_2 bubble recorded by the optical microscopy. The Pt NP coverage was very low by spin casting of the very low concentration of Pt NPs solution. The distance between two NPs is at least 200 µm as can be seen by optical microscopy imaging.

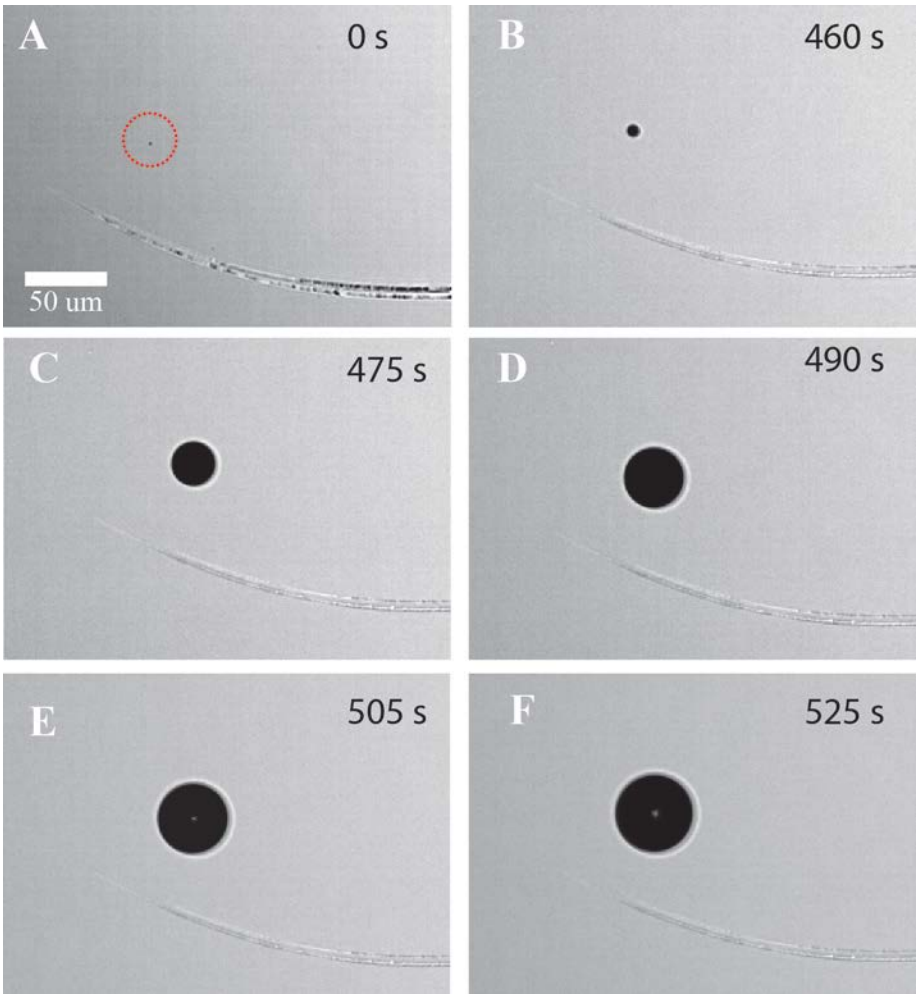

Figure 5.3 Optical microscopy sequential images of single Pt NP (A: without H_2O_2) and time evolution of bubble formation (B-F) from a 200 nm Pt NP embedded in 50 nm PMMA thin film on silicon substrate within 35% H_2O_2.

The overall dynamical behavior of oxygen bubble can be seen from the series of snapshots in Figure 5.3. It shows a typical individual bubble formation from a single Pt NP (200 nm) which was covered in 50 nm PMMA thin film. Due to the film distortion, we can localize the NP with the optical microscopy, as shown in Figure 5.3 A. The scratch here is used to mark the point of NP during immersing in H_2O_2. After an incubation time of 460 s, the bubble formed and grew continually after the incubation time. The volume of bubble increased proportionally to the time.

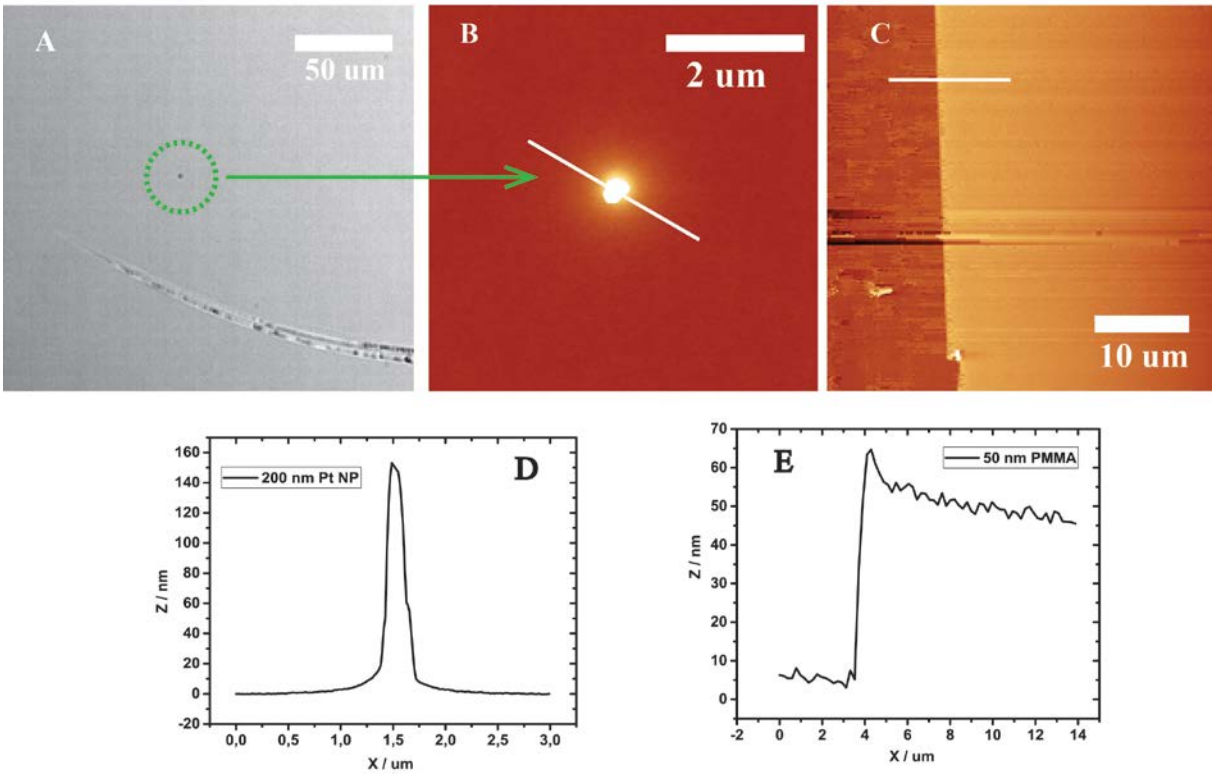

Figure 5.4: OM images (A) and AFM (B) in-site images for the 200 nm Pt NP embedded in the PMMA film. C is the AFM image of a line scratch edgy. D and E are the corresponding section analysis of the NP and film thickness.

To reveal the structure of the Pt active site, we find the Pt NP reversibly with the help of a marker (scratch) and measure it by AFM. The results are shown in Figure 5.4. The Pt NP height above the film is around 150 nm according to the date from Figure 5.4 B, D. By making a scratch, we measure the thickness of PMMA film. The thickness of the film was about 50 nm formed by spin casting a solution of 5×10^{-3} w/w PMMA in toluene (1×10^{3} rpm), as shown in Figure 5.4 C, E.

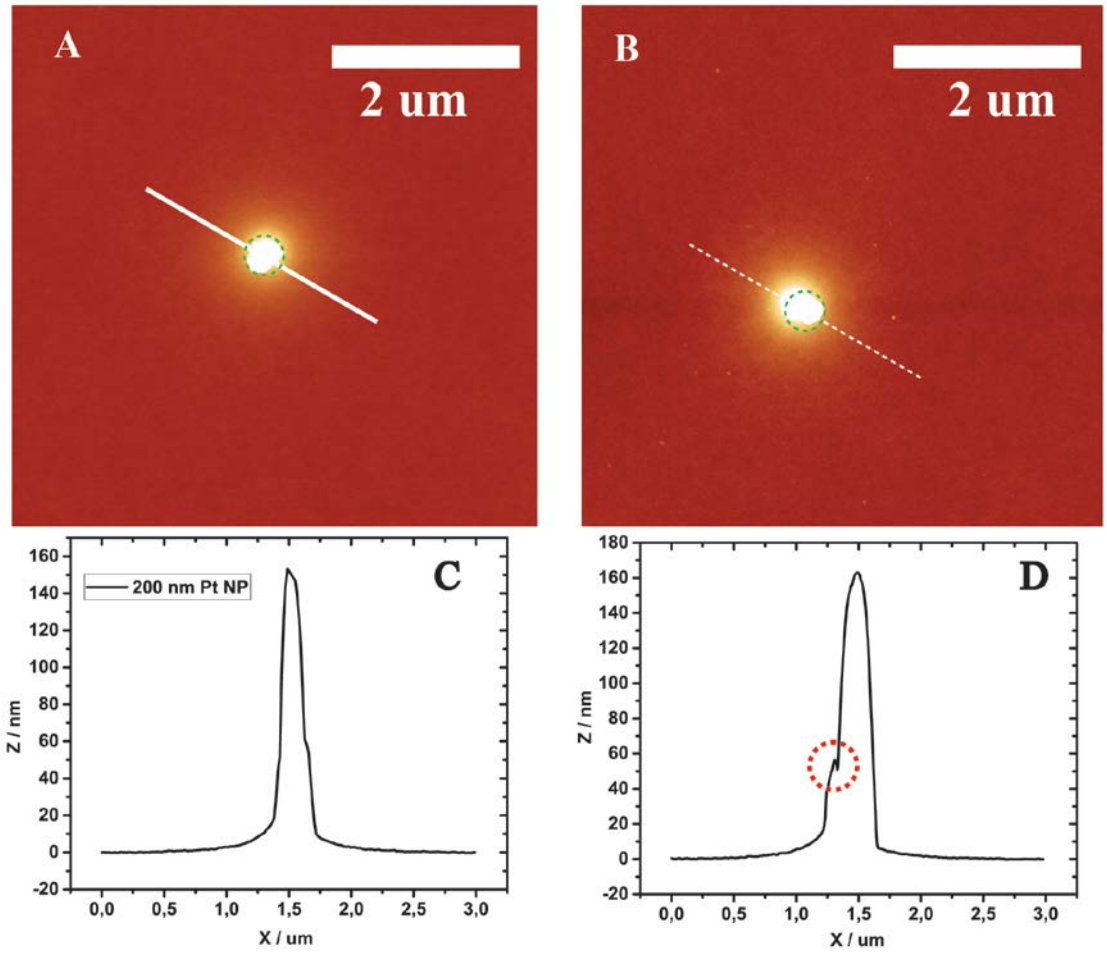

Figure 5.5: AFM images of the 200 nm Pt NP embedded in 50 nm PMMA thin film before and after bubble formation within 35% solution of H_2O_2 in 1 hour. The section analysis is performed across the NP.

We also compare the structure before and after bubble formation for the Pt NP active site by AFM, as shown in Figure 5.5. From the section analysis, we can see that the NP moved aside and lifted up a little bit. The height is lifted up about10 nm by comparing the height of the NP before and after bubble formation. It also moved aside when it is exposed to the H_2O_2 solution.

5.4 Kinetics of bubble formation

5.4.1 Effect of H_2O_2 Concentration on bubble formation

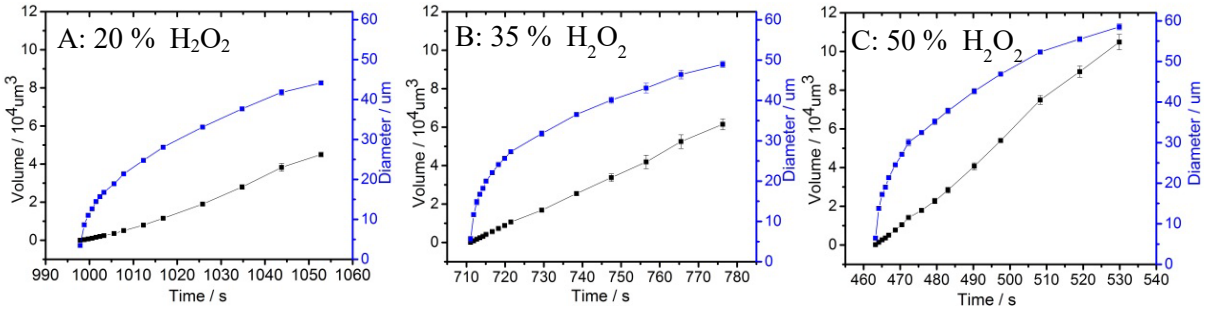

Figure 5.6: Individual bubble growth from a 140 nm Pt NP. Bubble volume (black curve) and diameter (blue curve) as a function of time for different concentration of H_2O_2: A) 20 %; B) 35 %; C) 50 %.

Here we consider the parameter of H_2O_2 concentration and study its effect on the bubble formation. In this system, we just change the parameter of H_2O_2 concentration, with other parameters being the same (NP size: 140 nm, film thickness: 50 nm; NP coverage: ~1.2 /250 μm x 250 μm). The data is shown in Figure 5.6, where black and blue curves show bubble volume and diameter as a function of time for 20 %, 35 %, and 50 % concentration of H_2O_2. Here the bubble diameter was extracted from the optical microscopy images by ImageJ software. For the bubble volume calculation, we assumed that it is aspheric as is described in ref. [28]. From Figure 5.6, it can be seen that the bubble volume increases linearly with time *t*. Moreover, the slope increases with increasing the concentration of H_2O_2. By linearly fitting the data, they are 450, 993, and 1403 $\mu m^3/s$, with corresponding standard error 10.6, 8.2, and 22.5 for the different concentrations of 20 %, 35% and 50%. The linear relationship between volume and t is consistent with the observed behavior for the diameter. Since volume linearly increases with t and bubble is nearly spherical, diameter should scale as $t^{1/3}$.

5.4.2 Size of NP on bubble formation

We now consider the effect of Pt NPs size on the bubble formation. Figure 5.7 shows the AFM images of three different sizes of Pt NPs, 95 nm (a), 140 nm (b), and 200nm (c), embedded in a PMMA film with thickness of 50 nm. Considering the height of PMMA film, the actual height of Pt NPs decreased to 47 nm (a), 93 nm (b), and 150nm (c), consistent with the size measured from TEM.

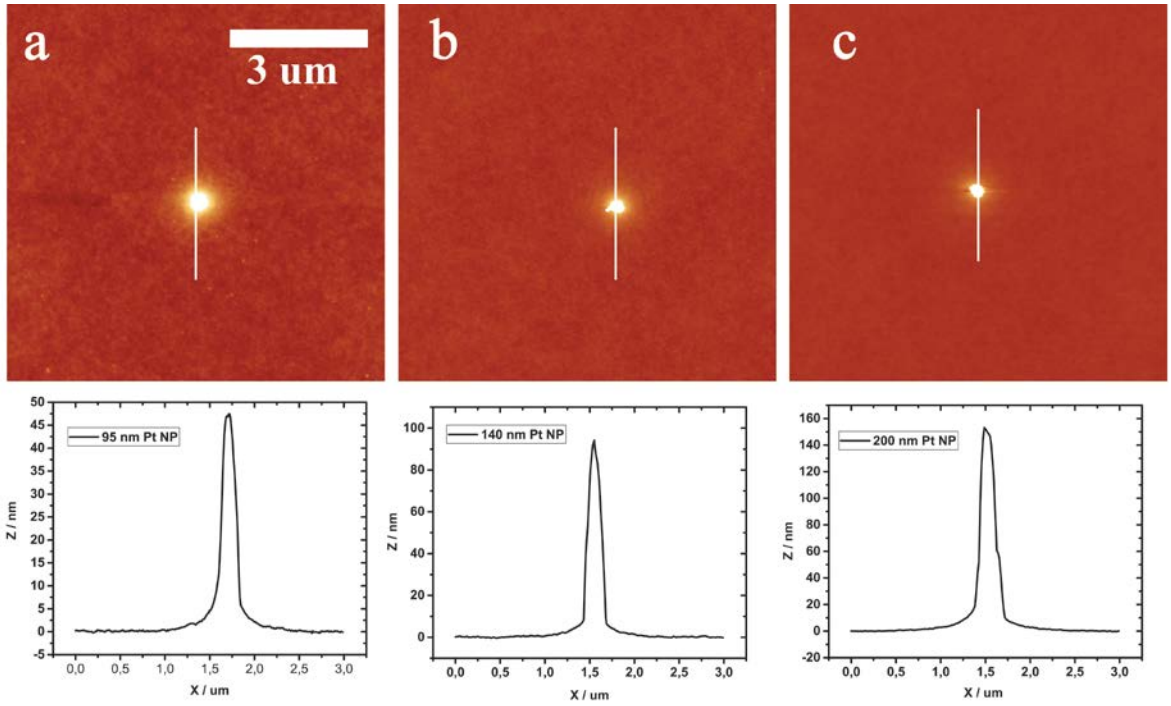

Figure 5.7: AFM images of the Pt NP with different diameters embedded in 50 nm PMMA thin film: A) 95 nm; B) 140 nm; C) 200 nm.

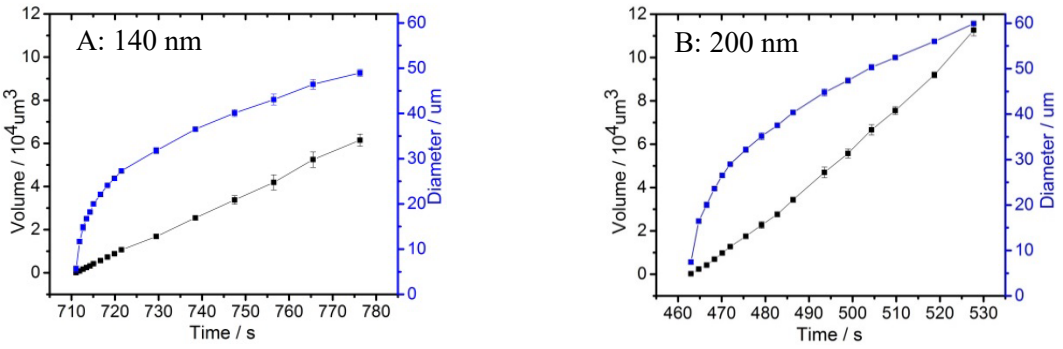

Figure 5.8: Individual bubble growth from single Pt NPs. Bubble volume as a function of time for different diameters of Pt NPs: A) 140 nm; B) 200 nm. The concentration of H_2O_2 is 35 %. The Pt NPs coverage is about ~2 $\times 10^{-5}/\mu m^2$.

For the bubble formation, we found that it would not produce bubble for the size of 95 nm even after long incubation time (above 1 hour). For the size of 140 nm and 200 nm, the bubble would be formed at the time of 712 s and 463 s after they contacted with 35 % H_2O_2. The data of their bubble volume and diameter as function of time are shown in Figure 5.8. It can be seen that the bubble

volume increases linearly with time *t* with the slope of 993 and 1529 $\mu m^3/s$ having standard error 8.2 and 41.4 for 140 nm and 200 nm Pt NP, respectively.

5.4.3 Surface property dependence on the bubble formation

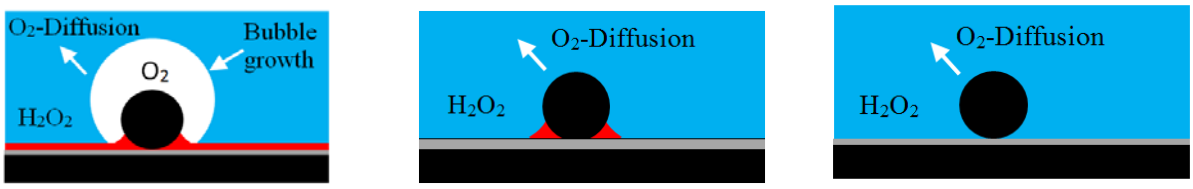

PMMA | Capillary immobilization | Bare substrate

Figure 5.9: Schematic of different situations of the contact angle comparison for different thicknesses in the cases of PMMA and PS film.

We furthermore check the impact of interfacial properties on the bubble formation. As shown in Figure 5.9, three substrates with different surface properties were. All the silicon substrates were cleaned by piranha solution. For the NP embedded in PMMA, the surface contact angle (with water) is about 65 degree. However, for the cases of the NP fixed by capillarity or depositing without immobilization the surface contact with water are ~ 0 degree, both surfaces are almost equal to clean silicon surface. Even though a single 200 nm Pt NP was used for the bubble formation with the same conditions to the case of PMMA surface, it still can not produce bubble. One could expect that oxygen diffusion is the limited parameter for the bubble formation. As a result, the surrounding environment played a role in the process of the bubble formation. It could be that the rather hydrophobic PMMA surface leads to an enrichment of the O_2 and thus favors the bubble formation.

5.5 Conclusions

In sum we investigated individual bubble nucleation and growth from a single Pt NP active site to get understanding on how a bubble forms and grows. It is investigated how parameters such as concentration of H_2O_2, size of nanoparticles and interfacial properties (hydrophobic/hydrophilic) affect the bubble formation. The bubble formation is linear with the concentration of H_2O_2. The bubble can form if the size of Pt NPs is equal or bigger than 140 nm, with the condition of NP embedded in a polymer film. It shows that the surrounding environment also played a role for the bubble formation. With hydrophilic surface, the bubbles can not form even for the size is as big as 200 nm.

6. Running bubbles driven by oxygen source´s difference

6.1 Introduction

The second law of thermodynamics prohibits specific spontaneous motion in macroscopic systems under equilibrium; nature obeys the law of equipartition [105]. Making small objects move spontaneously on solid surfaces is a key challenge in fundamental research or in practice [106-108]. There are reports about the spontaneous motion of droplets on surface or substrate [109-114]. There are no reports yet on moving bubbles with a film up to now. Here we observe and investigate the microbubble moving. The movement occurs on the basis of bubble formation from Pt NPs active sites by decomposition of H_2O_2. After the bubble production is enough to break the thin polymer film, it will move aside. We try different kinds of polymers and show that it works with hydrophobic polymers such polystyrene (PS) and polyvinyl chloride (PVC). For poly (methyl methacrylate) (PMMA), the bubbles just grow but do not move.

6.2 Bubble moving through a thin PS film

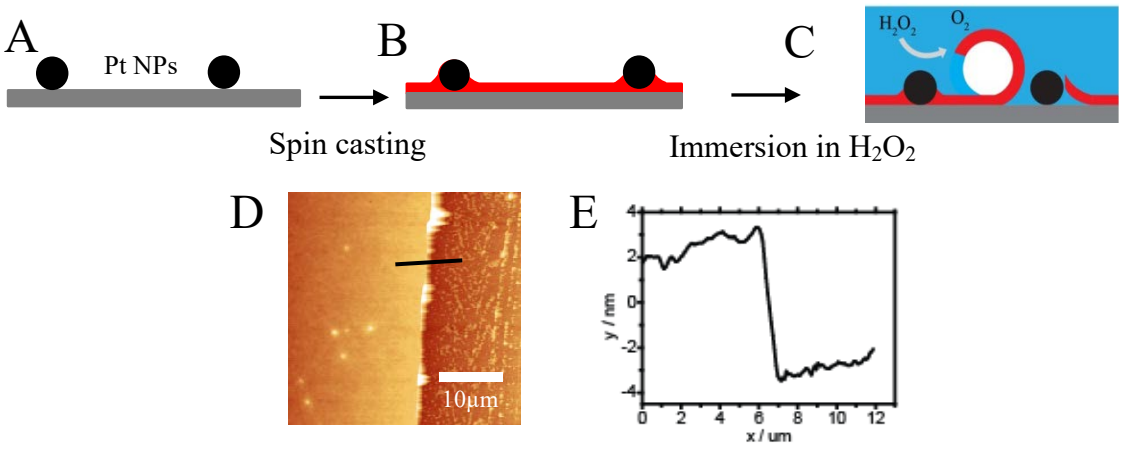

Figure 6.1 Schematic of experiment set-up. A) Pt NPs were deposited on a silicon wafer; B) PS or PVC film was deposited onto the Pt NPs pre-coated substrate; C) The system was immersed in H_2O_2 solution; D) AFM image of the height of PS film (5 nm) and E) its corresponding cross-section curve.

The experiment set up is shown in Figure 6.1. The polymer film is made of PS or PVC. Figure 6.1 C, D presents a case of 65 nm Pt NPs embedded in 5 nm thin PS film. We immerse them in H_2O_2 solution and recorded it under optical microscopy. Different from PMMA, the bubbles form after some incubation time. Them these break the film and subsequently move with the polymer film.

Figure 6.2 presents a time evolution of bubble moving on a system of a thin layer of 5 nm PS film with a 65 nm Pt NPs. It shows the sequence of optical microscopy images of the bubble forming and moving. After adding 35 % H_2O_2, a tiny bubble nucleates and grows on the PS film, as shown in Figure 6.2 B. At t = 73 s, it starts to brake the film and then quickly moves aside (with the distance of 65 μm in 0.6 s). After moving, it fixed at the original place and grew continually until t = 130 s, as shown in Figure 6.2 D. After that, the bubble moves again. From Figure 6.2 E, It is found that three new bubbles nucleate and move sideways (t = 143s).

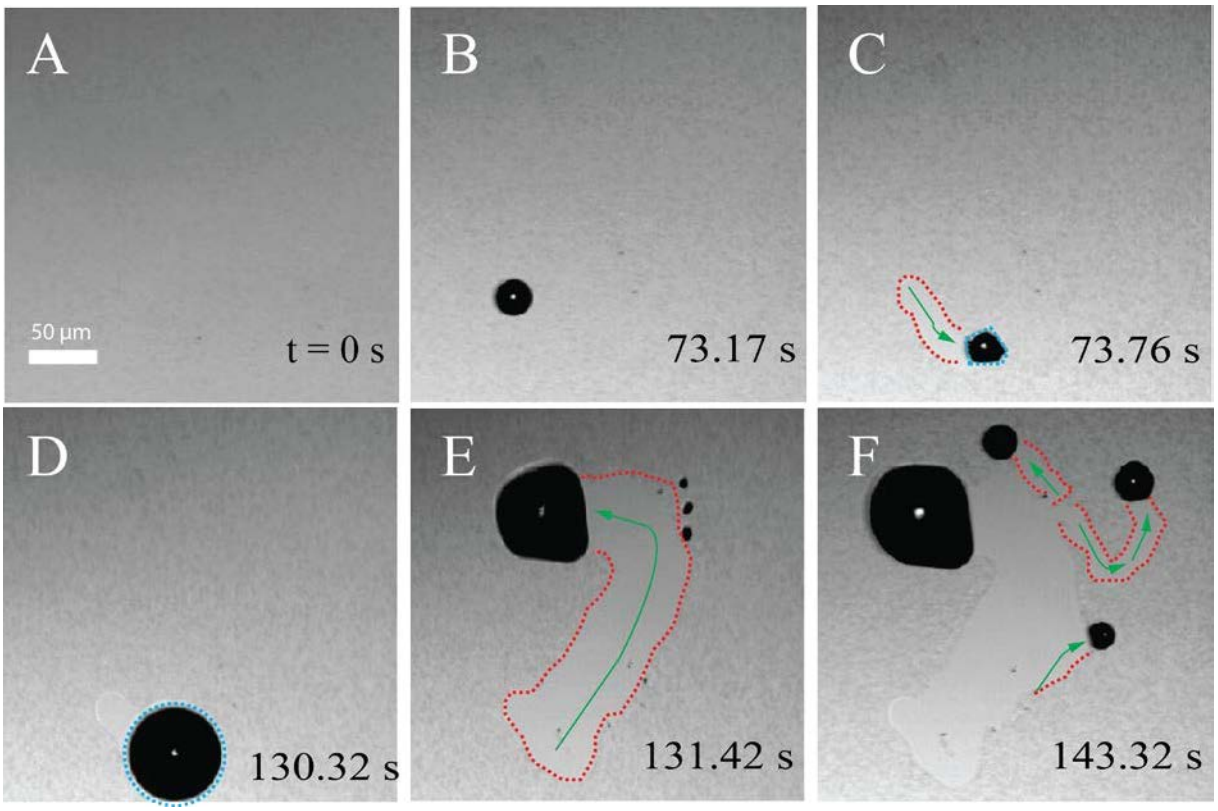

Figure 6.2 Sequence of optical microscopy images showing the bubble movement in the case of a 5 nm PS film embedded 65 nm Pt NPs.

In the followings we analyze the velocity of the bubble moving on the surface covered with a certain thickness of polymer as function of Pt NPs diameter, H_2O_2 concentration and Pt NPs coverage. For this study, the movement of the bubble is observed under the interference-enhanced optical reflected microscopy (silicon wafer with a natural oxide ~2 nm layer).

6.2.1 Dependence of bubble moving on the size

Figure 6.3 presents the high resolution AFM images of different sizes of Pt NPs embedded in 10 nm PS film. Here we used 3 Pt NPs size: 25 nm, 65 nm, and 140 nm embedded in 10 nm PS film. By keeping constant concentration of Pt NPs solution in the spin casting dispersion, we make the coverage of Pt NPs similar for each case. The number for each size of Pt NPs was around $2.5\times10^{-2}/\ \mu m^2$ by random counting the numbers of Pt NPs per areas of different regions from the optical microscopy observations.

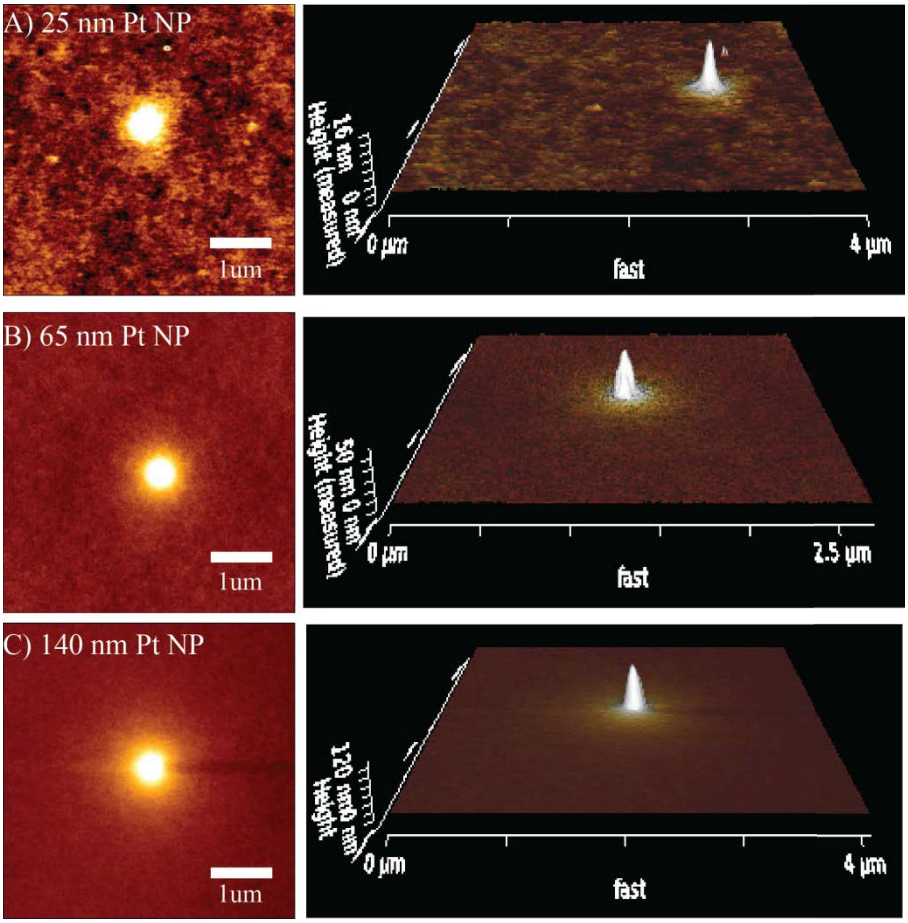

Figure 6.3 AFM images and corresponding 3D images for different diameters of Pt NPs embedded in 10 nm PS film.

The bubble velocities as a function of the diameter of the Pt NPs are shown in Figure 6.4. As already observed in Figure 6.2, the bubbles were growing in the size initially from a point. They undergo the circle process of growing-moving- stopping-growing. So we tried to measure the different moving stages (e.g. different time, size) by random to get a statistical mean velocity for each sample. Here the coverages for different size of Pt NPs were similar. The thickness of the PS film is 10 nm for each case. The data indicates that the velocity is increasing with the increasing the size of Pt NPs as shown in Figure 6.3. The average values are 30 ± 19 µm/s for 25 nm Pt NPs, 64 ± 32 µm/s for 65 nm Pt NPs, and 101 ± 26 µm/s for 140 nm Pt NPs.

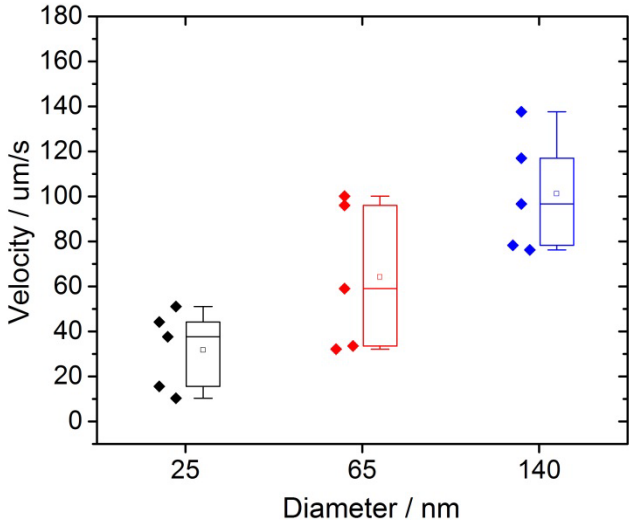

Figure 6.4 The dependence of bubble moving velocity on 10 nm PS film for different diameters of Pt NPs. The coverage of Pt NPs for all the cases similarly equal around 2.5×10^{-2} / μm^2.

6.2.2 Dependence of bubble moving on the coverage of Pt NPs

The coverage of Pt NPs embedded in thin polymer film is another important parameter for the bubble production. We get different coverage of Pt NPs by spin casting of different concentration of Pt NPs solution and then spin casting of a fixed concentration of PS toluene solution. Figure 6.5 shows optical microscopy images of such different coverages of 70 nm Pt NPs which were embedded in 10 nm PS thin films. From this data, we calculated the coverage of Pt NPs by random selecting five different regions per each sample. The coverages of Pt NPs for different sample were about 2.5×10^{-2}, 4.7×10^{-2}, 8.8×10^{-2}, and 13.4 per μm^2.

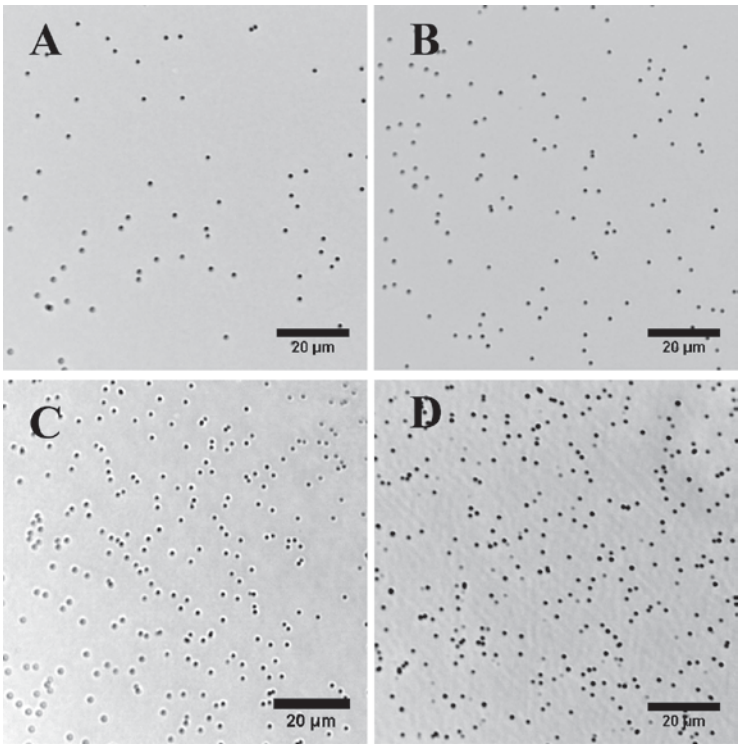

Figure 6.5 Optical microscopy images of different coverages of Pt NPs (70 nm) embedded in 10 nm PS thin films.

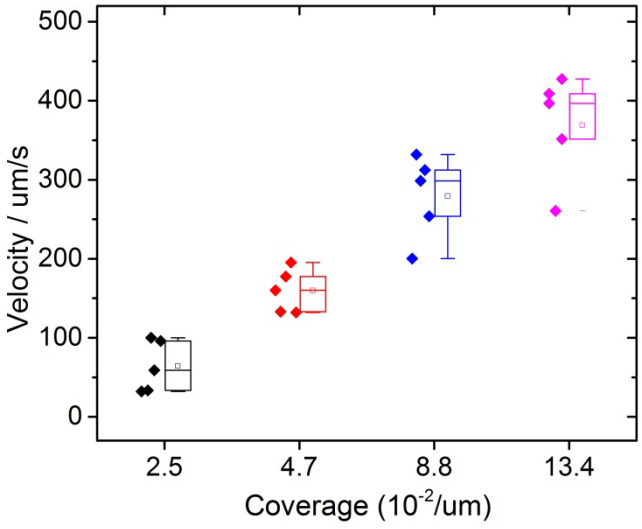

Figure 6.6 The dependence of bubble moving velocity on 10 nm PS film for different coverage of Pt NPs. The concentration of H_2O_2 is 35% w/w.

Figure 6.6 shows the dependence of the velocity on the number of Pt NPs embedded in the PS thin film. We can see that the velocity of bubble movement is nearly linear to the

coverage of Pt NPs. Increasing the coverage of Pt NPs, increases the speed of oxygen bubble movement. The average values are 64 ± 32 μm/s for the coverage of 2.5×10^{-2}/ μm^2, 160 ± 27 μm/s for the coverage of 4.7×10^{-2}/ μm^2, 279 ± 53 μm/s for the coverage of 8.8 $\times10^{-2}$/ μm^2, and 325 ± 88 μm/s for the coverage of 13.4×10^{-2}/ μm^2.

6.2.3 Dependence of bubble moving on the concentration of H_2O_2

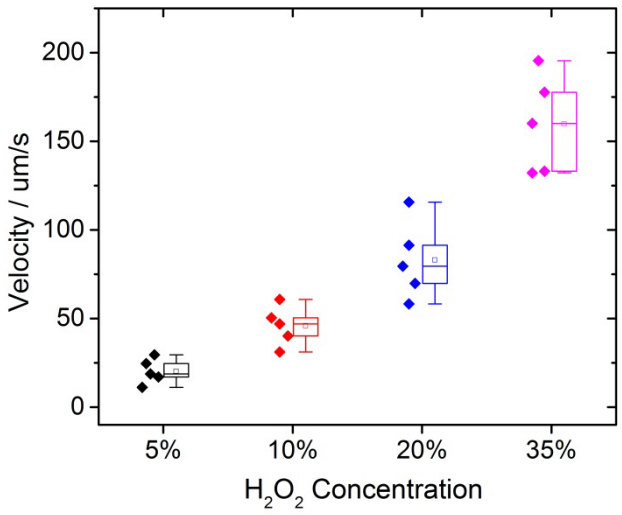

Figure 6.7 The dependence of bubble moving velocity on 10 nm PS film for different concentration of H_2O_2. The coverage of Pt NPs (65 nm) for all the cases is similar, around 4.7×10^{-2}/ μm^2.

We furthermore investigated the dependence of velocity on the concentration of H_2O_2, as shown in Figure 6.7. The concentration of H_2O_2 ranged from 5%, 10%, 20% to 35%. The size of NPs is 65 nm with the coverage of 4.7×10^{-2}/ μm^2. As shown in Figure 6.7, the velocities are proportional to the different concentration of H_2O_2.

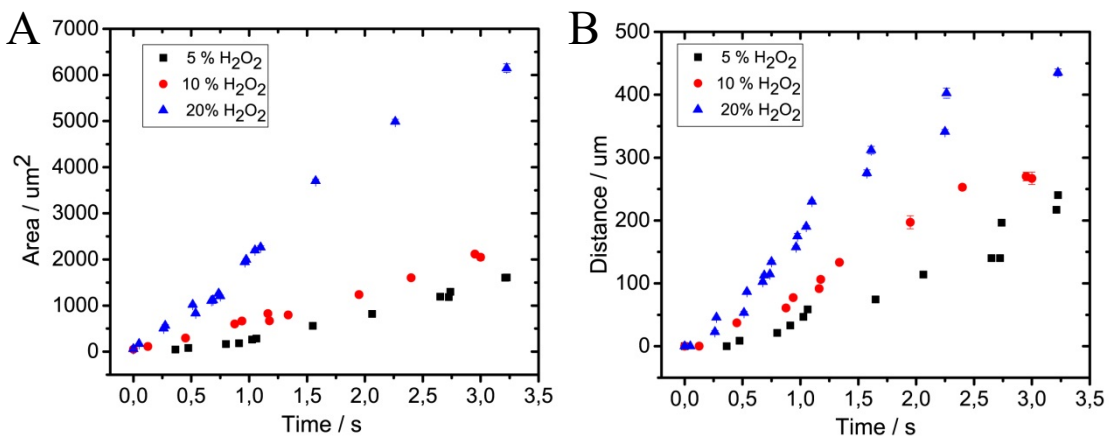

Figure 6.8 The bubble area as a function of time and the bubble moving length as a function of time on 10 nm PS film for different concentrations of H_2O_2. The coverage of Pt NPs (65 nm) for all the cases is similar, around $4.7\times10^{-2}/\ \mu m^2$.

As already described, the bubble nucleated and broke the film which resulted in a groove as we see from the optical microscopy (Figure 6.2). Then new bubbles nucleate at the edge of the polymer film terrace. After it is enough big, it moves again like the previous one. In figure 6.8 we plot the bubble area and the distance of bubble moving as function of time for the new bubble forming from the beginning with different concentrations of H_2O_2. The shape of bubble is not always perfectly spherical during their moving. So when measuring the area of the bubble, we used their outlines. For low concentration of H_2O_2, the bubbles grow slower than for high concentration. The distance of bubble moving was increasing during the bubble moving. The growth is not continues, sometimes it stops at a certain point and grows, then moved again. The slope of the distance with time is proportional to the concentration of H_2O_2.

6.2.4 Dependence of bubble moving on height of polymer film

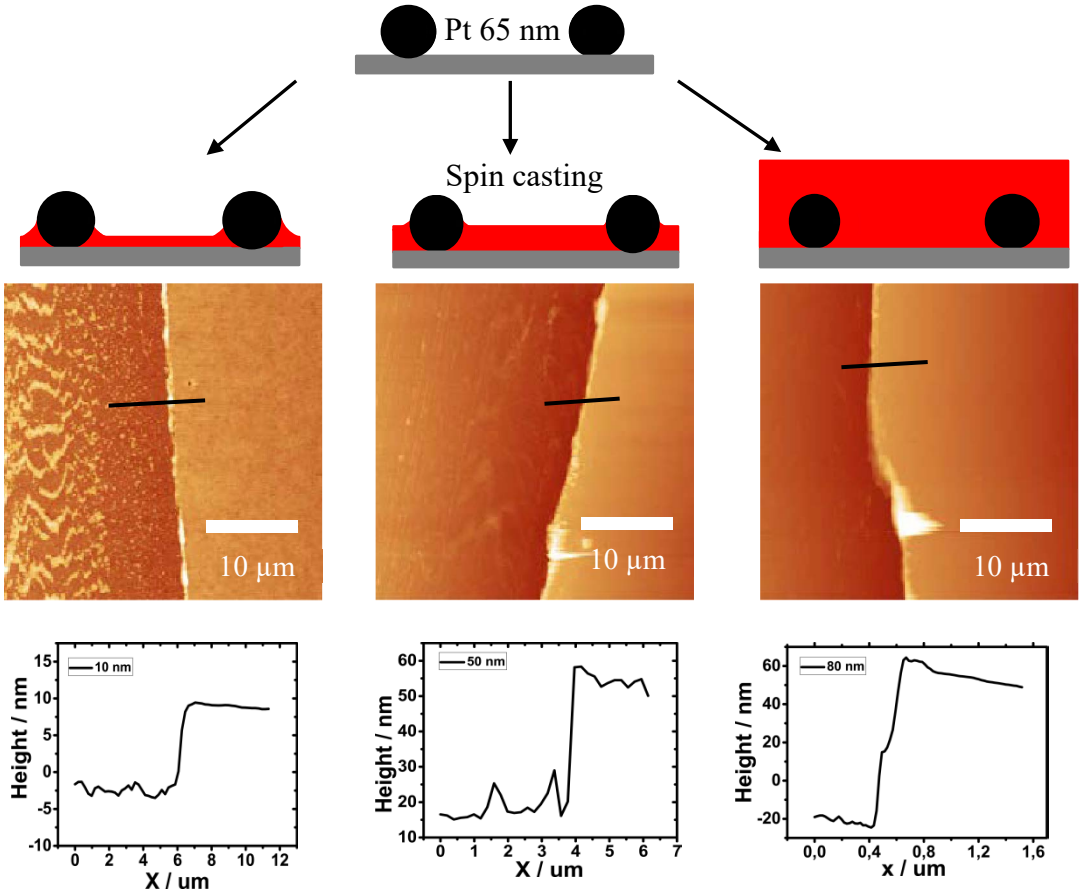

Figure 6.9 Schematic illustration of preparation of different thicknesses of the PS film by spin casting of different concentrations of PS solution in toluene on Pt NP coated substrates (the upper part). Thickness of the PS film was measured by AFM method (the middle part) and corresponding cross section analysis (the down part).

We present different thicknesses of the PS film to study their effect on bubble moving. Figure 6.9 presented the AFM measurement of the different thicknesses of the PS film. By spin casting different concentrations of PS solution, we can control the thickness of PS film onto the 65 nm Pt NPs coated substrate. From the section analysis it is easy to observe that the thickness for each sample were 10 nm, 35 nm, and 80 nm at the edge of the film terrace, respectively.

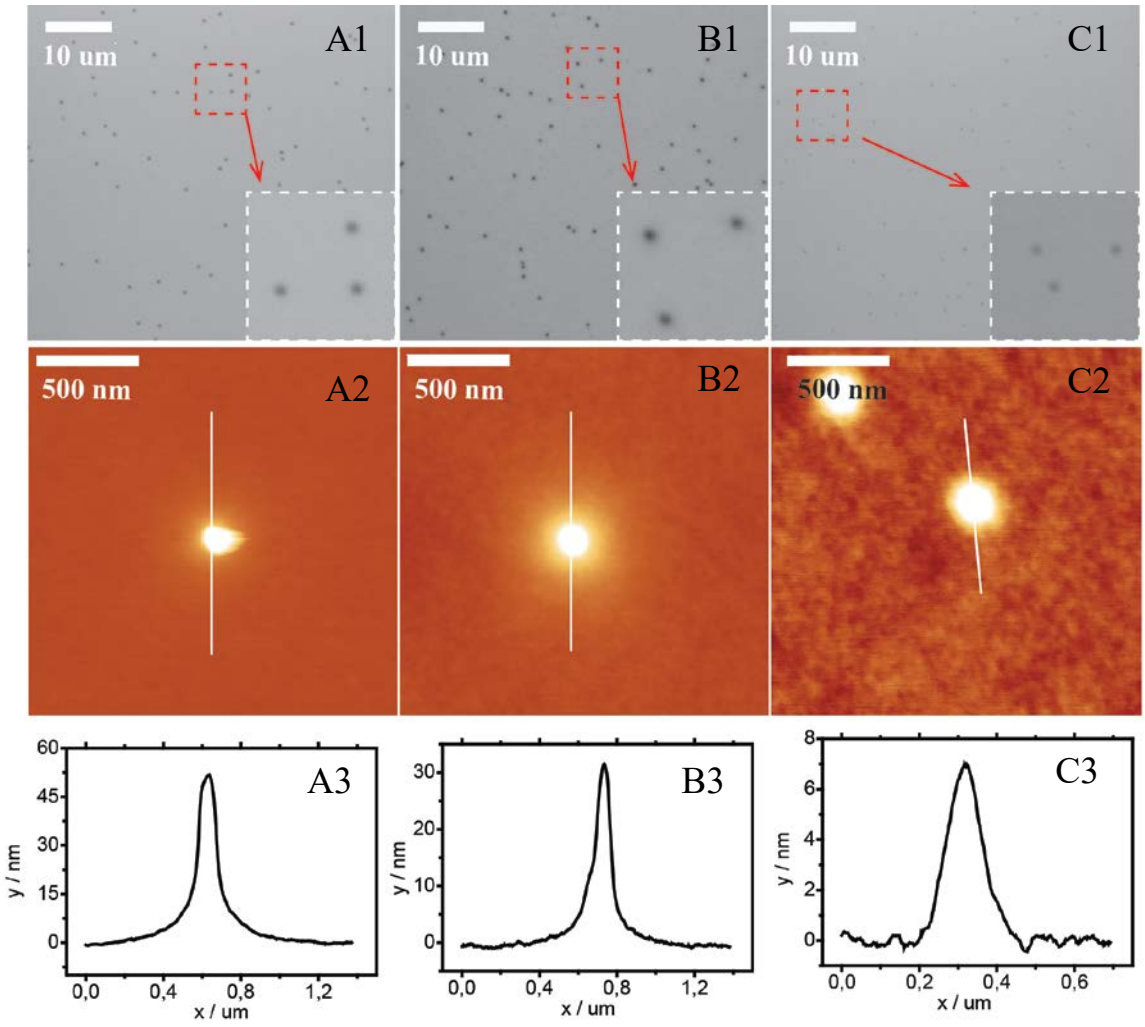

Figure 6.10 OM and corresponding AFM images of the thicknesses of A: 10 nm, B: 35 nm and C: 80 nm of the PS film embedded on 65 nm Pt NPs coated substrate.

Figure 6.10 shows the structure for the 65 nm Pt NPs embedded in different thicknesses of PS films. In the upper part, the optical microscopy images show that we can localize the NPs, even for the 80 nm PS film. The images inserted in the upper part of Figure 6.10 show the high resolution of OM images. In the middle and low part, we show the AFM images and corresponding cross section analysis of different thicknesses of the PS film-Pt NPs structure. The height of Pt in the NP-polymer film profile is 55 nm for 10 nm PS film, 30 nm for 35 nm PS film, and 7 nm for 80 nm PS film.

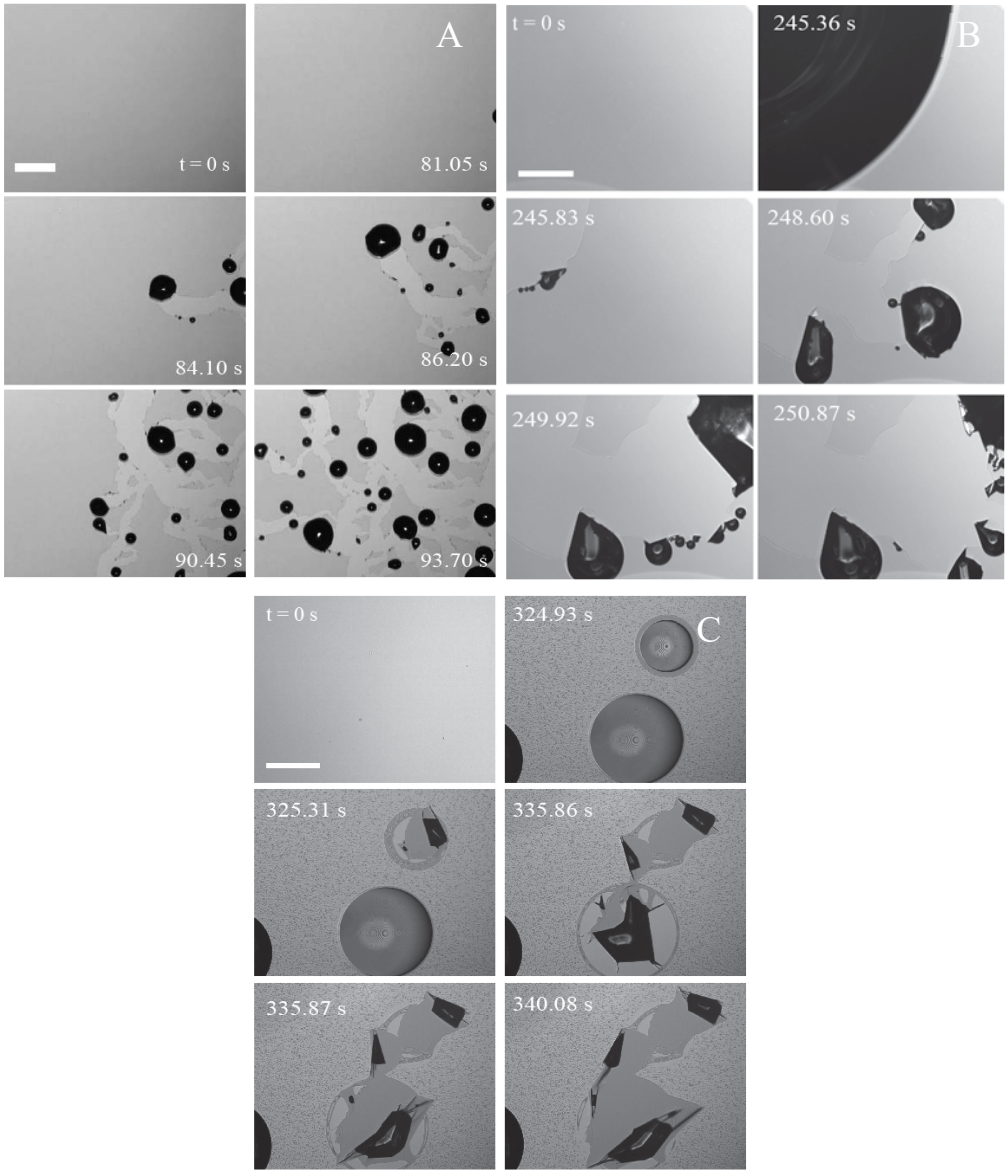

Figure 6.11 Sequential OM images of bubble moving for A: 10nm, B: 35 nm, and C: 80 nm thicknesses of the PS film embedded on 65 nm Pt NPs coated substrate. The coverage is about 2.5×10^{-2}/ μm^2. Scale bar: 200 μm.

Figure 6.11 presents the sequence of optical microscopy images for different thicknesses of the PS film on 65 nm Pt NPs during bubble moving. Figure 6.11 A shows the bubble moving in the case of 10 nm PS film. After adding 35% w/w H_2O_2, the bubble started moving at 81 s and left the groove behind the film being taken away with bubble as was shown in Figure 6.2. When the thickness of film increased to 35 nm, it needs bigger bubbles to break the film, as shown in Figure 6.10 B. In addition, it also underwent longer time (245 s) to break the film and make bubbles move. Samples with thicker layers of PS film behave different. For the thickness of 80 nm PS film, oxygen accumulated underneath the film.

When the thickness is increased to 200 nm, which was very big when compared with 65 nm Pt NPs, it only produced a bubble without bubble moving after undergoing a long incubation period. We think that the H_2O_2 may penetrate the thick film and react with the Pt NPs.

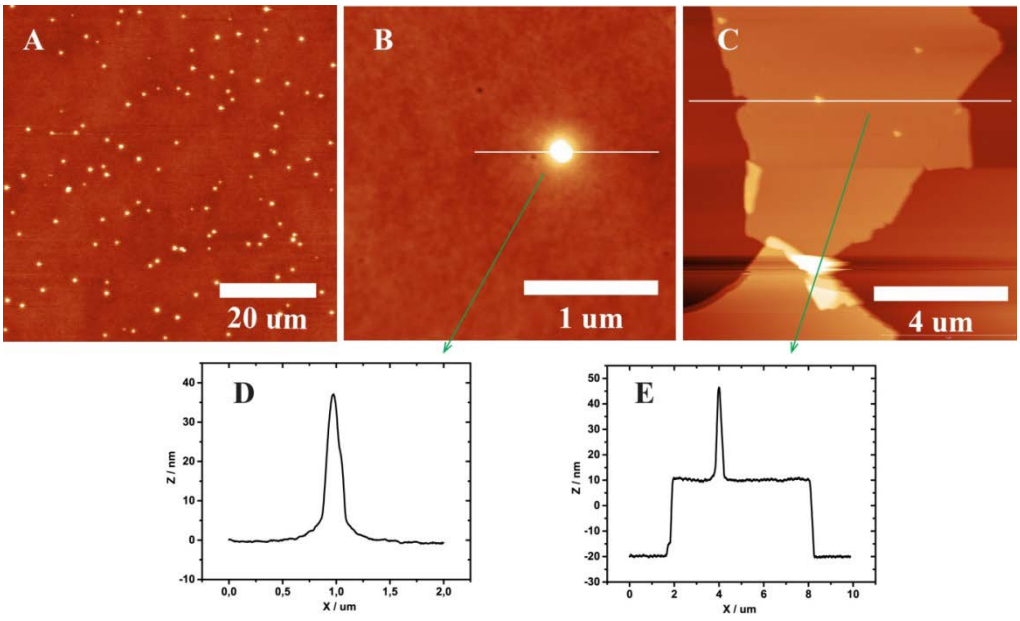

Figure 6.12 A) AFM image and, B) high resolution AFM image of 65 nm Pt embedded in PS thin films before adding the H_2O_2. C) AFM images after bubble moving within H_2O_2. D, and E) are the corresponding cross section images of B), and C).

After bubble moving, we dried the sample and investigated with AFM, as shown in Figure 6.12. Figures 6.12 A, B are the AFM and high resolution of AFM images of the substrate before the bubble moving experiment. The thickness of PS film is 30 nm. The coverage of 65 nm Pt NPs is about $2.5\times10^{-2}/\ \mu m^2$. After the bubbles break the PS film, the Pt NPs were also taken away together with bubble, which could be proved by the AFM image in Figure 6.12 C. The area covered with monolayer of PS film is different from the bare substrate where the film was gone the bubble moving. We can see that there remained no Pt NPs on the bare silicon substrate (Figure 6.12 C). However, for substrate surface with the film the Pt NPs still sticked to the film. From the section analysis it is easy to observe that the regions where the terrace edgy has the height of 30 nm. The height of Pt NP is around 35 nm.

6.3 Bubble running through thin polyvinyl chloride (PVC) film

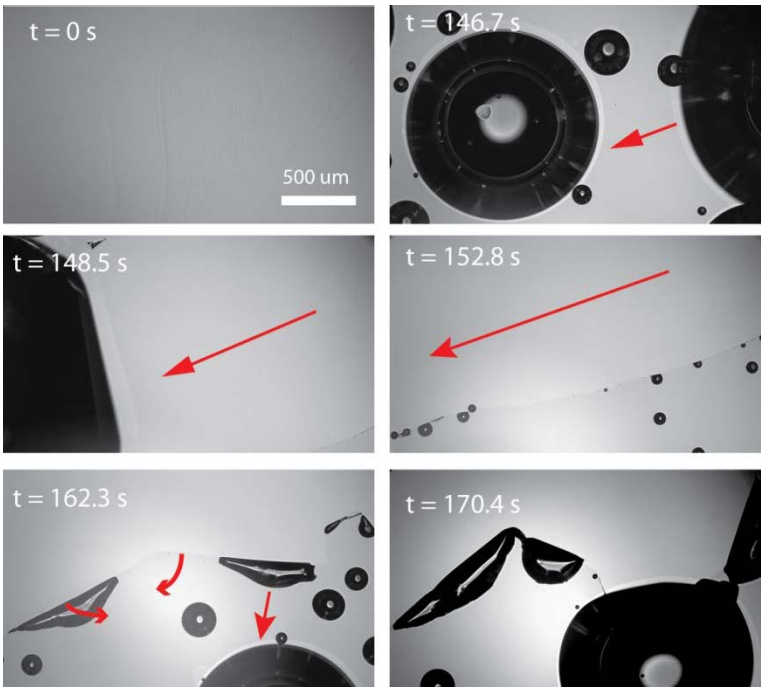

Figure 6.13 Sequence of optical microscopy images showing the bubble movement in the case of a 7 nm PVC film embedded 65 nm Pt NPs.

Figure 6.13 shows the bubble moving for the thickness of 7 nm PVC with 65 nm Pt NPs. The behavior of bubble moving is similar to the PS case.

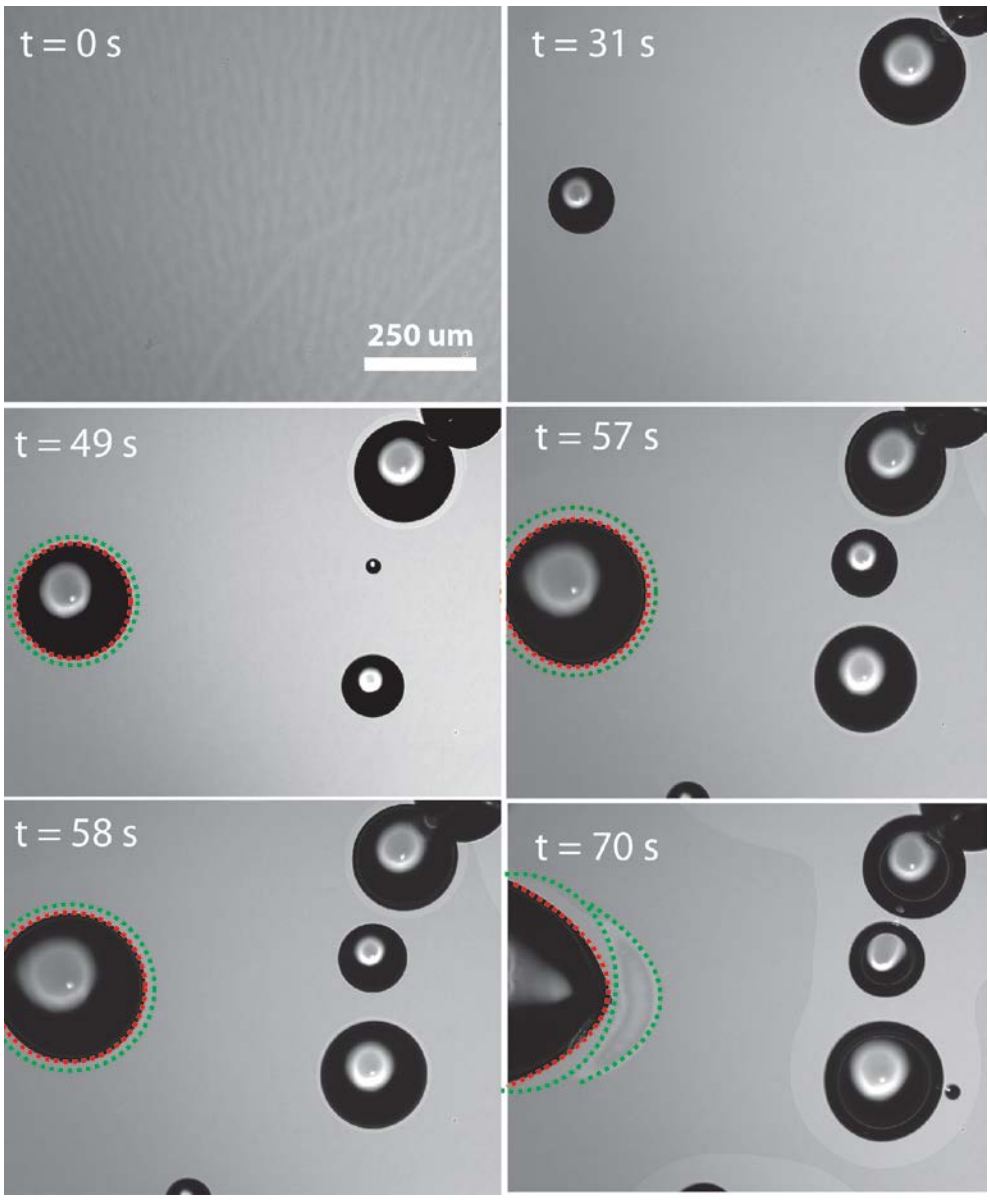

Figure 6.14 Sequence of optical microscopy images showing the bubble production in the case of a 14 nm PVC film embedded 65 nm Pt NPs.

Furthermore, we increased the thickness of PVC film from 7 nm to 14 nm. The bubble formation behavior is presented in Figure 6.14. The bubble was growing on the PVC film meanwhile it also accumulated underneath the film. This phenomenon is similar with the high thickness of PS film. As shown in Figure 6.14, we can see that there was a different region between dashed green and red circles with outside which is the accumulation of oxygen under the film. At time of 70 s, the oxygen broke the film and the shape of bubble was also changed due to the film fracture. Compared with the Pt diameter of 65 nm, the thickness of 14 nm is not so big that cover the Pt active sites.

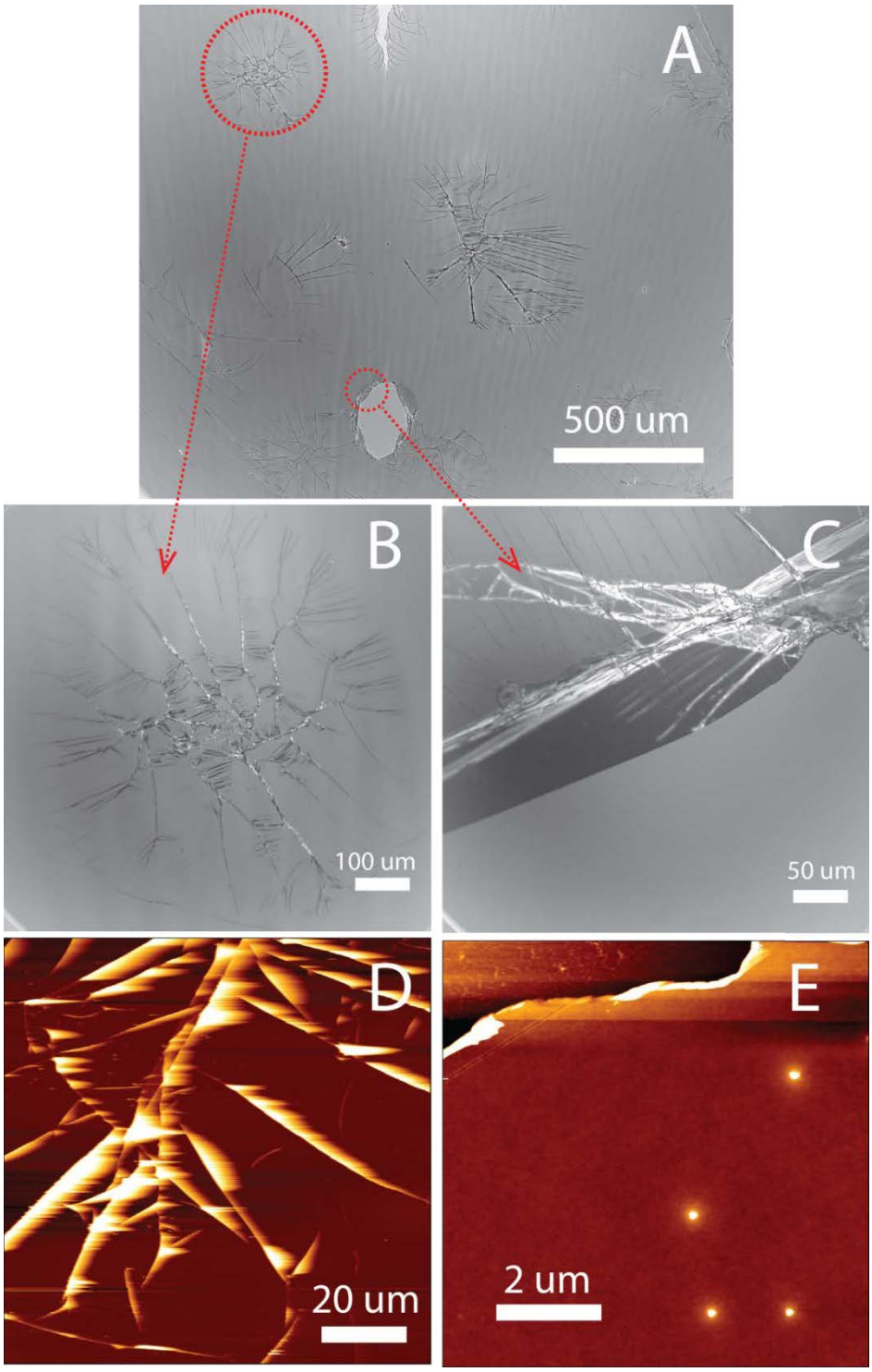

Figure 6.15 Optical microscopy images showing the 14 nm PVC film fracture and AFM images show the details of breaking film structure.

We stop the bubble formation experiment for the situation of 14 nm and measure its surface under the AFM to get structure details. Figure 6.15 A showed the optical microscopy image of a typical PVC structure after the bubbles form and the films break. Figure 6.15 B, C were the high resolution optical microscopy images by taking the regions from the A. Figure 6.15 B shown a bubble was about to break the film and Figure 6.15 C shows the terrace edge

where the film had already been broken by the bubble. The details of these two typical film structures were shown by the AFM images as shown in Figure 6.15 C, D. PMMA film, it just formed the bubbles on top of the film that secondly detached, but they do not move any more.

We measured the contact angle for the PS, PVC, and PMMA film. The advancing contact angle and receding contact angle for PS is 112±5 º and 92±7 º. The advancing contact angle and receding contact angle for PVC is 107±3 º and 80±2 º. However, the advancing contact angle and receding contact angle for PMMA is 68±2 º and 66±1 º.

6.4 The evolution of the polymer film fracture and rolling

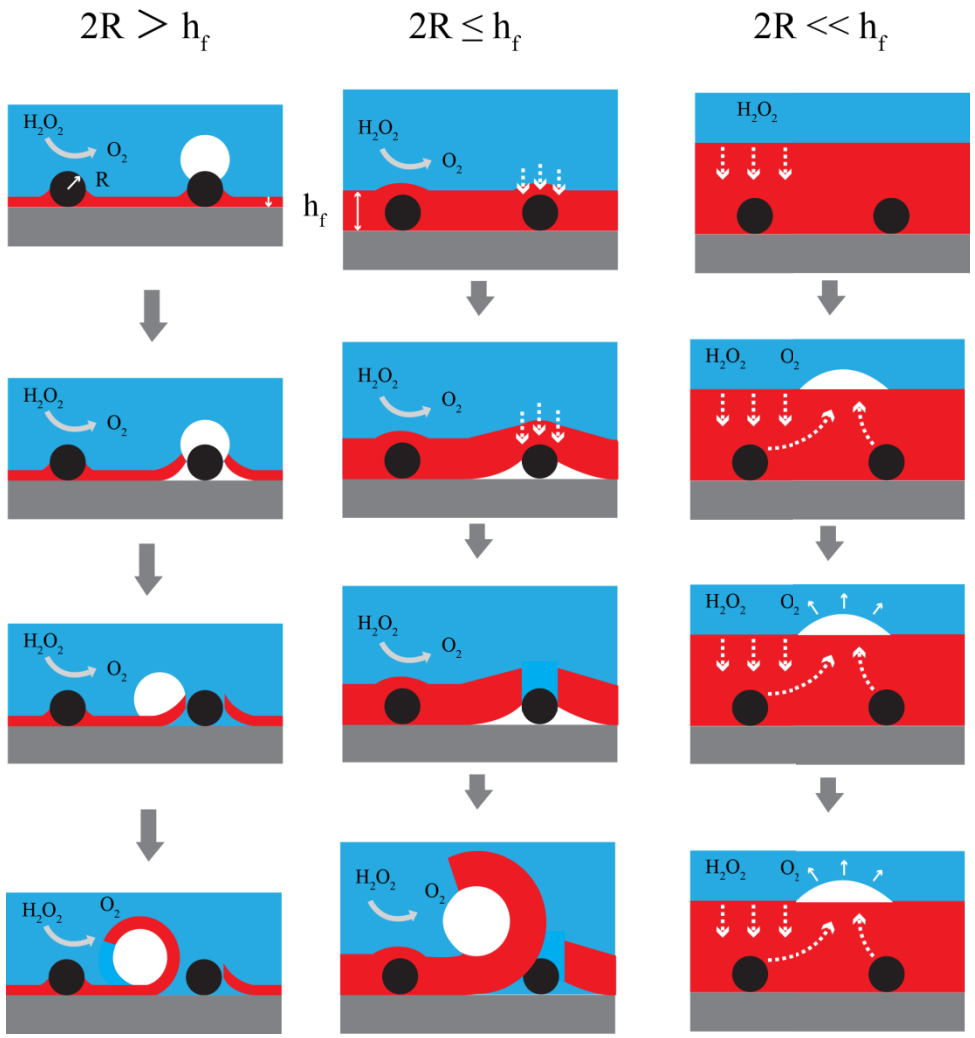

Figure 6.16 Schematic description of the fracture and rolling evolution from the thin to thick polymer films during bubble moving. R is the radius of the NPs and h_f is the thickness of polymer film.

According to above experimental results, the morphology may evolve following the scenario presented in Figure 6.16. For the thin layer of polymer film, the H_2O_2 can contact directly with the Pt NPs and produce the oxygen. The oxygen molecules go through the film to the substrate. When they form the bubble, it could break the film and roll with the polymer film. When the thickness of the film is near or higher than the size of Pt NPs, it would be dominate that the oxygen molecules accumulate underneath of the film and form the bubble. When its volume is enough it will break the film and move. However, when the film thickness is much higher than the size of Pt NPs, the diffusion through the polymer film of H_2O_2 and later of the O_2 are dominating. It is reasonable that the O_2 production would be reduced (the long distance between the Pt NPs active sites and the H_2O_2), which goes along to the fact that in the time frame work. We did not observe blistering or film wrapping.

6.5 Conclusion

We observed and investigated the microbubble moving over an ultrathin polymer film for the first time. The movement occurs on the basis of bubble formation from Pt NPs active sites by decomposition of H_2O_2. After the bubble production is enough to break the thin polymer film IT will move aside. We try different kinds of polymers and shows that it works with hydrophobic polymer such as polystyrene (PS) and polyvinyl chloride (PVC). For poly (methyl methacrylate) (PMMA), the bubbles just grow but do not move that means the bubble move.

7. Summary

The present thesis focuses on nanoparticles (NPs) attached to solid/liquid interface. In this thesis, monodisperse Pt NPs with sizes ranging from 5 to 200 nm were synthesized by a multistep seed-mediated growth approach. These were deposited on planar substrates to study their behavior at solid/liquid interface.

Chapter 3 describes a new route to immobilize NPs on substrate through capillary condensation. Being different from the conventional immobilization route, we attach the NPs to the bare substrate first and deposit the binding agent afterwards. Ultrasonication tests prove that this can strongly increase the adhesion of the NPs on the substrate. We assume that the improved adhesion is caused by extra amounts of binding agent accumulated in the between vicinity where the NPs contacts the substrate. Supposedly capillary effects (capillary condensation) induced by the narrow annular gap next to the contact between NPs and substrate cause this local enrichment of binding agent. AFM data reveal that there was a footprint at the NP´s original place left after moving it away which prove this assumption. In addition, the new route is universal, because it works for different types of NPs (Pt-NPs and Au-NPs) as well as for different types of adhesion agents (APTES, C_{60} and polymer).

Chapter 4 presents the imaging of objects with dimensions much smaller than the Rayleigh resolution limit by conventional optical microscopy. In one route, they can be localized by the lateral distortion of thin film around them on the planar substrate that could be transparent (liquid film); frozen (polymer), or switchable (film of low melting point molecules). In another route, we used silica coated wafers to enhance the contrast to image the NPs. Due to the optical reflected interference, the contrast for the NPs is enhanced so that they can be localized.

Individual bubble formation from a single localized Pt NP active sit at planar substrate was investigated in chapter 5. An individual Pt NP was used as active site to decompose the H_2O_2 to produce the oxygen bubble. We studied the influence of the concentration of H_2O_2, the size of active site, and the substrate properties on the bubble formation. We combine the optical microscopy and AFM measurement to localize the Pt NP. Optical microscopy was used to characterize individual bubble formation and growth in real time.

The moving of bubble over a thin polymer film was presented in chapter 6. It was found that in the system of the hydrophobic polymer (PS/PVC) thin films coated on the Pt NPs-substrate immersed within H_2O_2, bubbles could be produced that suddenly wrapped up the

thin film. The oxygen bubbles formed at the Pt NPs active sites and broke the thin film. These bubbles grew in size during moving sideways through the polymer terrace area, taking the polymer film away and leaving behind a groove. The bubble moving velocity is dependent on the parameters of the concentration of H_2O_2, the size of Pt NPs, the thickness of film, and the interfacial properties of polymers.

Bibliography

[1] Taguchi, T.; Isozaki, K.; Miki, K. *Adv. Mater.* 2012, 24, 6462-6467.

[2] Strayer, M. E.; Binz, J. M.; Tanase, M.; Shahri, S. M. K.; Sharma, R.; Rioux, R. M.; Mallouk, T. E. *J. Am. Chem. Soc.* 2014, 136, 5687-5696.

[3] Riskin, M.; Tel-Vered, R.; Lioubashevski, O.; Willner, I. *J. Am. Chem. Soc.* 2009, 131, 7368-7378.

[4] Fan, M.; Andrade, G. F. S.; Brolo, A. G. *Analytica. Chimica. Acta.* 2011, 693, 7-25.

[5] Liu, Y.; Khabashesku, V. N.; Halas, N. J. *J. Am. Chem. Soc.* 2005, 127, 3712-3713.

[6] Park, M. H.; Ofir, Y.; Samanta, B.; Arumugam, P.; Miranda, O. R.; Rotello, V. M. *Adv. Mater.* 2008, 20, 4185-4188.

[7] Xia, Y.; Ramgopal, Y.; Li, H.; Shang, L.; Srinivas, P.; Kickhoefer, V. A.; Rome, L. H.; Preiser, P. R.; Boey, F.; Zhang, H.; Venkatraman, S. S. *ACS Nano* 2010, 4, 1417-1424.

[8] Karpitschka, S.; Dietrich, E.; Seddon, J. R. T.; Zandvliet, H. J. W.; Lohse, D.; Riegler, H. *Phys. Rev. Lett*. 2012, 109, 066102.

[9] Köhler, R.; Lazar, P.; Riegler, H. *App. Phys. Lett*. 2006, 89, 241906.

[10] Wu, Y.; Wu, Z.; Lin, X.; He, Q.; Li, J. *ACS Nano*. 2012, 12, 10910.

[11] Butt, H.-J.; Graf, K., Kappl M. Physics and Chemistry of Interfaces. John Wiley & Sons, New York, 1997.

[12] Adamson, A. W.; Gast, A. P. Physical Chemistry of surfaces. 6th ed, Wiley-VCH Verlag GmbH & Co. KGaA, Weinheim, 2003.

[13] Adkins, C. J. Equilibrium thermodynamics. 9th ed., Cambridge University Press, 1984.

[14] Butt, H.-J.; Kappl M. *Adv. Colloid Interface Sci*. 2009, 146, 48-60.

[15] Adkins, C. J.; Paula, J. D. Atkins´s Physical Chemistry. Oxford University Press, 2010.

[16] Saleh, B. E. A.; Teich, M. C. Fundamentals of Photonics. 2th ed., Wiley-VCH Verlag GmbH & Co. KGaA, Weinheim, 2007.

[17] Roychoudhuri, C. Fundamentals of Photonics. SPIE Digital Library, 2008.

[18] Kashchiev, D. Nucleation, basic theory with applications, Butterworth-Heinemann, Oxford, 2000.

[19] Jones, S. F.; Evans G. M.; Galvin K. P. *Adv. Colloid Interface Sci*. 1999, 80, 27-50.

[20] Auer, S.; Frenkel D. *Nature* 2001, 409, 1020-1023.

[21] Cacciuto A.; Auer S.; Frenkel D. *Nature* 2004, 428, 404-406.

[22] Schmelzer, J. W. P. Nucleation theory and application, Wiley-VCH Verlag GmbH & Co. KGaA, Weinheim, 2005.

[23] Blander, M.; Katz J. L. 1975, *AIChE J*. 21, 833-848.

[24] Blander, M. *Adv. Colloid Interface Sci*. 1979, 10, 1-32.

[25] Ajekseechkin, N. V. *J. Phys. Chem. B*. 2012, 116, 9445-9459.

[26] German, S. R.; Edwards, M. A.; Ren, H.; White, H. S. *J. Am Chem. Soc*. 2018, DOI: 10.1021/jacs.7b13457.

[27] Chen, Q.; Wiedenroth, H. S.; German, S. R.; White, H. S. *J. Am Chem. Soc*. 2015, 137, 12064-12069.

[28] Wang, Y.; Zaytsev, M. E.; The, H. L.; Eijkel, J. C. T.; Zandvliet, H. J. W.; Zhang, X.; Lohse, D. *ACS Nano* 2017, 11, 2045-2051.

[29] Baffou, G.; Polleux, J.; Rigneault, H.; Monneret, S. *J. Phys. Chem. C*. 2014, 118, 4890-4898.

[30] Hemmingsen, E. A. *Nature* 1977, 267, 141-142.

[31] Fu, Q.; Zhu, Z.; Dou, J.; Zheng, X.; Xu, R.; Wu, M.; Lei, Y. *ACS Appl. Mater. Interfaces* 2015, 7, 13322-13328.

[32] Murray, R. W. *Chem. Rev.* 2008, 108, 2688-2720.

[33] Moreau, A.; Cirací, C.; Mock, J. J.; Hill, R. T.; Wang, Q.; Wiley, B. J.; Chilkoti, A.; Smith, D. R. *Nature* 2012, 492, 86-89.

[34] Yang, J.; Choi, M. K.; Kim, D.; Hyeon, T. *Adv. Mater.* 2016, 28, 1176-1207.

[35] Kagan, C. R.; Lifshitz, E.; Sargent, E. H.; Talapin, D. V. *Science* 2016, 353, 885.

[36] Jin, B.; He, J. *ACS Photonics* 2017, 4, 188-196.

[37] Karakouz, T.; Maoz, B. M.; Lando, G.; Vaskevich, A.; Rubinstein, I. *ACS Appl. Mater. Interfaces* 2011, 3, 978-987.

[38] Gould, T.; Izar, A.; Weimer, A. W.; Falconer, J. L.; Medlin, J. W. *ACS Catal*. 2014, 4, 2714-2717.

[39] Dafinone, M. I.; Feng, G.; Brugarolas, T.; Tettey, K. E.; Lee, D. *ACS Nano* 2011, 5, 5078-5087.

[40] O´Neill, B. T.; Jackson, D. H. K.; Lee, J.; Canlas, C.; Stair, P. C.; Marshall, C. L.; Elam, J. W.; Kuech, T. F.; Dumesic, J. A. *ACS Catal*. 2015, 5, 1804-1825.

[41] Pick, C.; Argento, C.; Drazer, G.; Frechette, J. *Langmuir* 2015, 31, 10725-10733.

[42] Karpitschka, S.; Hanske, C.; Fery, A.; Riegler, H. *Langmuir* 2014, 30, 6826-6830.

[43] Williams, S. E.; Davies, P. R.; Bowen, J. L.; Allender, C. *J. Nanomater.* 2013, 3, 192-203.

[44] Kaminska, A.; Inya-Agha, O.; Forster, R. J.; Keyes, T. E. *Phys. Chem. Chem. Phys.* 2008, 10, 4172-4180.

[45] Young, S. L.; Kellon, J. E.; Hutchison, J. E. *J. Am Chem. Soc*. 2016, 138, 13975-13984.

[46] Toolan, D. T. W.; Fujii, S.; Ebbens, S. J.; Nakamura, Y.; Howse, J. R. *Soft Matter* 2014, 10, 8804-8812.

[47] Hong, Y.-K.; Kim, H.; Lee, G.; Kim, W. *Appl. Phys. Lett.* 2002, 80, 844-846.

The NPs stick to the surface because of VdW interactions. The attached NPs can be seen by AFM and SEM.

[48] Butt, H.-R.; Graf, K.; Kappl, M. Physics and Chemistry of Interfaces; Krieg, U., Ed.; Wiley-VCH Verlag GmbH: Weiheim, 2006.

[49] Fisher, L. R.; Israelachvili, J. N. *Nature* 1979, 277, 548-549.

[50] Gemici, Z., Schwachulla, P. I., Williamson, E. H., Rubner, M. F.; Cohen, R. E. *Nano Lett.* 2009, 9, 1064-1070.

[51] Yoon, S.-S.; Khang, D.-Y. *Nano Lett.* 2016, 16, 3550-3556.

[52] Shardt, N.; Elliott, J. A. W. *J. Phys. Chem. A*. 2016, 120, 2194-2200.

[53] Israelachvili, J. N. Intermolecular and surface forces; Academic Press, London, 1991.

[54] Chen, A.; Holt-Hindle, P. *Chem. Rev*. 2010, 110, 3767-3804.

[55] Sau, T. K.; Rogach, A. L.; Jäckel, F.; Klar, T. A.; Feldmann, J. *Adv. Mater*. 2010, 22, 1805-1825.

[56] Wu, L.; Mendoza-Garcia, A.; Li, Q.; Sun, S. *Chem. Rev*. 2016, 116, 10473-10512.

[57] Su, Q.; Ma, X.; Dong, J.; Jiang, C.; Qian, W. *ACS Appl. Mater. Interfaces* 2011, 3, 1873-1879.

[58] Xia, Y.; Li, W.; Cobley, C. M.; Chen, J.; Xia, X.; Zhang, Q.; Yang, M.; Cho, E. C.; Brown, P. K. *Acc. Chem. Res*. 2011, 44, 914-924.

[59] Chithrani, B. D.; Ghazani, A. A.; Chan, W. C. W. *Nano Lett*. 2006, 6, 662–668.

[60] Feinstone, S. M.; Kapikian, A. Z.; Purcell, R. H. *Science* 1973, 182, 1026–1028.

[61] Hockley, D. J.; Wood, R. D.; Jacobs, J. P.; Garrett, A. J. *J. Gen. Virol*. 1988, 69, 2455-2469.

[62] Pease, L. F. III; Lipin, D. I.; Tsai, D.-E.; Zachariah, M. R.; Lua, L. H. L.; Tarlov, M. J.; Middelberg, A. P. J. *Biotechnol. Bioeng*. 2009, 102, 845–855.

[63] Binnig, G.; Quate, C. F.; Gerber, C. *Phys. Rev. Lett*. 1986, 56, 930–933.

[64] Ebenstein, Y.; Nahum, E.; Banin, U. *Nano Lett*. 2002, 2, 945–950.

[65] Barker, A. L.; Gonsalves, M.; Macpherson, J. V.; Slevin, C. J.; Unwin, P. R. *Anal. Chim. Acta* 1999, 385, 223-240.

[66] Polcari, D.; Dauphin-Ducharme, P.; Mauzeroll, J. *Chem. Rev.* 2016, 116, 13234-13278.

[67] Kai, T.; Zoski, C. G.; Brad, A. J. *Chem. Commun.* 2018, 54, 1934-1947.

[68] Bard, A. J.; Fan, F. R. F.; Kwak, J.; Lev, O. *Anal. Chem.* 1989, 61, 132-138.

[69] Barker, A. L.; Unwin, P. R.; Zhang, J. *Electrochem. Commun.* 2001, 3, 372-378.

[70] Cornut, R.; Lefrou, C. *J. Electroanal. Chem.* 2008, 623, 197-203.

[71] Hickel, W.; Kamp, D.; Knoll, W. *Nature* 1989, 339, 186.

[72] Peterson, A. W.; Halter, M.; Tona, A., Plant, A. L. *BMC Cell Biology* 2014, 15:35.

[73] Campbell, C. T.; Kim, G. *Biomater.* 2007, 28, 2380-2392.

[74] Mudanyali, O.; McLeod, E.; Luo, W.; Greenbaum, A.; Coskun, A. F.; Hennequin, Y.; Allier, C. P.; Ozcan, A. *Nature Photonics* 2013, 7, 247-254.

[75] Wei, Q.; Qi, H.; Luo, W.; Tseng, D.; Ki, S. J.; Wan, Z.; Göröcs, Z.; Bentolila, L. A.; Wu, T.-T.; Sun, R.; Ozcan, A. *ACS Nano* 2013, 7, 9147-9155.

[76] Daaboul, G.; Yurt, A.; Zhang, X.; Hwang, G.; Goldberg, B.; Ünlü, M. S. *Nano lett*. 2010, 10, 4727-4731.

[77] Scherr, S. M.; Daaboul, G. G.; Trueb, J.; Sevenler, D.; Fawcett, H.; Goldberg, B.; Connor, J. H.; Ünlü, M. S. *ACS Nano* 2016, 10, 2827-2833.

[78] Liu, Y.; Huang, C. Z. *ACS Nano* 2013, 7, 11026-11034.

[79] Huang, F. M.; Zheludev, N. I. *Nano Lett*. 2009, 9, 1249-1254.

[80] Huang, B.; Babcock, H.; Zhuang, X. *Cell* 2010, 143, 1047-1058.

[81] Kner, P.; Chhun, B. B.; Griffis, E. R.; Winoto, L.; Gustafsson, M. G. L. Nature Methods 2009, 6, 339-342.

[82] Fitzgibbon, J.; Bell, K.; King, E.; Oparka, K. Plant Physiol. 2010, 153, 1453-1463.

[83] Riegler, H.; Köhler, R. *Nature Phys*. 2007, 3, 890-894.

[84] Gaskell, P. E.; Skulason, H. S.; Rodenchuk, C.; Szkopek, T. *App. Phys. Lett*. 2009, 94, 143101.

[85] Roddaro, S.; Pingue, P.; Piazza, V.; Pellegrini, V; Beltram, F. *Nano Lett*. 2007, 7, 2707-2710.

[86] Kim, J.; Kim, F.; Huang, J. *Mater. Today* 2010, 13, 28-38.

[87] Yang, G.; Kim, J. *App. Phys. Lett*. 2015, 106, 081901.

[88] Meyerhofer, D. *J. Appl. Phys.* 1978, 49, 3993.

[89] Eickelmann, S. Real-Time Imaging Study of Ultra-Thin Liquid Films in a Spin-Cast Configuration. M.Sc. thesis, University of Potsdam, Potsdam, Germany, 2014.

[90] Danglad-Flores, J. A.; Eickelmann, S.; Riegler, H. *Chem. Eng. Sci*. 2018, 179, 257.

[91] Lazar, P.; Schollmeyer, H.; Riegler, H. *Phys. Rev. Lett*. 2005, 94, 116101.

[92] Gerstner, E. *Nature Phys*. 2011, 7449.

[93] Harrison, D.; Leuno, L. S. *Nature* 1961, 190, 433-434.

[94] Lee, W. T.; McKechnie, J. S.; Devereux, M. G. *Phys. Rev. E*. 2011, 83, 051609.

[95] Jo, H.; Kaviany, M.; Kim, S. H.; Kim, M. H. *Int. J. Heat Mass* 2014, 71, 149-157.

[96] Parmigiani, A.; Faroughi, S.; Huber, C.; Bachmann, O.; Su, Y. *Nature* 2016, 532, 492-495.

[97] Zhang, T. H.; Liu, X. Y. *Angew. Chem. Int. Ed.* 2009, 48, 1308-1312.

[98] Auer, S.; Frenkel, D. *Nature* 2001, 409, 1020-1023.

[99] Almeida, J. etc. *Nature* 2013, 502, 359-363.

[100] Gasser, U.; Weeks, E. R.; Schofield, A.; Pusey, P. N.; Weitz, D. A. *Science* 2001, 292, 258-262.

[101] Kwon, S. G.; Krylova, G.; Phillips, P. J. *Nature Mater*. 2015, 14, 215-223.

[102] Kwak, H. Y. *KSME international J*. 2004, 18, 1271-1287.

[103] Bigall, N. C.; Hartling, T.; Klose, M.; Simon, P.; Eng, L. M.; Eychmuller, A. Nano Lett. 2008, 8, 4588-4592.

[104] Frens, G. Nature Phys. Sci. 1973, 241, 20-22.

[105] Sumino, Y.; Magome, N.; Hamada, T.; Yoshikawa, K. *Phys. Rev. Lett*. 2005, 94, 068301.

[106] Lv, Y.; Chen, C.; Chuang, Y.-C.; Tseng, F.-G.; Yin, Y.; Crey, F.; Zheng, Q. *Phys. Rev. Lett*. 2014, 113, 026101.

[107] Jin, C.; Krüger, C.; Maass, C. C. *PNAS*. 2017, 114, 5089-5094.

[108] Amato, D. V.; Lee, H.; Werner, J. G.; Weitz, D. A.; Patton, D. L. *ACS Appl. Mater. Interfaces* 2017, 9, 3288-3293.

[109] Daniel, D.; Timonen, J. V. I.; Li, R.; Velling S. J.; Aizenberg. *Nature phys*. 2017, 13, 1020-1025.

[110] Bjelobrk, N.; Girard, H.-L.; Subramanyam, S. B.; Kwon, H.-M.; Quere, D.; Varanasi, K. K. *Phys. Rev. Fluids*. 2016, 1, 063902.

[111] Lazar, P.; Hans, R.. *Phys. Rev. Lett*. 2005, 95, 136103.

[112] Daniel, S.; Chaudhury, M. K.; Chen, J. C.. *Science*. 2001, 291, 633-636.

[113] Stone, H. A.; Stroock, A. D.; Ajdari, A. *Annu. Rev. Fluid*. 2004, 36, 381-411.

[114] Zheng, Y.; Bai, H.; Huang, Z.; Tian, X.; Nie, F.-Q.; Zhao, Y.; Zhai, J.; Jiang, L.. *Nature* 2010, 463, 640-643.

[115] Jalili, N.; Laxminarayana, K. *Mechatronics* 2004, 14, 907-945.

[116] Bohren, C.; Huffffman, D. Adsorption and scattering of light by small particles. John Wiley & Sons, New York, 1998.

[117] Chenyu, J. Theoretical and Experimental Study of Capillary Effect on Melting. PhD. thesis, University of Potsdam, Potsdam, Germany, 2014.

[118] Berg, H. C. Random walks in biology; Princeton University Press, New Jersey, 1993.

[119] Chen, G.; Perez-Garcia, R.; Danglad-Flores, J.; Riegler, H. *J. Phys. Chem. Lett*. 2017, 8, 6094-6098.

Appendix

A.1. List of abbreviations

Pt	Platinum
Au	Gold
SiO_2	Silicon dioxide
C_{60}	Fullerene
H_2O_2	Hydrogen peroxide
DI	Deionized
APTES	3-(aminopropyl) triethoxysilane
PMMA	Poly (methyl methacrylate)
PS	Polystyrene
PVC	Polyvinyl chloride
AFM	Atomic force microscopy
SEM	Scanning electron microscopy
TEM	Transmission electron microscopy
CVD	Chemical vapor deposition

A.2. Seeded growth synthesis of Pt NPs with different diameters

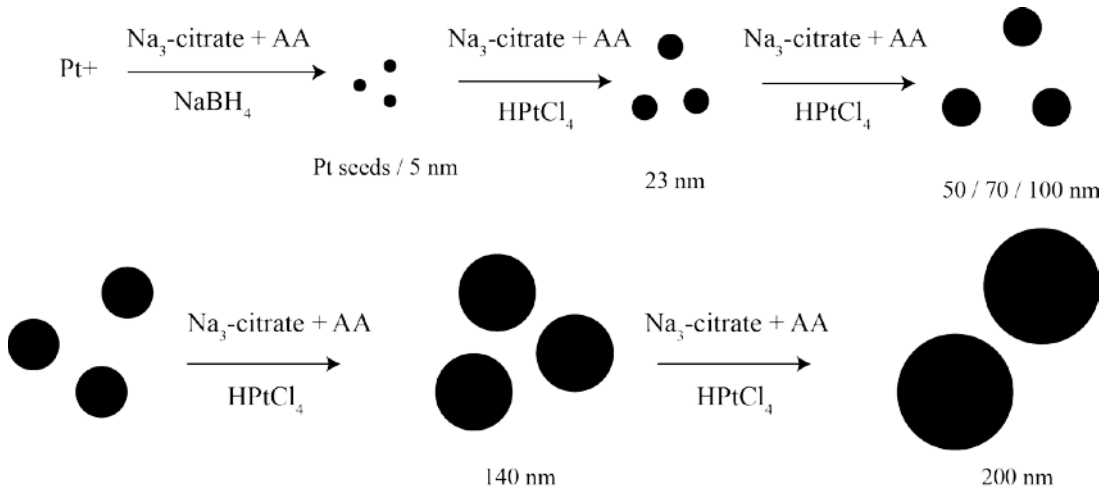

Figure S.1: Schematic diagram of the seeded growth method used for the synthesis of Pt nanoparticles with controlled diameters increasingly tuned from 5 nm to 200nm.

Figure S.1 shows a schematic diagram of the procedure used for the synthesis of Pt NPs with diameters controlled in the range of 5-200 nm. For the first step, Pt nanoparticle seed of about 5 nm was prepared by the standard sodium borohydride ($NaBH_4$) reduction method. Briefly, 7.2 mL of 0.02% aqueous solution of HPtCl4 was adding to 90 mL of boiling deionized (DI) water. Then 2.2 ml of solution containing 1% trisodium citrate and 0.05% citric acid was added, followed half a minute later by a quick injection of 1.1 mL of a freshly prepared NaBH4 (0.08%) solution containing 1% trisodium citrate and 0.05% citrate acid. After 10 minutes, the solution was cooled down to room temperature. The resultant suspension displayed a black color, which would be directly used as seeds to generate larger Pt NPs. The size and morphology of the resultant Pt seeds were determined by transmission electron microscopy (TEM). As shown in Figure A.2, the diameter of seeds is around 5 nm with a relatively uniform size.

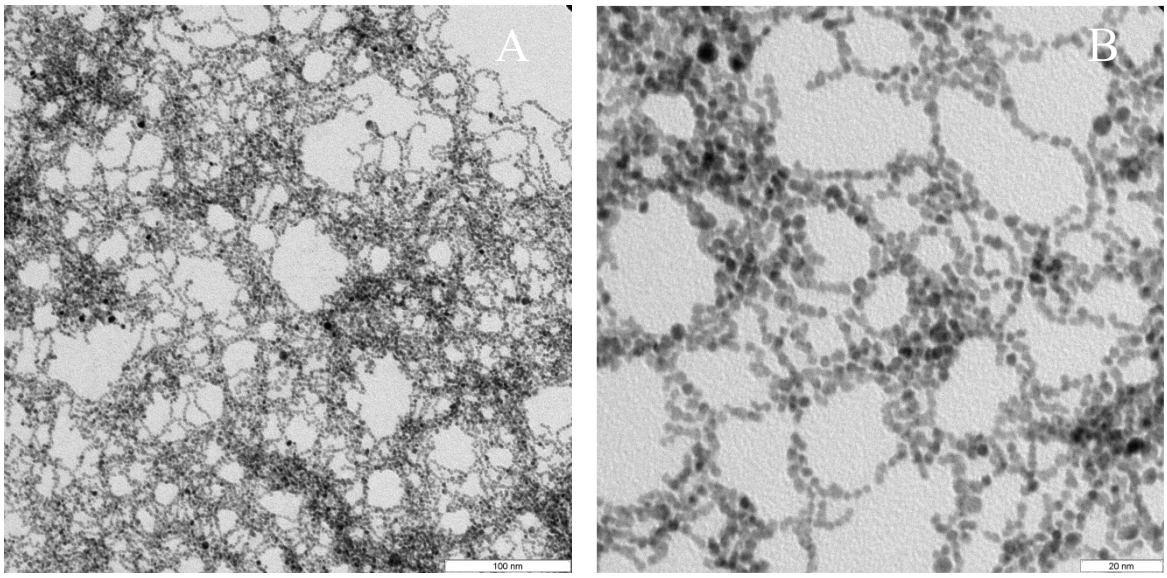

Figure S.2: TEM images of low (A) and high (B) resolution of Pt seeds with diameter of 5 nm.

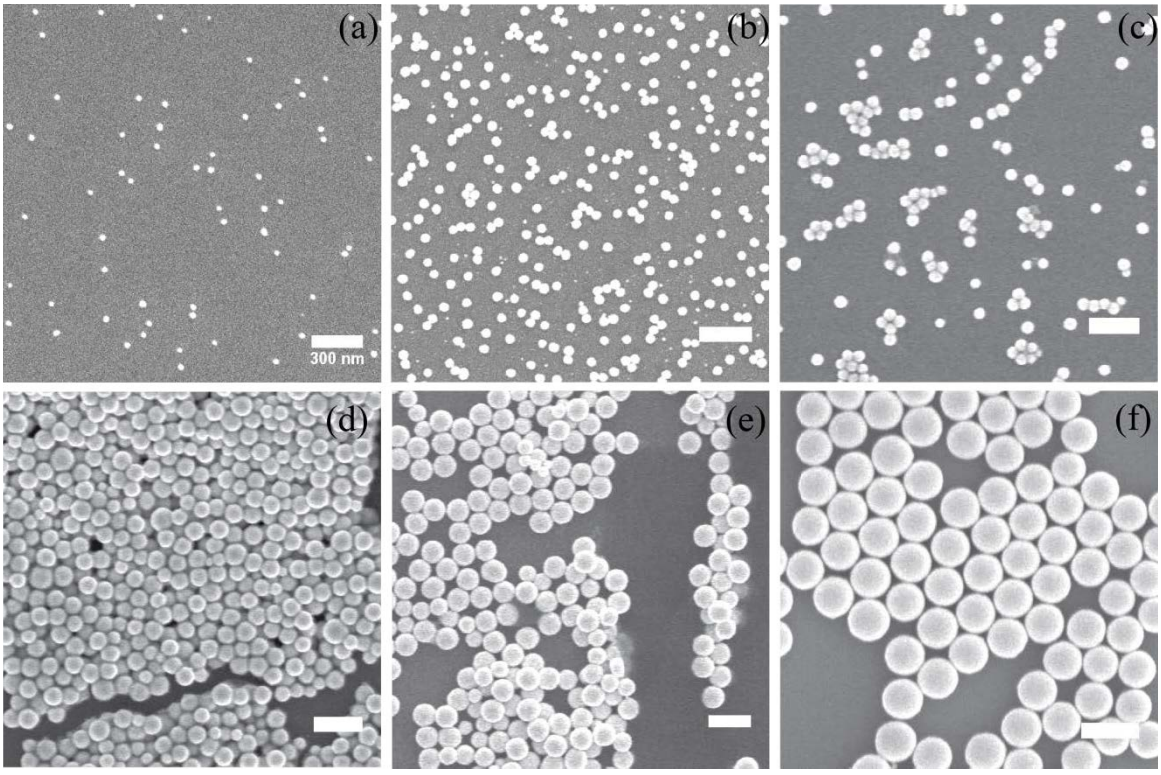

Figure S.3: SEM images of different diameters of Pt nanospheres: (a) 23 nm (seeds); (b) 50 nm; (c) 70 nm; (d) 100 nm; (e) 140 nm; (f) 200 nm. Scale bar: 300 nm.

Figure S.3 presents the SEM images of Pt NPs with different mean diameters of 23, 50, 70, 100, 140, and 200 nm, respectively. In the first round of seeded growth, we synthesized 23 nm Pt NPs in diameter using 5 nm Pt NPs as seeds. We added 1 mL of previous Pt seeds to 29 mL DI water in a three necked flask at room temperature. A 90 μL aliquot of the 0.2 mol/L precursor $HPtCl_4$ solution was added, followed by the addition of 0.5 mL solution containing 1% trisodium citrate and 1.25% ascorbic acid (AA). Under vigorously stirring, the temperature was slowly increased from room temperature to the boiling point in about 10 minutes. The reaction time was 30 minutes in total. Then the product was cooled to room temperature. In the second round of seeded growth, we used 23 nm Pt NPs as seeds. Similarly, 4 mL of above 23 nm Pt NPs solution was added to 26 mL DI water together with 0.09 mL of $HPtCl_4$ solution, followed by the addition of 0.5 mL of the solution containing 1% trisodium citrate and 1.25% AA. The final solution was slowly increased to boiling point and left to react for 30 minutes. We obtained NPs with diameter of 50 nm. The same procedure using 1 and 0.25 mL of seed solution in 29 mL of DI water resulted in 70 and 100 nm in diameter. In the third round of seeded growth, 130 nm Pt nanospheres were prepared by adding the 0.5 mL of 50 nm Pt NPs solution to 29 mL DI water together with 0.09 mL of $HPtCl_4$ solution, followed by the addition of 0.5 mL of the solution containing 1% trisodium citrate and 1.25% AA. The final solution was slowly increased to boiling point and left to react for 30 minutes. We obtained nanospheres with diameter of 140 nm. Finally, 200 nm Pt NPs were prepared by adding 0.5 mL of 140 nm Pt NPs solution to 29 mL DI water together with 0.09 mL of $HPtCl_4$ solution, followed by the addition of 0.5 mL of the solution containing 1% trisodium citrate and 1.25% AA. The final solution was slowly increased to boiling point and left to react for 30 minutes. With this seeded growth step, we produced NPs with diameter of 200 nm, as shown in Figure S.3.

A.3. Before and after sonification: superimposed images (AFM data)

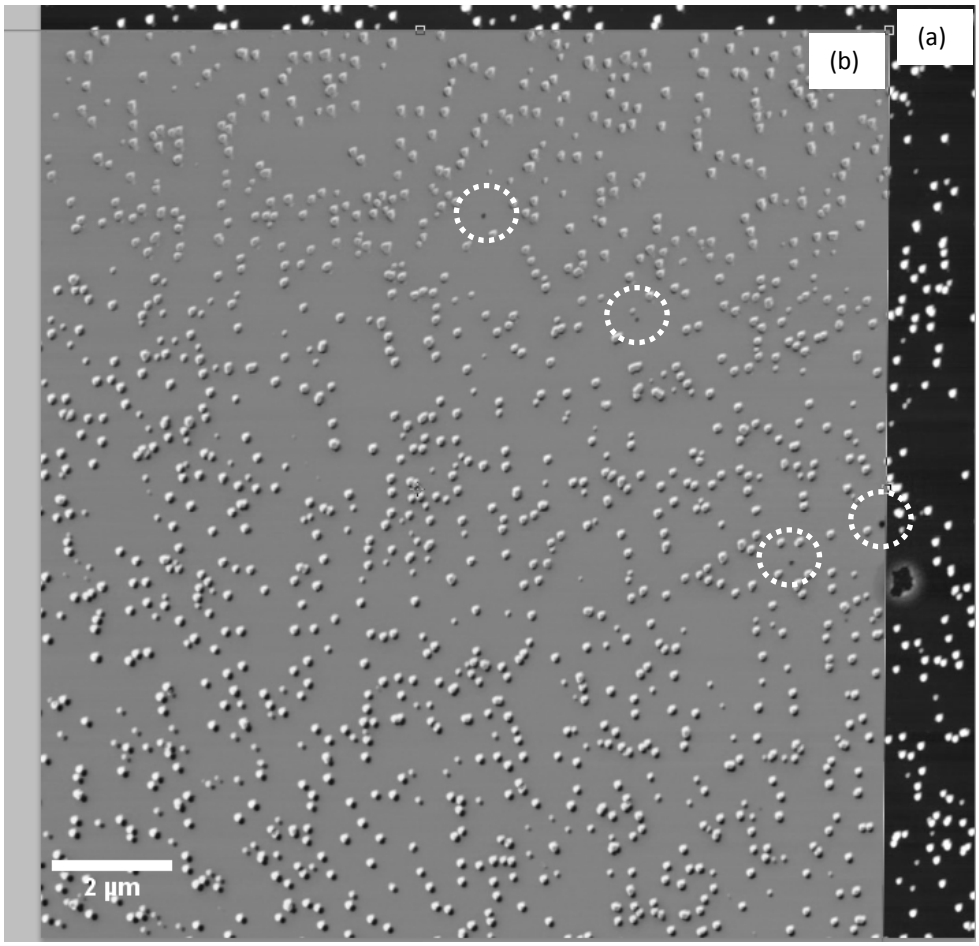

Figure S.3.: Superimposed identical regions of the substrate covered with NPs with the new immobilization protocol before (a) and after (b) 30 minutes of ultrasonication (AFM images). The round circles show the few NPs (black points) that were lost after the ultrasonication.

A.4. Footprint after moving the Au NPs after APTES

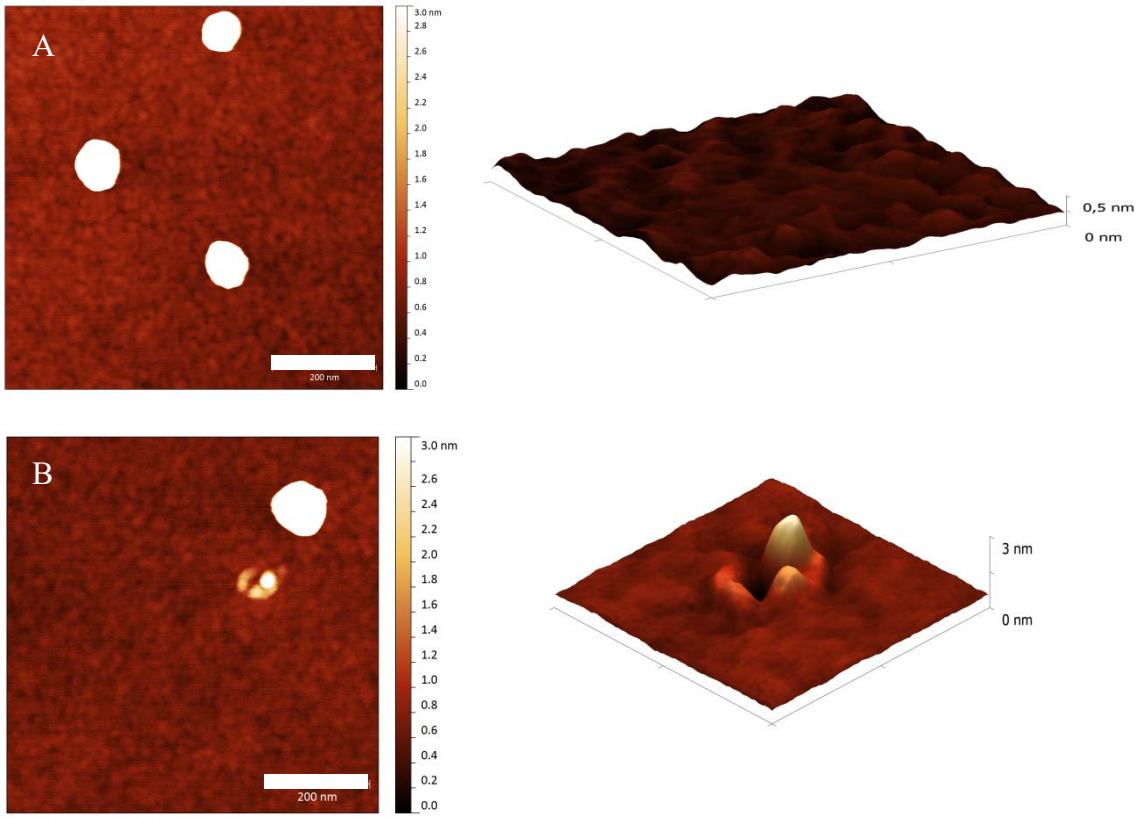

Figure S.5: AFM images of the footprint area after moving individual Au NP away from their original position and the corresponding AFM 3D images of the area in the vicinity of the NP. A: Au NPs without immobilization; B: Au NP-APTES immobilization.

A.5. Zeta potential characterization

Pt NPs colloids	**Origin Pt NPs colloids**	**Pt NPs were immersed in anhydrous ethanol for 3 hours**	**Pt NPs were immersed in APTES anhydrous ethanol mixture for 3 hours**
Zeta potential	-11.0 mM	-13.5 mM	-7.41 mM

We measured the zeta potential for the origin Pt NPs colloids and the Pt NPs which were incubated with APTES/ anhydrous ethanol mixture. The zeta potential for Pt NPs only incubated with anhydrous ethanol was also measured for a blank experiment. For the Pt NPs immersed in anhydrous ethanol or APTES/ anhydrous ethanol mixture, both were washed with anhydrous ethanol for 10 minutes and then re-dispersed in water. From the Table S1, we note that at the beginning, the potential value was -11.0 mM because of citrate covering on the surface of NPs. The zeta potential was a little decreasing for Pt NPs incubation in only anhydrous ethanol. For the Pt NPs immersed in APTES/ anhydrous ethanol mixture, the zeta potential was a little increasing that means the interaction between APTES and Pt NPs is weak, because we can use anhydrous ethanol rinse to get rid of such electrostatic adsorbing molecules.

A.6. AFM images of Pt NPs embedded in different thicknesses of PMMA film

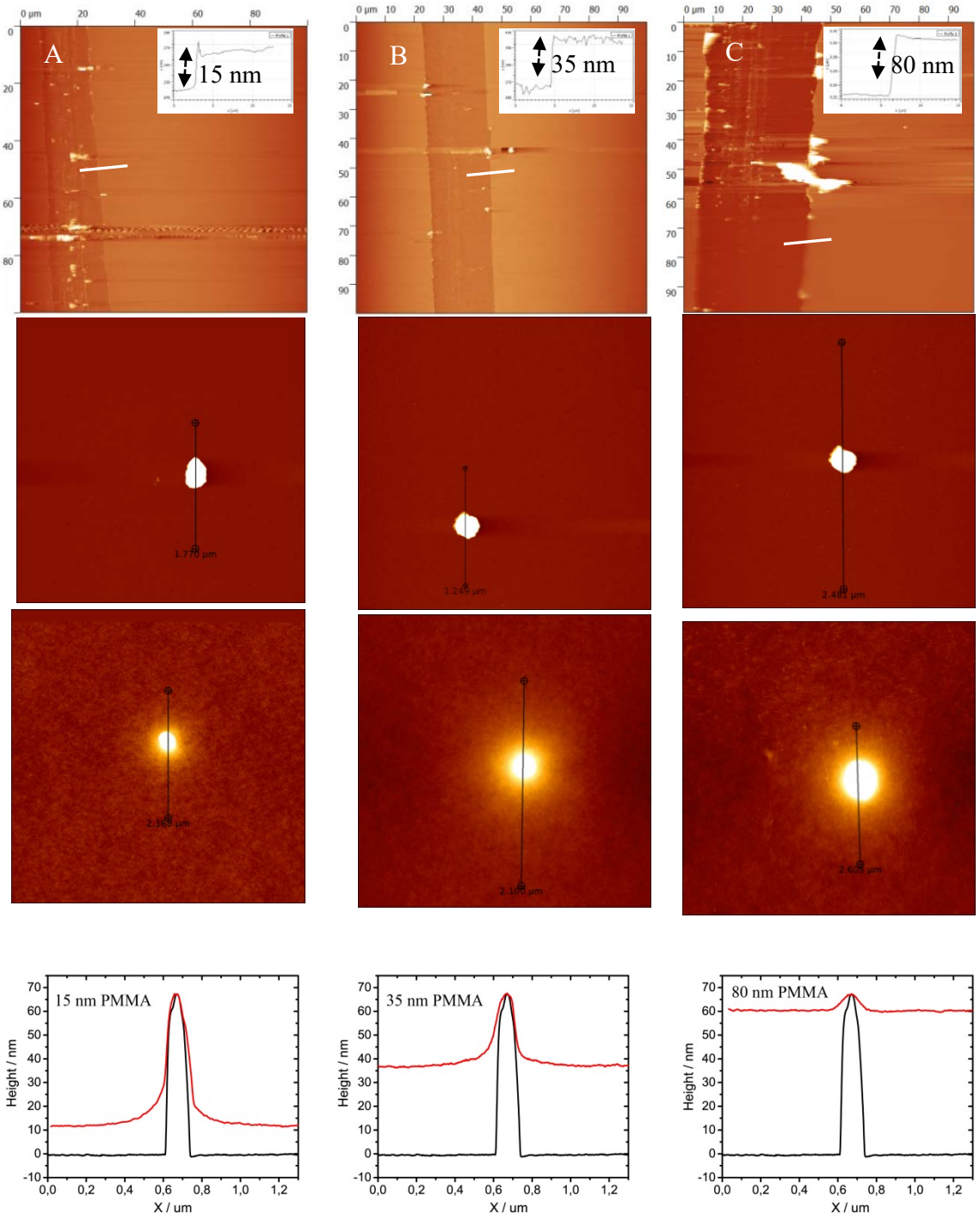

Figure S.6: AFM images of different thicknesses of PMMA film (A: 15 nm; B: 35 nm; C: 80 nm), before (the second row) and after (the third row) spin coating them onto 70 nm Pt NPs pre-coated substrate. And corresponding cross section images of the film height (the forth row).

Acknowledgement

The work presented in this thesis was done at the Max Planck Institute of Colloids and Interfaces. I would like to express my gratitude to all the people who have contributed to it. I would not have been possible to finish this thesis without the help and support of the kind people around me.

First of all, I would like to express my gratitude to my supervisor, Priv.- Doz. Dr. Hans Riegler, for giving me the opportunity and guiding my research projects in this unique and creative institute. I appreciate very much for his encouraging words and his vision in the word of science. His deep and broad knowledge in science and life gives me a lot of gains. I still have a lot to learn from you.

Then, I would like to thank Prof. Dr. Gerald Brezesinski, for the acceptance and help me during my PhD study.

I thank to my group members Rodrigo Perez-Garcia, José Danglad-Flores, Stephan Eickelmann, for your kind help and support, without you, I cannot finish this thesis successfully. Many thanks also to my former group members Dr. Chenyu Jin, Dr. Marie, Jehannin, Dr. Stefan, Karpitschka, Dr. Hubert, Gojzewski, for your kind help when I enter this group to start my PhD study.

I am thankful to Anneliese Heilig for her significant help and teaching when I start the AFM measurements.

Many thanks to my friends, Zhaoyong, Zupeng, Guoliang, Qianling, Yongjun, Jingsan, Ran, Jianke, Minrui… for your kind help in life and research and also giving me a lot of nice memories in Germany. I appreciate that so much.

I thank my committee members and reviewers for their valuable suggestions and time.

I gratefully acknowledge the funding support from China Scholarship Council (CSC). Without this scholarship, I would not be able to come to institute to pursue my PhD study.

I am very grateful for my wife Juan Xia for her love and patience during my PhD period. Last but not the least; I would like to express my deepest gratitude to my parents for their encouragement, patience and all their love. Only because of you, I can be brave to the challenging future.

Eigenständigkeitserklärung

Hiermit versichere ich, Guoxiang Chen, die vorliegende Arbeit *„Nanopartical at Solid Interfaces“* selbstständig und nur unter Verwendung der angegebenen Quellen und Hilfsmittel angefertigt zu haben. Übernommene Textstellen sind als solche gekennzeichnet.

Des Weiteren erkläre ich die Kenntnisnahme der dem angestrebten Verfahren zugrunde liegende Promotionsordnung. Ich habe die Arbeit an keiner anderen Hochschule vorgelegt und mich zu keinem früheren Zeitpunkt um ein Doktorgrad beworben.

Potsdam, 28.Mai 2018